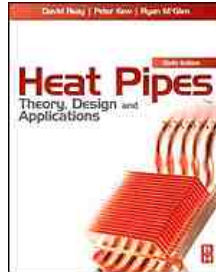# Chapters to Go

Heat Pipes: Theory, Design and Applications, Sixth Edition

by D.A. Reay, P.A. Kew and R.J. McGlen

Elsevier Science and Technology Books, Inc.. (c) 2014. Copying Prohibited.

Skillsoft

Chapter 2: Heat Transfer and Fluid Flow Theory

2.1 INTRODUCTION

As discussed in Chapter 6, there are many variants of heat pipe, but in all cases the working fluid must circulate when a temperature difference exists between the evaporator and condenser. In this chapter the operation of the classical wicked heat pipe is discussed. Various analytical techniques are then outlined in greater detail, and these techniques are then applied to the classical heat pipe and the gravity-assisted thermosyphon.

2.2 OPERATION OF HEAT PIPES

2.2.1 Wicked Heat Pipes

The overall thermal resistance of a heat pipe, defined by Eq. (2.1), should be low; however, it is first necessary to ensure that the device will function correctly.

The operating limits for a wicked heat pipe, first described in Ref. [1], are illustrated in Fig. 2.1.

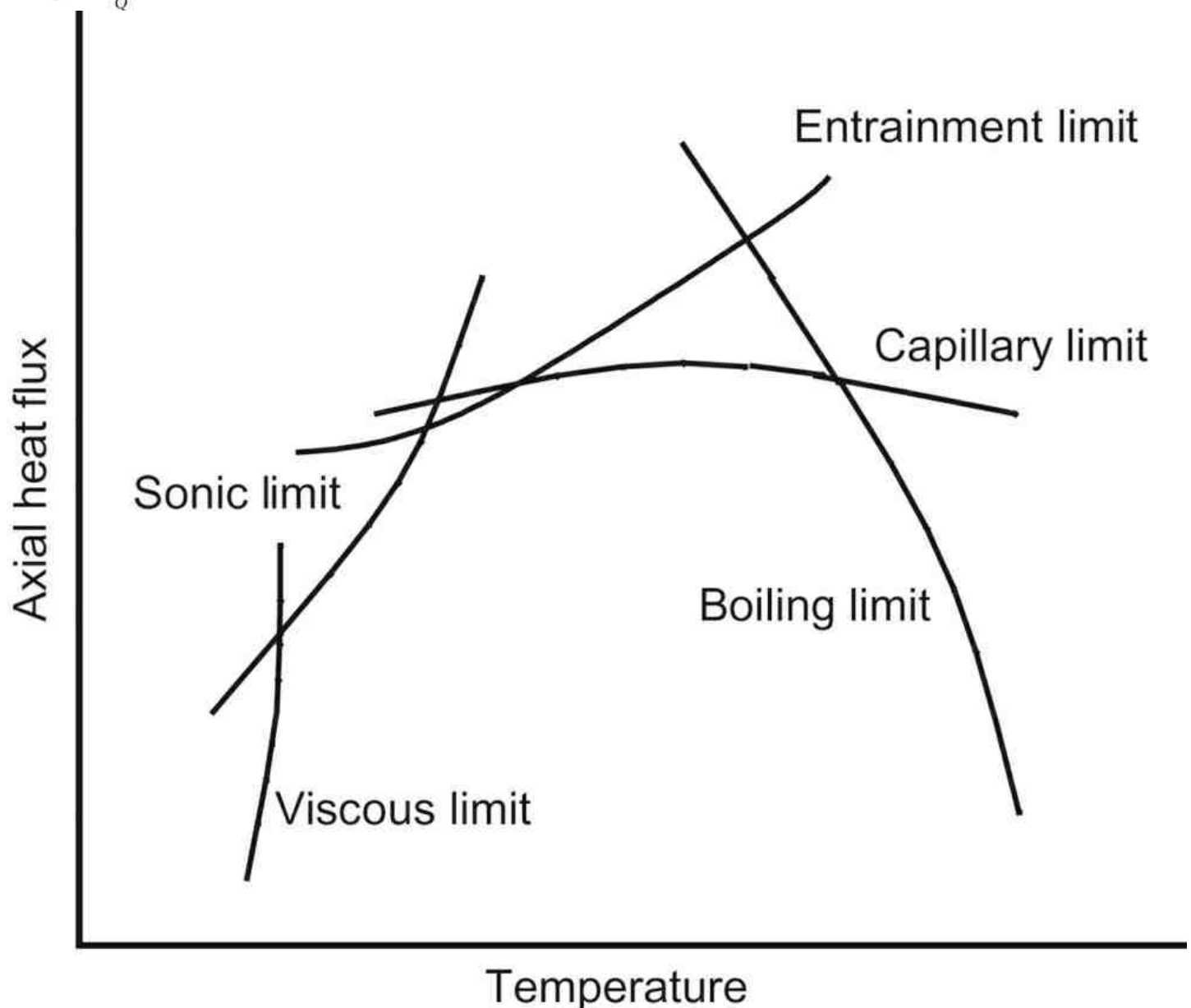(2.1) $$R = \frac{T_{hot} - T_{cold}}{\dot{Q}}$$

Figure 2.1: Limitations to heat transport in a heat pipe

Each of these limits may be considered in isolation.

In order for the heat pipe to operate the maximum capillary pumping pressure, $\Delta P_{c,max}$, must be greater than the total pressure drop in the pipe. This pressure drop is made up of three components.

    a. The pressure drop ΔP_l required to return the liquid from the condenser to the evaporator;

    b. The pressure drop ΔP_v necessary to cause the vapour to flow from the evaporator to the condenser;

    c. The pressure due to the gravitational head, ΔP_g which may be zero, positive or negative, depending on the inclination of the heat pipe.

For correct operation,[1]

(2.2) $\Delta P_{c,max} \geq \Delta P_l + \Delta P_v + \Delta P_g$

If this condition is not met, the wick will dry out in the evaporator region and the heat pipe will not operate. The maximum allowable heat flux for which Eq. (2.2) holds is referred to as the capillary limit. Methods of evaluating the four terms in Eq. (2.2) will be discussed in detail in this chapter. Typically, the capillary limit will determine the maximum heat flux over much of the operating range; however, the designer must check that a heat pipe is not required to function outside the envelope defined by the other operating limits, either at design conditions or at start-up.

During start-up and with certain high-temperature liquid metal heat pipes the vapour velocity may reach sonic values. The sonic velocity sets a limit on the heat pipe performance. At velocities approaching sonic compressibility effects must be taken into account in the calculation of the vapour pressure drop.

The viscous or vapour pressure limit is also generally most important at start-up. At low temperature the vapour pressure of the fluid in the evaporator is very low, and, since the condenser pressure cannot be less than zero, the difference in vapour pressure is insufficient to overcome viscous and gravitational forces, thus preventing satisfactory operation.

At high heat fluxes the vapour velocity necessarily increases, if this velocity is sufficient to entrain liquid returning to the evaporator then performance will decline. Hence the existence of an entrainment limit.

The above limits relate to axial flow through the heat pipe. The final operating limit discussed will be the boiling limit. The radial heat flux in the evaporator is accompanied by a temperature difference which is relatively small until a critical value of heat flux is reached above which vapour blankets the evaporator surface resulting in an excessive temperature difference.

The position of the curves and shape of the operating envelope shown in Fig. 2.1 depends upon the wick material, working fluid and geometry of the heat pipe.

2.2.2 Thermosyphons

The two-phase thermosyphon is thermodynamically similar to the wicked heat pipe but relies on gravity to ensure liquid return from the condenser to the evaporator. A wick or wicks may be incorporated in at least part of the unit to reduce entrainment and improve liquid distribution within the evaporator.

2.2.3 Loop Heat Pipes and Capillary Pumped Loops

As will be seen later, the characteristics which produce a wick having the capability to produce a large capillary pressure also lead to high values of pressure drop through a lengthy wick. This problem can be overcome by incorporating a short wick contained within the evaporator section and separating the vapour flow to the condenser from the liquid return.

[1]Note that this implies that the capillary pressure rise is considered as positive, while pressure drops due to liquid and vapour flow or gravity are considered positive.

2.3 THEORETICAL BACKGROUND

In this section the theory underpinning the evaluation of the terms in Eqs (2.1) and (2.2) and the determination of the operating limits shown in Fig. 2.1 is discussed.

2.3.1 Gravitational Head

The pressure difference, ΔP_g, due to the hydrostatic head of liquid may be positive, negative or zero, depending on the relative positions of the condenser and evaporator. The pressure difference may be determined from:

(2.3) $\Delta P_g = \rho_l g l \sin\phi$

where ρ_l is the liquid density (kg/m^3), g the acceleration due to gravity (9.81 m/s^2), l length of the heat pipe (m) and ϕ the angle between the heat pipe and the horizontal defined such that ϕ is positive when the condenser is lower than the evaporator.

2.3.2 Surface Tension and Capillarity

2.3.2.1 Introduction

Molecules in a liquid attract one another. A molecule in a liquid will be attracted by the molecules surrounding it and, on average, a molecule in the bulk of the fluid will not experience any resultant force. In the case of a molecule at or near the surface of a liquid the forces of attraction will no longer balance out and the molecule will experience a resultant force inwards. Because of this effect the liquid will tend to take up a shape having minimum surface area; in the case of a free falling drop in a vacuum this would be a sphere. Due to this spontaneous tendency to contract a liquid surface behaves rather like a rubber membrane under tension. In order to increase the surface area work must be done on the liquid. The energy associated with this work is known as the free surface energy, and the corresponding free surface energy/unit surface area is given the symbol σ_l. For example, if a soap film is set up on a wire support as in Fig. 2.2(a) and the area is increased by moving one side a distance dx, the work done is equal to F dx, hence the increase in surface energy is $2\sigma_l l dx$.
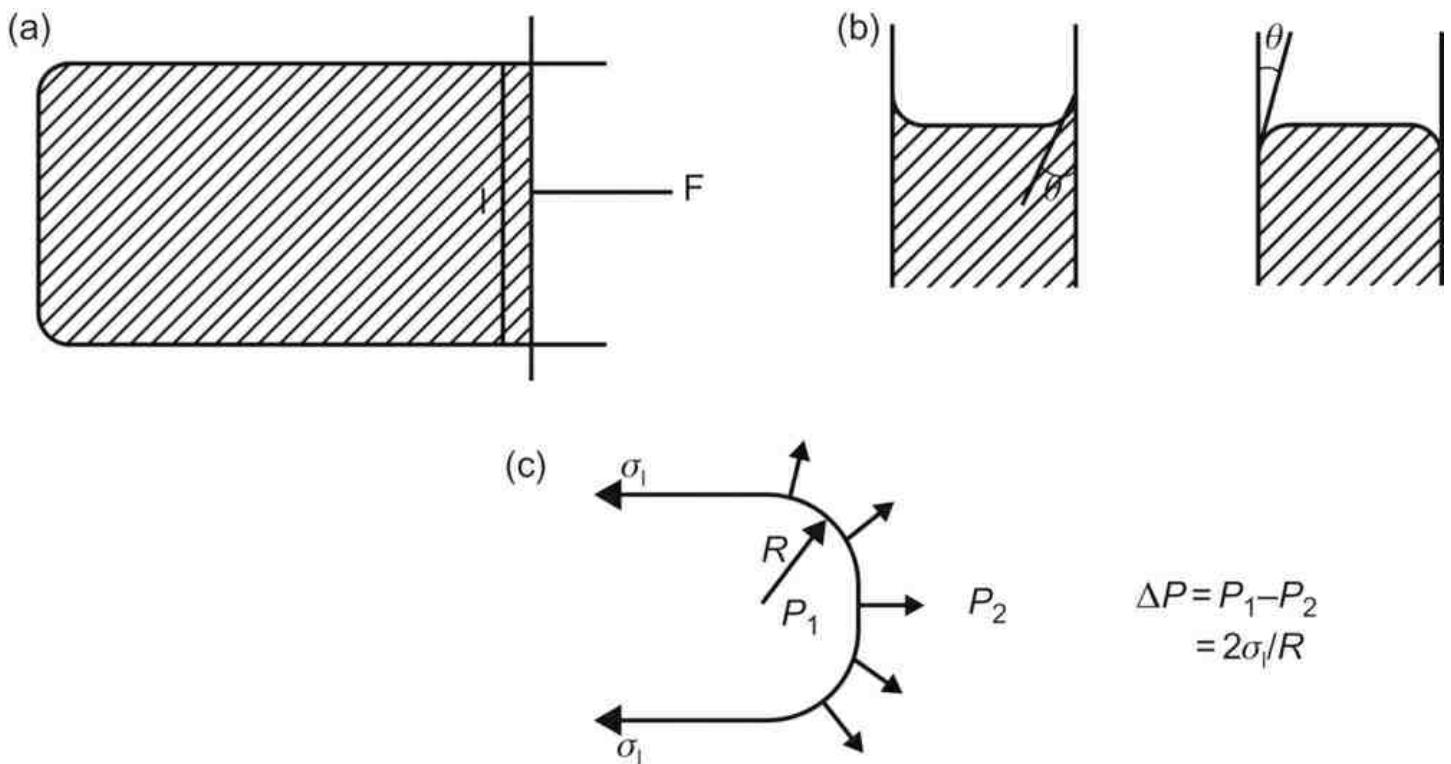

Figure 2.2: Representation of surface tension and pressure difference across a curved surface

The factor 2 arises since the film has two free surfaces. Hence if T is the force/unit length for each of the two surfaces, $2Tldx = 2\sigma_l l dx$ or $T = \sigma_l$. This force/unit length is known as the surface tension. It is numerically equal to the surface energy/unit area measured in any consistent set of units, e.g. N/m.

Values for surface tension for a number of common working fluids are given in Appendix 1.

Since latent heat of vaporisation, L, is a measure of the forces of attraction between the molecules of a liquid we might expect surface energy or surface tension σ_l to be related to L. This is found to be the case. Solids also will have a free surface energy and in magnitude it is found to be similar to the value for the same material in the molten state.

When a liquid is in contact with a solid surface, molecules in the liquid adjacent to the solid will experience forces from the molecules of the solid in addition to the forces from other molecules in the liquid. Depending on whether these solid/liquid

    Elsevier Science and Technology Books, Inc., David Reay, Peter Kew, Ryan McGlen (c) 2014, Copying Prohibited

forces are attractive or repulsive, the liquid solid surface will curve upwards or downwards, as indicated in Fig. 2.2(b). The two best-known examples of attractive and repulsive forces respectively are water and mercury. Where the forces are attractive the liquid is said to 'wet' the solid. The angle of contact made by the liquid surface with the solid is known as the contact angle, θ. For wetting θ will lie between 0 and $\pi/2$ radians and for non-wetting liquids $\theta > \pi/2$.

The condition for wetting to occur is that the total surface energy is reduced by wetting.

$\sigma_{sl} + \sigma_{lv} < \sigma_{sv}$

where the subscripts, s, l and v refer to solid, liquid and vapour phases, respectively, as shown in Fig. 2.3(a).
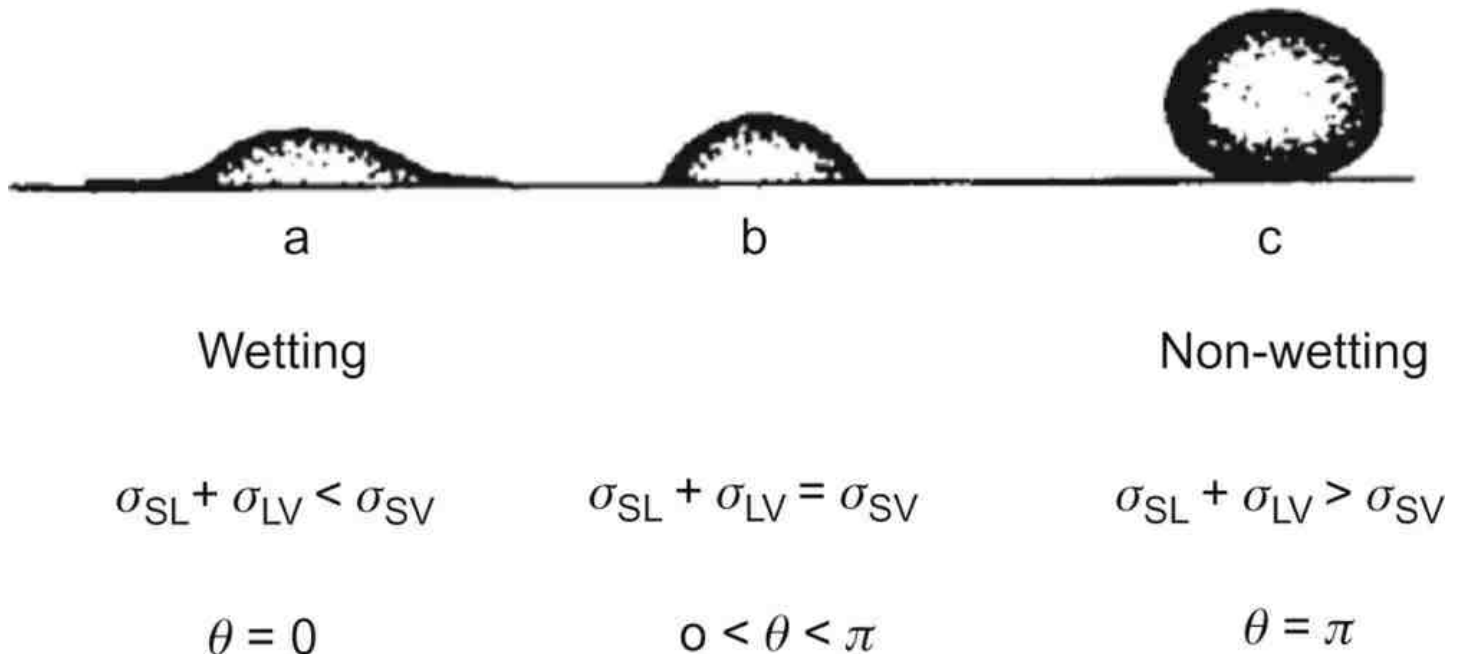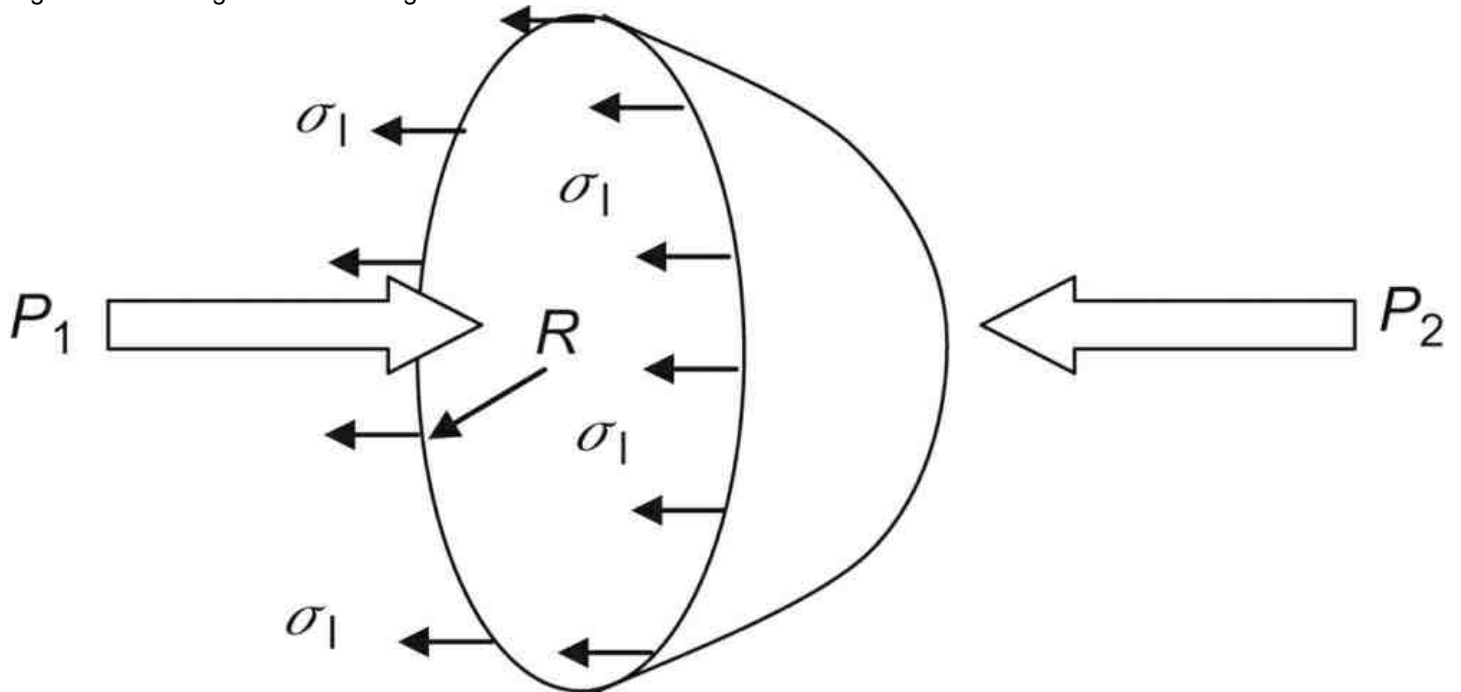

Figure 2.3: Wetting and non-wetting contact

Figure 2.4: Pressure difference across a curved liquid surface

Wetting will not occur if $\sigma_{sl} + \sigma_{lv} > \sigma_{sv}$ as in Fig. 2.3(c) while the intermediate condition of partial wetting $\sigma_{sl} + \sigma_{lv} = \sigma_{sv}$ is illustrated in Fig. 2.3(b).

2.3.2.2 Pressure Difference across a Curved Surface

A consequence of surface tension is that the pressure on the concave surface is greater than that on the convex surface. With reference to Figs 2.2(c) and 2.4, this pressure difference ΔP is related to the surface energy σ_l and radius of curvature R of the surface.

The hemispherical surface tension force acting around the circumference is given by $2\pi R\sigma_l$ and must be balanced by the net force on the surface due to the pressures which is $(P_1 - P_2)\pi R^2$ or $\Delta P\pi R^2$. Thus,

(2.4) $\Delta P = \dfrac{2\sigma_1}{R}$

If the surface is not spherical, but can be described by two radii of curvature, R_1 and R_2 at right angles, then it can be shown that Eq. (2.4) becomes:

(2.5) $\Delta P = 2\sigma_1\left(\dfrac{1}{R_1} + \dfrac{1}{R_2}\right)$

Due to this pressure difference, if a vertical tube, radius r, is placed in a liquid which wets the material of the tube, the liquid will rise in the tube to a height above the plane surface of the liquid as shown in Fig. 2.5.

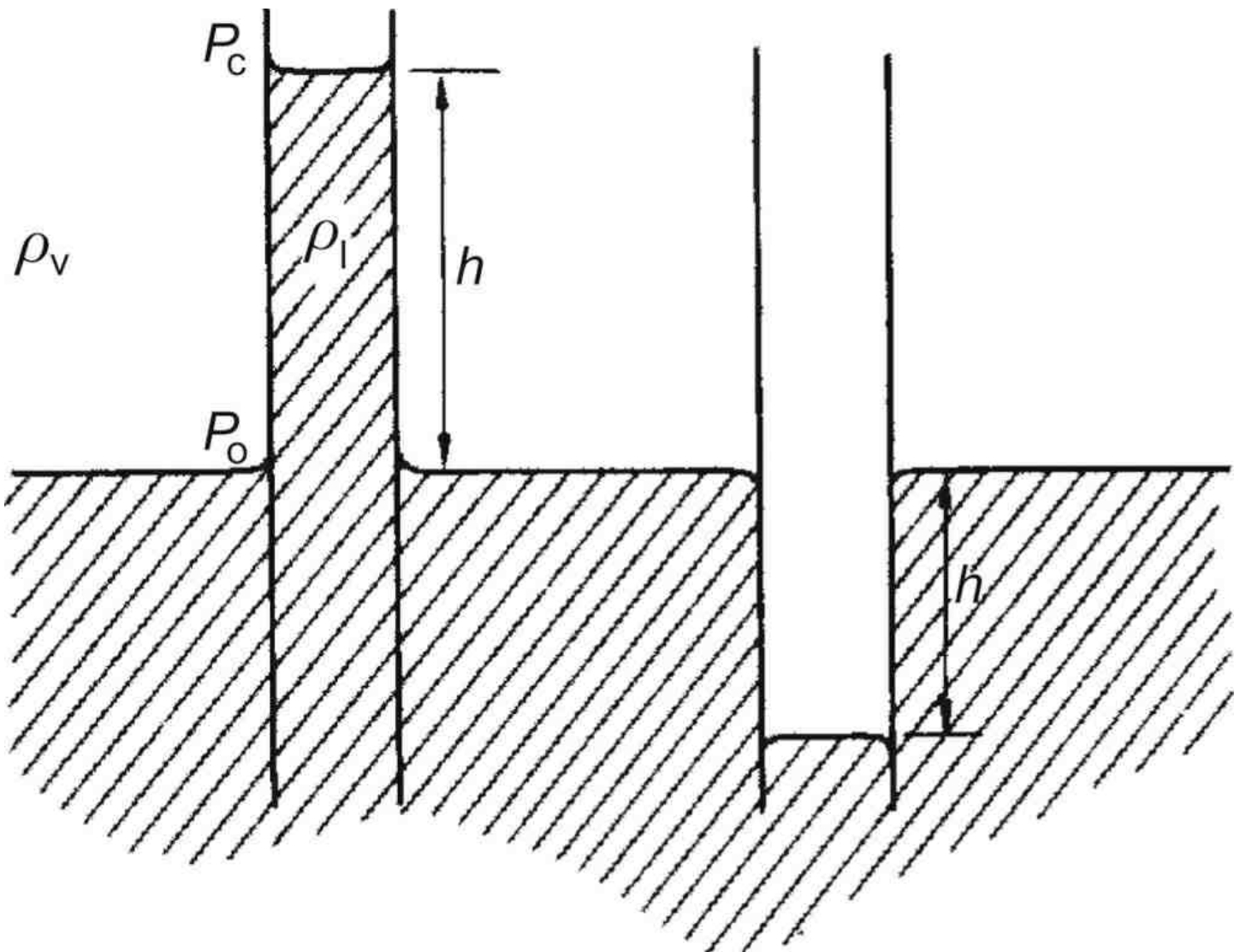Figure 2.5: Capillary rise in a tube (wetting and non-wetting fluids)

The pressure balance gives, for a tube radius r:

(2.6) $(\rho_1 - \rho_v)gh = \dfrac{2\sigma_1}{r}\cos\theta \approx \rho_1 gh$

For the case of a non-circular tube,

(2.7) $\dfrac{1}{r} = \left(\dfrac{1}{R_1} + \dfrac{1}{R_2} \right)$

where ρ_l is the liquid density, ρ_v is the vapour density and θ is the contact angle. This effect is known as capillary action or capillarity and is the basic driving force for the wicked heat pipe.

For non-wetting liquids cos θ is negative and the curved surface is depressed below the plane of the liquid level. In heat pipes wetting liquids are always used, the capillary lift increasing with liquid surface tension and decreasing contact angle.

2.3.2.3 Change in Vapour Pressure at a Curved Liquid Surface

From Fig. 2.5 it can be seen that the vapour pressure at the concave surface is less than that at the plane liquid surface by an amount equal to the weight of a vapour column of unit area, length h.

$P_c - P_o = g \rho_v h$

Assuming that ρ_v is constant.

Combining this with Eq. (2.6):

(2.8) $P_c - P_o = \dfrac{2\sigma_1}{r} \dfrac{\rho_v}{(\rho_1 - \rho_v)} \cos \theta$

This pressure difference $P_c - P_o$ is small compared to the capillary head $(2\sigma_1/r)\cos\theta$ and may normally be neglected when considering the pressures within a heat pipe. It is, however, worth noting that the difference in vapour pressure between the vapour in a bubble and the surrounding liquid is an important phenomena in boiling heat transfer.

2.3.2.4 Measurement of Surface Tension

There is a large number of methods for the measurement of surface tension of a liquid, and these are described in the standard texts [2,3]. For our present purpose we are interested in the capillary force, $\sigma_1 \cos\theta$, which is dependent on both liquid and surface properties. The simplest measurement is that of capillary rise h in a tube, which gives:

(2.9) $\sigma_1 \cos\theta \approx \dfrac{\rho_1 g h r}{2}$

In practical heat pipe design it is also necessary to know r, the effective pore radius. This is by no means easy to estimate for a wick made up of a sintered porous structure or from several layers of gauze. By measuring the maximum height the working fluid will attain it is possible to obtain information on the capillary head for fluid wick combinations. Several workers have reported measurements on maximum height for different structures and some results are given in Chapter 3. The results may differ for the same structure depending on whether the film was rising or falling; the reason for this is brought out in Fig. 2.6.
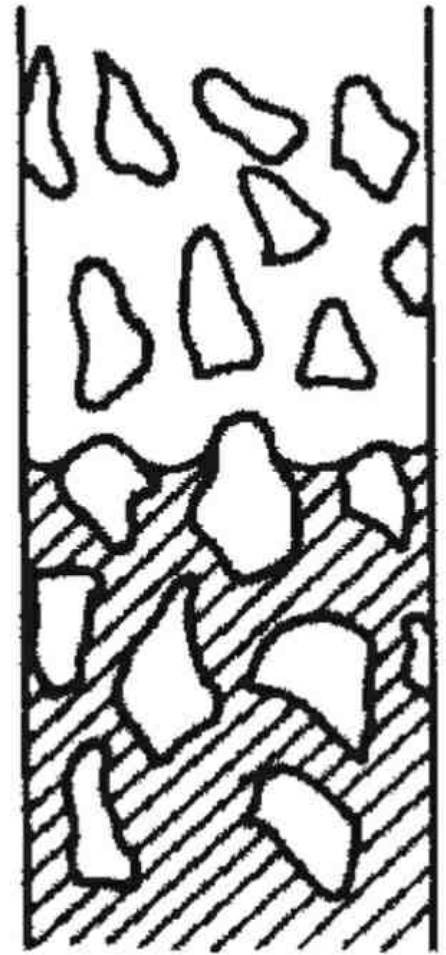
Figure 2.6: Rising and falling column interface

Another simple method, for the measurement of σ_l, due to Jäger, and shown schematically in Fig. 2.7 is sometimes employed. This involves the measurement of maximum bubble pressure. The pressure is progressively increased until the bubble breaks away and the pressure falls. When the bubble radius reaches that of the tube pressure is a maximum P_{max} and at this point,

(2.10) $\quad P_{max} = \rho_l h g + \dfrac{2\sigma_l}{r}$

$$\sigma_1 = r/2 \ (P_{max} - P_l \ gh)$$
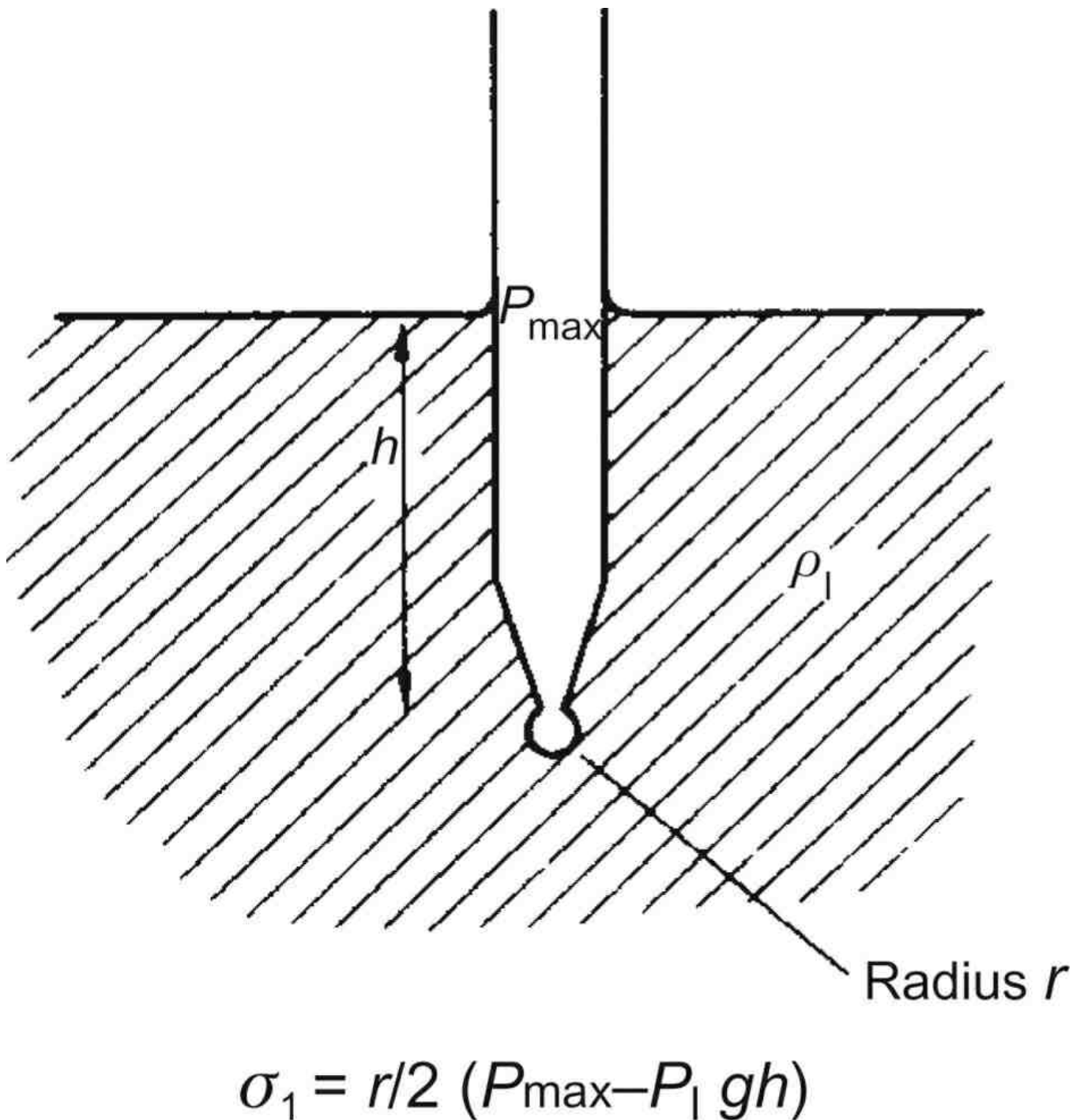
Figure 2.7: Jäger's method for surface tension measurement

This method has proved appropriate [4] for measurement of the surface tension of liquid metals.

The surface tension of two liquids can be compared by comparing the mass of the droplets falling from a narrow vertical tube. If the mass of the droplets for liquids 1 and 2 are m_1 and m_2, respectively, then:

(2.11) $\dfrac{m_1 \rho_{l1}}{m_2 \rho_{l2}} = \dfrac{\sigma_{f1}}{\sigma_{f2}}$

2.3.2.5 Temperature Dependence of Surface Tension

Surface tension decreases with increasing temperature, it is therefore important to take temperature effects into account if using the results of measurements at typical ambient temperatures.

Values of surface tension for over 2000 pure fluids have been tabulated by Jasper [5] and temperature corrections of the form $\sigma = a + bT$ are suggested.

For water the following interpolating equation [6] gives good values of surface tension:

$$(2.12) \quad \sigma_1 = B(1 - T_r)^\mu (1 - b(1 - T_r))$$

where T_r is the reduced temperature $= T/T_c$, T_c=647.096 K, B=235.8 mN/m, b=0.625 and μ=1.256.

Equation (2.12) is valid between the triple point (0.01°C) and the critical temperature, and is in agreement with measured data to within experimental uncertainty.

Eötvös proposed a relationship which was later modified by Ramsay and Shields to give:

$$(2.13) \quad \sigma_1 \left(\frac{M}{\rho_1} \right)^{2/3} = H(T_c - 6 - T)$$

where M is the molecular weight, T_c is the critical temperature (K), T the fluid temperature (K) and H is a constant, the value of which depends upon the nature of the liquid.

The Eötvös–Ramsay–Shields equation does not give agreement with the experimentally observed behaviour of liquid metals and molten salts. Bohdanski and Schins [7] have derived an equation which applies to the alkali metals. While Fink and Leibowitz [8] recommended:

$$(2.14) \quad \sigma_1 = \sigma_o \left(1 - \frac{T}{T_c} \right)^n (mN/m)$$

for sodium, where σ_o=240.5 mN/m, n=1.126 and T_c=2503.7 K.

Alternatively, the surface tension of liquid metals may be estimated from the data provided by Iida and Guthrie [9] and summarised in Table 2.1. The value of surface tension may then be calculated:

$$\sigma_1 = \sigma_{lm} + (T - T_m) d\sigma/dT$$

Table 2.1: Surface Tension of Selected Liquid Metals [9]

		M (kg/kmol)	Melting Point, T_m (K)	Boiling Point, 1 bar (K)	σ_{lm} at Melting Point (mN/m)	$d\sigma/dT$ (mN/mK)
Lithium	Li	7	452.2	1590	398	−0.14
Sodium	Na	23	371.1	1151	191	−0.1
Potassium	K	39	336.8	1035	115	−0.08
Caesium	Cs	133	301.65	1033	70	−0.06
Mercury	Hg	200	234.3	630	498	−0.2

A method of evaluating surface tension based upon the number and nature of chemical bonds was first suggested by Walden [10] and developed by Sugden [11] and Quale [12].

$$(2.15) \quad \sigma^{0.25} = \frac{P}{M}(\rho_1 - \rho_v)$$

where P was defined by Walden as a parachor. Values of the increments to be used in evaluating the parachor, adapted to give values of surface tension in N/m are given in Ref. [13].

2.3.2.6 Capillary Pressure ΔP_c

Equation (2.4) shows that the pressure drop across a curved liquid interface is:

$$\Delta P = \frac{2\sigma_1}{R}$$

From Fig. 2.8 we can see that $R \cos \theta = r$ where r is the effective radius of the wick pores and θ the contact angle. Hence the capillary head at the evaporator, $\Delta P'_e$ is:

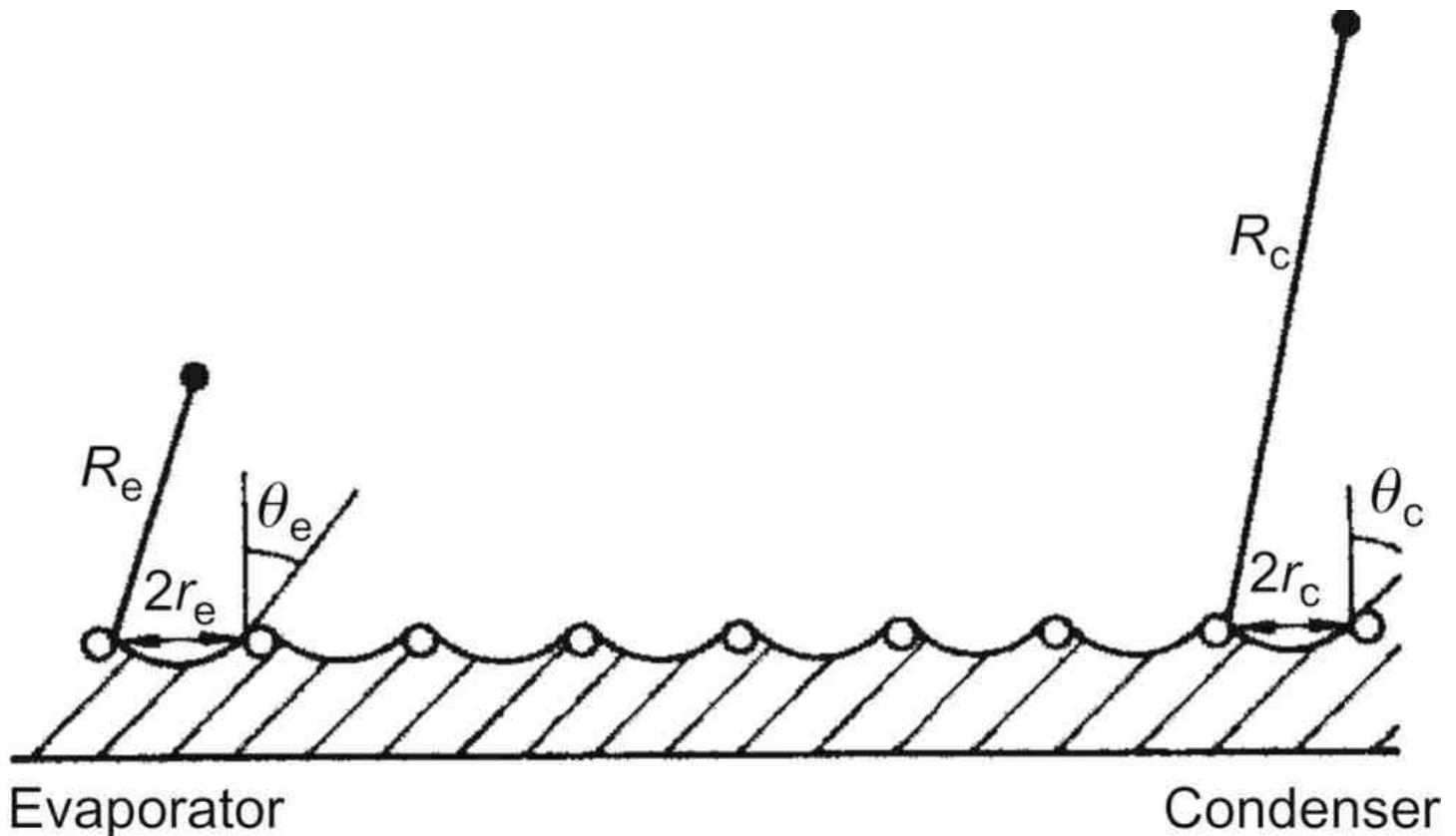$$(2.16a) \quad \Delta P'_e = 2\sigma_1 \frac{\cos \theta_e}{r_e}$$

Figure 2.8: Wick and pore parameters in evaporator and condenser

Similarly, for the condenser:

(2.16b) $\Delta P'_c = 2\sigma_1 \dfrac{\cos \theta_c}{r_c}$

and the capillary driving pressure, ΔP_c, is given by $\Delta P'_e - \Delta P'_c$.

It is worth noting that ΔP_c is a function only of the conditions where a meniscus exists. It does not depend on the length of the adiabatic section of the wick. This is particularly important in the design of loop heat pipes.

2.3.3 Pressure Difference Due to Friction Forces

In this section we will consider the pressure differences caused by frictional forces in liquids and vapours flowing in a heat pipe. Firstly, it is convenient to define some of the terms which will be used later in this chapter.

2.3.3.1 Laminar and Turbulent Flow

If one imagines a deck of playing cards or a sheaf of papers, initially stacked to produce a rectangle, to be sheared as shown in Fig. 2.9, it can be seen that the individual cards, or lamina, slide over each other. There is no movement of material perpendicular to the shear direction.
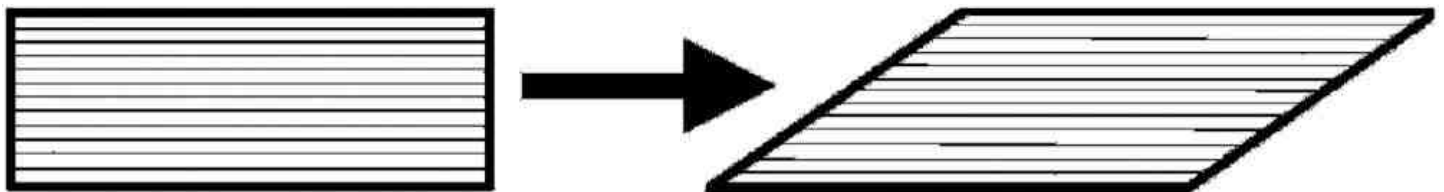

Figure 2.9: Shear applied to parallel sheets

Similarly, in laminar fluid flow there is no mixing of the fluid and the fluid can be regarded as a series of layers sliding past each other.

Consideration of a simple laminar flow allows us to define viscosity. Figure 2.10 illustrates the velocity profile for a laminar flow

of a fluid over a flat plate.
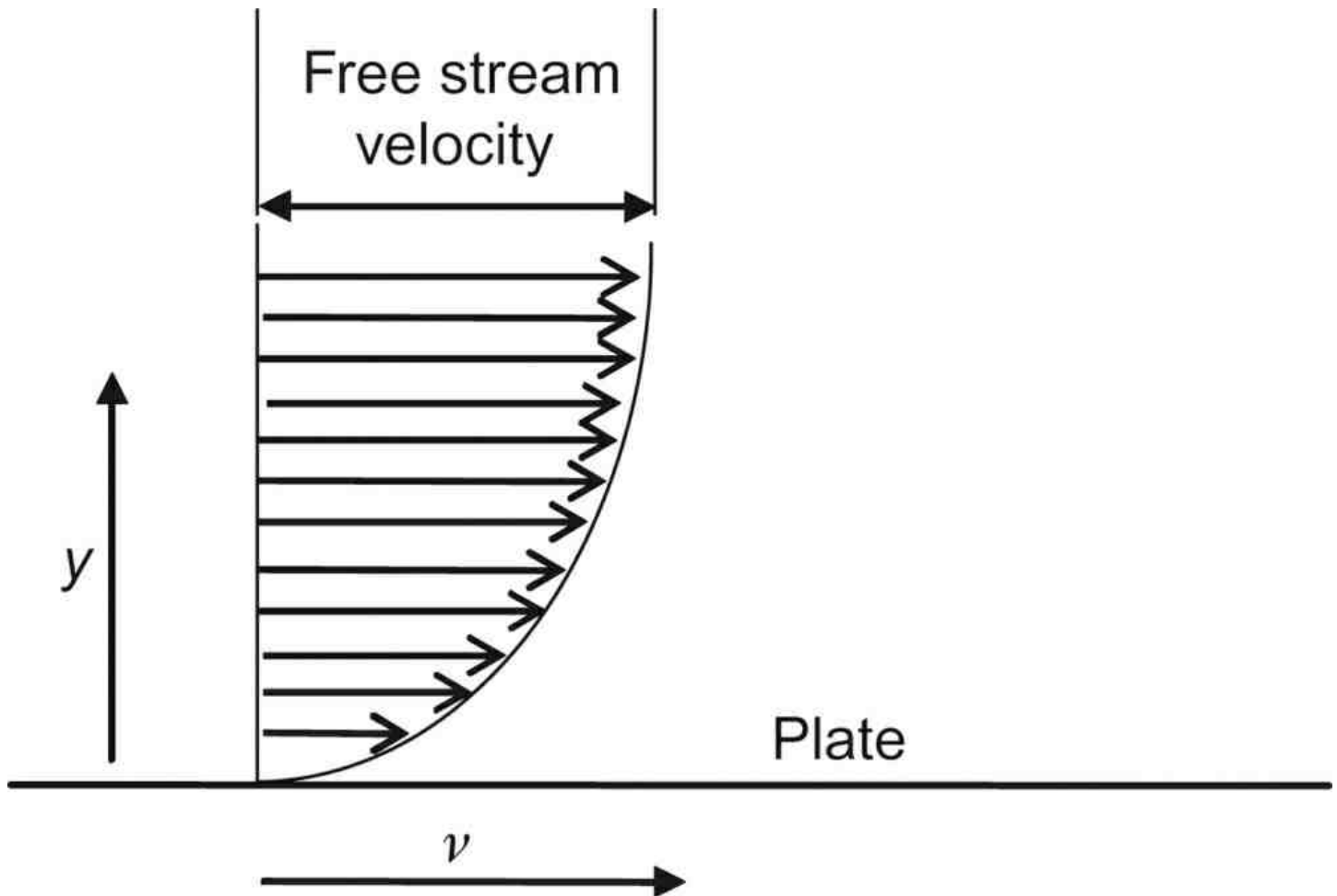
Figure 2.10: Velocity profile in laminar flow over a flat plate

The absolute or dynamic viscosity of a fluid, μ, is defined by:

$$\tau = \mu \frac{dv}{dy}$$

where τ is the shear stress. At the wall, the velocity of the fluid must be zero, and the wall shear stress is given by:

$$\tau_w = \mu \left(\frac{dv}{dy} \right)_w$$

In practice, laminar flow is observed at low speeds, in small tubes or channels, with highly viscous fluids and very close to solid walls. It is the flow normally observed when liquid flows through the wick of a heat pipe.

If the fluid layers seen in laminar flow break up and fluid mixes between the layers, then the flow is said to be turbulent. The turbulent mixing of fluid perpendicular to the flow direction leads to a more effective transfer of momentum and internal energy between the wall and the bulk of the fluid. This is illustrated in Fig. 2.11.

Figure 2.11: Development of the boundary layer over a flat plate

The heat transfer and pressure drop characteristics of laminar and turbulent flows are very different. In forced convection the magnitude of the Reynolds number, defined below, provides an indication of whether the flow is likely to be laminar or turbulent.
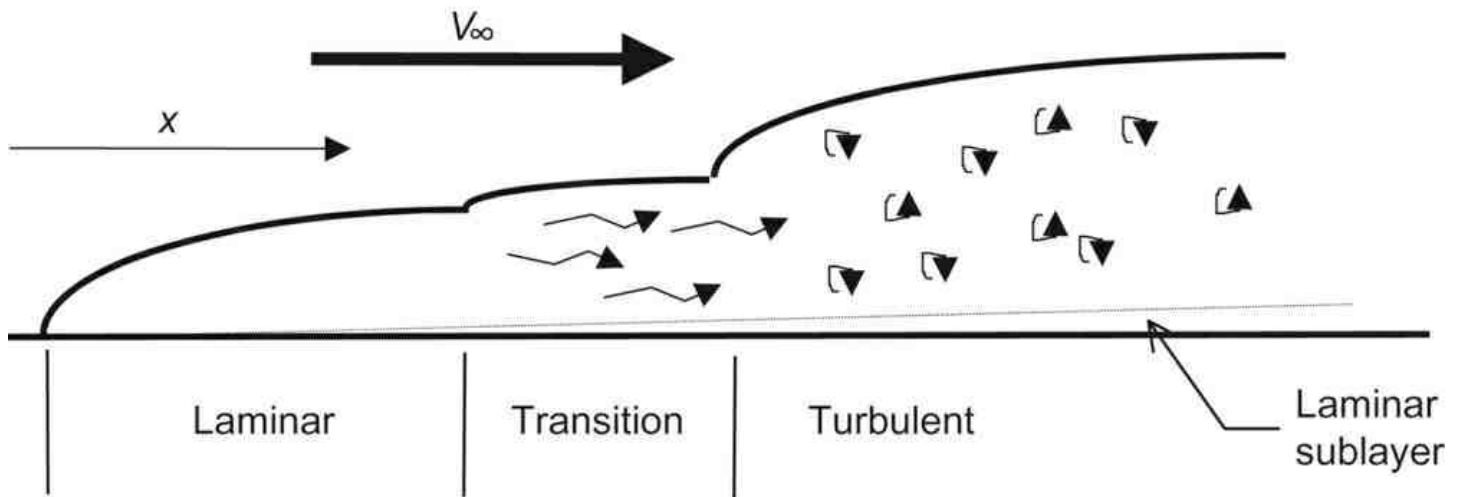
$$Re = \frac{\rho v d_{rep}}{\mu}$$

where d_{rep} is a representative linear dimension. If the Reynolds number is written as:

$$Re = \frac{\rho v^2}{\mu v/d}$$

then it can be seen to be a measure of the relative importance of inertial and viscous forces acting on the fluid.

For flow over a flat plate, as shown in Fig. 2.11, we may determine whether the flow in the boundary layer is likely to be laminar or turbulent by applying the following conditions:

$$Re_x \left(= \frac{\rho V_\infty x}{\mu} \right) < 10^5 \quad \text{Laminar flow}$$
$$Re_x \left(= \frac{\rho V_\infty x}{\mu} \right) > 10^5 \quad \text{Turbulent flow}$$

where x is the distance from the leading edge of the plate.

For values of Reynolds number between 10^5 and 10^6 the situation is complicated by two factors. Firstly, the transition is not sharp, it occurs over a finite length of plate. In the transition region the flow may intermittently take on turbulent and laminar characteristics. Secondly, the position of the transition zone depends not only upon the Reynolds number; it is also influenced by the nature of the flow in the free stream and the nature of the surface. Surface roughness or protuberances on the surface tend to trip the boundary layer from laminar to turbulent.

For flow in pipes, channels or ducts the situation is similar to that for a flat plate in the entry region, but in long channels the boundary layers from all walls meet and fully developed temperature and velocity profiles are established.

For fully developed flow in pipes or channels the transition from laminar to turbulent flow occurs at a Reynolds number, $Re_d = (\rho v d_e / \mu)$ of approximately 2100. The dimension d_e is the channel equivalent or hydraulic diameter:

(2.17a) $\quad d_e = \frac{4 \times \text{cross-sectional area}}{\text{wetted perimeter}}$

As expected, for a circular duct or pipe, diameter d, this is given by:

(2.17b) $\quad d_e = \frac{4\pi d^2/4}{\pi d} = d$

For a square duct, side length x,

(2.17c) $\quad d_e = \frac{4x^2}{4x} = x$

and for a rectangular duct, width *a* and depth *b*:

(2.17d) $d_e = \dfrac{4ab}{2(a+b)}$

For flow through an annulus having inner and outer diameters d_1 and d_2, respectively, the hydraulic diameter may be calculated as:

(2.17e) $d_e = \dfrac{4\pi(d_2^2 - d_1^2)/4}{\pi(d_2 + d_1)} = \dfrac{4\pi(d_2 - d_1)(d_2 + d_1)/4}{\pi(d_2 + d_1)} = (d_2 - d_1)$

which is equal to twice the thickness of the annular gap.

The velocity profile in laminar flow in a tube is parabolic, while in turbulent flow the velocity gradient close to the wall is much steeper, as shown in Fig. 2.12.

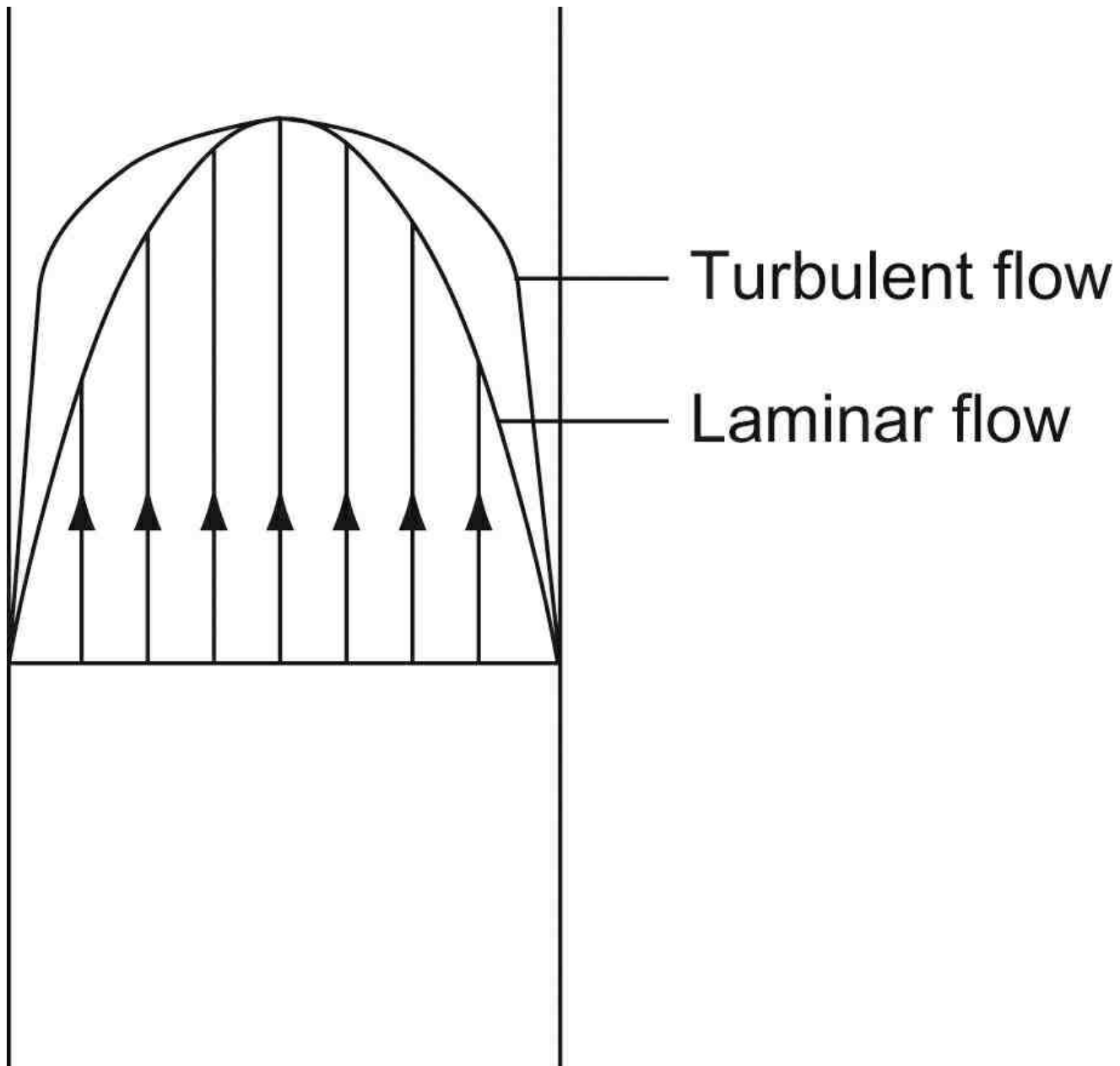
Figure 2.12: Velocity distribution in a circular tube for laminar and turbulent flows

2.3.3.2 Laminar Flow – The Hagen–Poiseuille Equation

The steady state laminar flow of an incompressible fluid of constant viscosity *μ*, through a tube of circular cross section, radius

a, is described by the Hagen–Poiseuille equation.

This equation relates the velocity, v_r of the fluid at radius *r*, to the pressure gradient (dp/dl) along the tube.

(2.18) $\quad v_r = \frac{a^2}{4\mu}\left[1 - \left(\frac{r}{a}\right)^2\right]\left(-\frac{dp}{dl}\right)$

The velocity profile is parabolic, varying from the maximum value, v_m, given by:

(2.19) $\quad v_m = \frac{a^2}{4\mu}\left(-\frac{dp}{dl}\right)$

on the axis of the tube to zero adjacent to the wall.

The average velocity, *v*, is given by:

(2.20) $\quad v = \frac{a^2}{8\mu}\left(-\frac{dp}{dl}\right)$

or rearranging:

$$\frac{dp}{dl} = -\frac{8\mu v}{a^2}$$

In a one-dimensional treatment the average velocity may be used throughout. The volume flowing per second, *S*, is:

(2.21) $\quad S = \pi a^2 v = -\frac{\pi a^4}{8\mu}\left(-\frac{dp}{dl}\right)$

and if ρ is the fluid density the mass flow $\dot{m}$ is given by:

(2.22) $\quad \dot{m} = \rho \pi a^2 v = -\rho\frac{\pi a^4}{8\mu}\left(-\frac{dp}{dl}\right)$

For incompressible, fully developed flow the pressure gradient is constant, so the term ($-dp/dl$) in <u>Eqs (2.18)</u>–<u>(2.22)</u> may be replaced by $((P_1 - P_2)/l)$ where P_1-P_2 is the pressure drop ΔP_f over a length *l* of the channel.

The kinetic head, or flow energy, may be compared to the energy lost due to viscous friction over the channel length *l*. Both may be expressed in terms of the effective pressure difference, ΔP.

The kinetic energy term and the viscous term are given by,

$$\Delta P_{KE} = \frac{1}{2}\rho v^2$$
$$\Delta P_F = \frac{8\mu v}{a^2}$$

respectively.

$$\frac{\Delta P_{KE}}{\Delta P_F} = \frac{\rho v a^2}{16\mu l} = Re\frac{a}{32l} = \frac{Re}{64}\frac{d}{l}$$

Thus, assuming the flow is laminar the kinetic and viscous terms are equal when

(2.23) $\quad l = \frac{Re}{64}d$

For high l/d ratios viscous pressure drop dominates.

2.3.3.3 Turbulent Flow – The Fanning Equation

The frictional pressure drop for turbulent flow is usually related to the average fluid velocity by the Fanning equation:

(2.24a) $\quad \left(-\frac{dp}{dl}\right) = \frac{4}{d}f\frac{1}{2}\rho v^2$

(2.24b) $\quad \frac{P_1 - P_2}{l} = \frac{4}{d}f\frac{1}{2}\rho v^2$

where *f* is the Fanning friction factor.

f is related to the Reynolds number in the turbulent region and a commonly used relationship is the Blasius equation.

(2.25) $\quad f = \dfrac{0.0791}{Re^{0.25}}, \quad 2100 < Re < 10^5$

The Fanning equation may be applied to laminar flow if

(2.26) $\quad f = \dfrac{16}{Re}, \quad Re < 2100$

2.3.4 Flow in Wicks

2.3.4.1 Pressure Difference in the Liquid Phase

The flow regime in the liquid phase is almost always laminar. Since the liquid channels will not in general be straight nor of circular cross section and will often be interconnected, the Hagen–Poiseuille equation must be modified to take account of these differences.

Since mass flow will vary in both the evaporator and the condenser region, an effective length rather than the geometrical length must be used for these regions. If the mass change per unit length is constant the total mass flow will increase, or decrease, linearly along the regions, being zero at the end. We can therefore replace the lengths of the evaporator l_e and the condenser l_c by $(l_e/2)$ and $(l_c/2)$. The total effective length for fluid flow will then be l_{eff} where:

(2.27) $\quad l_{eff} = l_a + \dfrac{l_e + l_c}{2}$

Tortuosity within the capillary structure must be taken into account separately and is discussed below.

There are three principal capillary geometries.

1. Wick structures consist of a porous structure made up of interconnecting pores. Gauzes, felts and sintered wicks come under this heading; these are frequently referred to as homogeneous wicks.

2. Open grooves.

3. Covered channels consist of an area for liquid flow closed by a finer mesh capillary structure. Grooved heat pipes with gauze covering the groove, and arterial wicks are included in this category. These wicks are sometimes described as composite wicks.

Some typical wick sections are shown in Fig. 2.13 and expressions for pressure drop within particular structures are discussed.
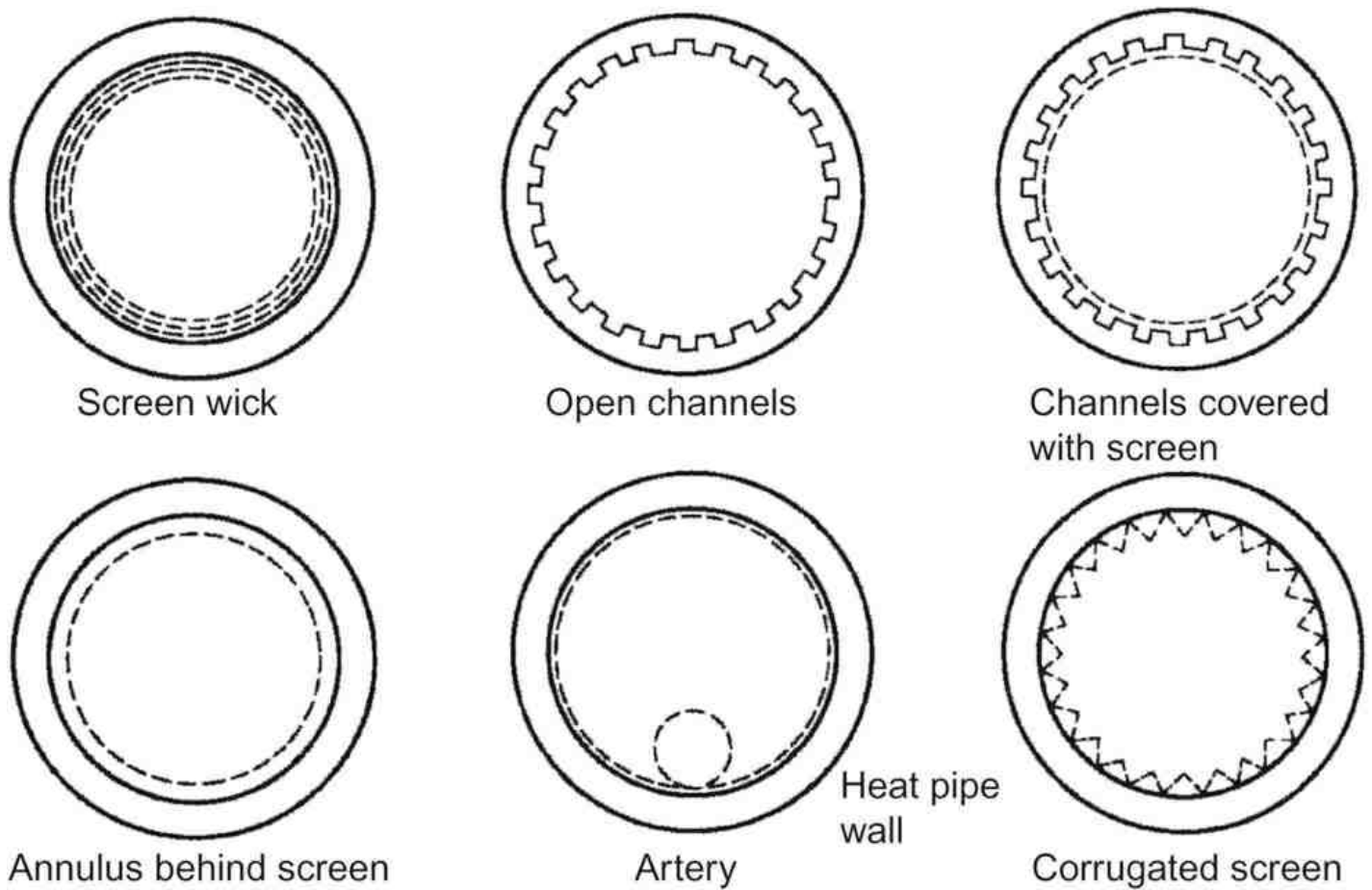
Figure 2.13: A selection of wick sections

Recent innovations in wick design may involve the use of nanoparticles to modify the surface characteristics of the wick, and it is reported [14] that this can result in a reduction in heat transfer overall resistance. It has been demonstrated that nanostructured microposts can be fabricated [15] which give excellent capillary performance and improvements in both heat transfer coefficient and critical heat flux [16].

2.3.4.2 Homogeneous Wicks

If ε is the fractional void of the wick, that is the fraction of the cross section available for the fluid flow, then the total flow cross-sectional area A_f is given by:

(2.28) $\quad A_f = A\varepsilon = \pi(r_w^2 - r_v^2)\varepsilon$

where r_w and r_v are the outer and inner radius of the wick, respectively.

If r_c is the effective pore radius, then the Hagen–Poiseuille equation (Eq. (2.22)) may be written as:

(2.29) $\quad \dot{m} = \dfrac{\pi(r_w^2 - r_v^2)\varepsilon r_c^2 \rho_l}{8\mu_l}\dfrac{\Delta P_l}{l_{eff}}$

or, relating the heat and mass flows, $\dot{Q} = \dot{m}L$, where L is the latent heat of vaporisation and rearranging:

(2.30) $\quad \Delta P_l = \dfrac{8\mu_l \dot{Q}l_{eff}}{\pi(r_w^2 - r_v^2)\varepsilon r_c^2 \rho_l L}$

For porous media, Eq. (2.30) is usually written:

(2.31) $\quad \Delta P_l = \dfrac{b\mu_l \dot{Q}l_{eff}}{\pi(r_w^2 - r_v^2)\varepsilon r_c^2 \rho_l L}$

The number 8, derived for round tubes, is replaced by the dimensionless constant, b, typically $10<b<20$ to include a correction for tortuosity.

Whilst this relation can be useful for a theoretical treatment, it contains three constants, b, ε and r_c, which are all difficult to measure in practice. It is therefore useful to relate the pressure drop and flow rate for a wick structure by using a form of Darcy's 'Law':

(2.32) $\quad \Delta P_l = \dfrac{\mu_l l_{eff} \dot{m}}{\rho_l K A}$

where K is the wick permeability.

Comparison of Eq. (2.32) with Eq. (2.31) shows that Darcy's 'Law' is the Hagen–Poiseuille equation with correction terms included in the constant K to take account of pore size, pore distribution and tortuosity. It serves to provide a definition of permeability, K, a quantity which can be easily measured.

The Blake–Kozeny equation is sometimes used in the literature. This equation relates the pressure gradient across a porous body, made up from spheres diameter D, to the flow of liquid. Like Darcy's 'Law' it is merely the Hagen–Poiseuille equation with correction factors. The Blake–Kozeny equation may be written as:

(2.33) $\quad \Delta P_l = \dfrac{150 \mu_l (1-\varepsilon')^2 l_{eff} \, v}{D^2 \varepsilon'^3}$

and is applicable only to laminar flow, which requires that:

$Re' = \dfrac{\rho v D}{\mu (1-\varepsilon')} < 10$

where v is the superficial velocity $\dot{m}/\rho_l A$ and $\varepsilon' = (\text{volume of voids/volume of body})$.

2.3.4.3 Non-Homogeneous Wicks

Longitudinal groove wick. For grooved wicks the pressure drop in the liquid is given by:

(2.34) $\quad \Delta P_l = \dfrac{8 \mu_l \dot{Q} l}{\pi ((1/2) d_e)^4 N \rho_l L}$

where N is the number of grooves, and d_e is the effective diameter defined by Eq. (2.17).

At high vapour velocities shear forces will tend to impede the liquid flow in open grooves. This may be avoided by using a fine pore screen to form a composite wick structure.

Composite wicks. Such a system as arterial or composite wicks require an auxiliary capillary structure to distribute the liquid over the evaporator and condenser surfaces.

The pressure drop in wicks constructed by an inner porous screen separated from the heat pipe wall to give an annular gap for the liquid flow may be obtained from the Hagen–Poiseuille equation applied to parallel surface, provided that the annular width w is small compared to the radius of the pipe vapour space r_v.

In this case,

(2.35) $\quad \Delta P_l = \dfrac{6 \mu_l \dot{Q} l}{\pi r_v w^3 \rho_l L}$

This wick structure is particularly suitable for liquid metal heat pipes. Variants are also used in lower temperature high performance heat pipes for spacecraft. Crescent annuli may be used, in which it is assumed that the screen is moved down to touch the bottom of the heat pipe wall leaving a gap $2w$ at the top. In this case,

(2.36) $\quad \Delta P_l = \dfrac{6 \mu_l \dot{Q} l}{\pi r_v w^3 \rho_l L}$

In Eqs (2.35) and (2.36) the length should be taken as the effective length defined in Eq. (2.27).

2.3.5 Vapour Phase Pressure Difference, ΔP_v

2.3.5.1 Introduction

The total vapour phase difference in pressure will be the sum of the pressure drops in the three regions of a heat pipe, namely the evaporator drop ΔP_{ve}, the adiabatic section drop ΔP_{va}, and the pressure drop in the condensing region ΔP_{vc}. The problem of calculating the vapour pressure drop is complicated in the evaporating and condensing regions by radial flow due to evaporation or condensation. It is convenient to define a further Reynolds number, the radial Reynolds number:

(2.37) $Re_{\mathrm{r}} = \frac{\rho_v v_r r_v}{\mu_v}$

to take account of the radial velocity component v_r at the wick where $r=r_v$.

By convention the vapour space radius r_v is used rather than the vapour space diameter which is customary in the definition of axial Reynolds number. Re_r is positive in the evaporator section and negative in the condensing section. In most practical heat pipes Re_r lies in the range 0.1–100.

Re_r is related to the radial rate of mass injection or removal per unit length $(d\dot{m}/dz)$ as follows:

(2.38) $Re_{\mathrm{r}} = \frac{1}{2\pi\mu_v} \frac{d\dot{m}}{dz}$

The radial and axial Reynolds numbers are related for uniform evaporation or condensation rates, by the equation,

(2.39) $Re_{\mathrm{r}} = \frac{Re\, r_v}{4\ z}$

where z is the distance from either the end of the evaporator section or the end of the condenser section.

In Section 2.3.3.2 we showed in Eq. (2.23), that, provided the flow is laminar, the pressure drop due to viscous forces in a length l is equal to the kinetic head when

(2.40) $l = \frac{Re\, d}{64} = \frac{Re\, r_v}{32}$

If we substitute:

$Re = \frac{4Re_{\mathrm{r}}l}{r_v}$

for the evaporator or condenser region we find that the condition reduces to

(2.41) $Re_{\mathrm{r}} = 8$

Figure 2.14, taken from Busse [17], shows Re_r as a function of power/unit length for various liquid metal working fluids. Clearly, the kinetic head may be a significant component of the vapour pressure drop in the evaporator, and result in an appreciable pressure rise in the condenser when working with liquid metals.
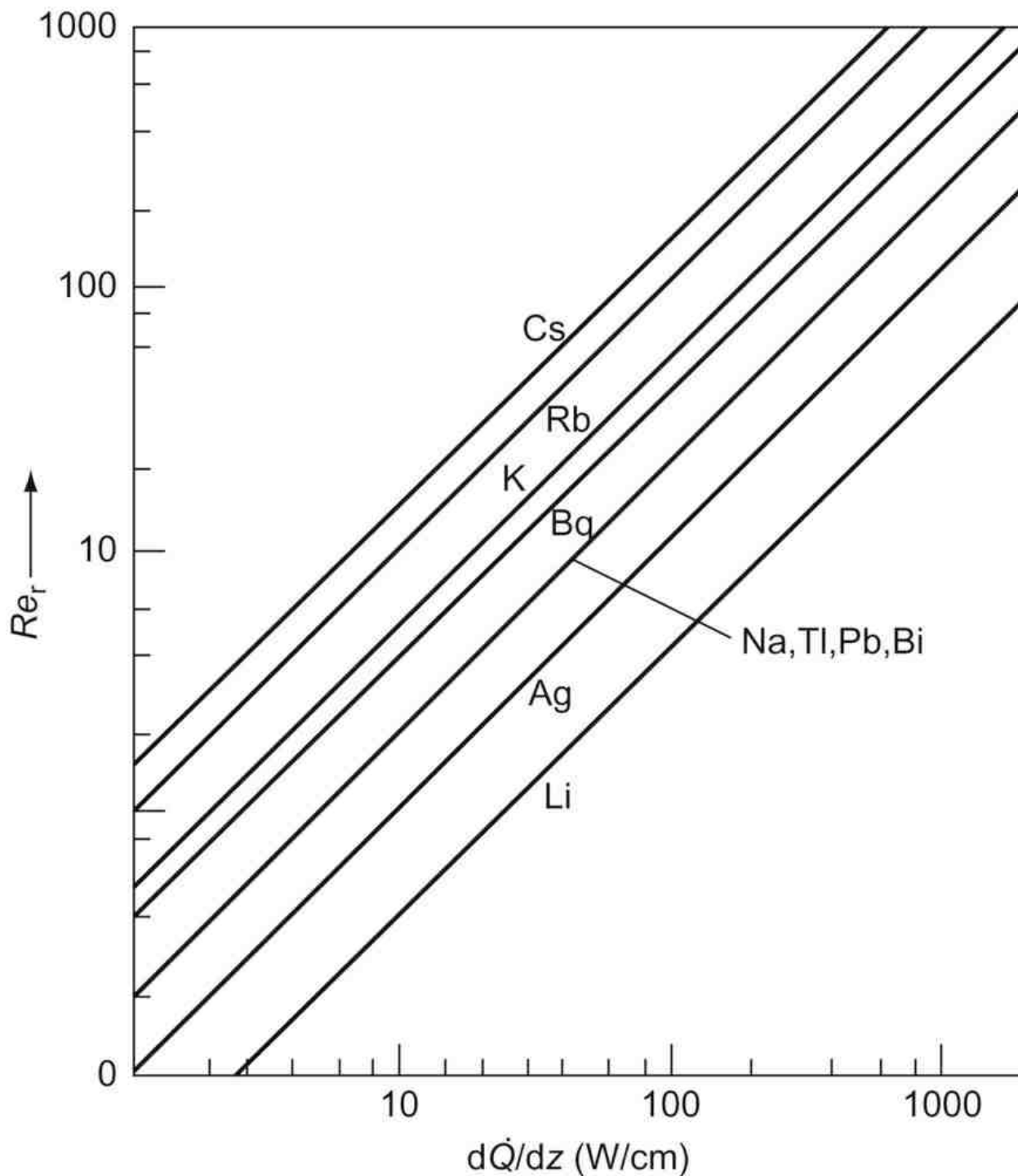
Figure 2.14: Radial Reynolds number versus heat input per unit length of heat pipe (liquid metal working fluids) [17]

2.3.5.2 Incompressible Flow: Simple One-Dimensional Theory

In the following treatment we will regard the vapour as an incompressible fluid. This assumption implies that the flow velocity v is small compared to the velocity of sound c, in the vapour, i.e. the Mach number:

$$\frac{v}{c} < 0.3$$

Alternatively, this condition implies that the treatment is valid for heat pipes in which ΔP_v is small compared with P_v, the average vapour pressure in the pipe. This assumption is not necessarily valid during start-up, nor is it always true in the case of high-temperature liquid metal heat pipes. The effect of compressibility of the vapour will be considered in Section 2.3.5.6.

In the evaporator region the vapour pressure gradient will be necessary to carry out two functions.

i. To accelerate the vapour entering the evaporator section up to the axial velocity *v*. Since, on entering the evaporator, this vapour will have radial velocity but no axial velocity. The necessary pressure gradient we will call the inertial term $\Delta P'_v$.

ii. To overcome frictional drag forces at the surface $r=r_v$ at the wick. This is the viscous term $\Delta P''_v$.

We can estimate the magnitude of the inertial term as follows. If the mass flow/unit area of cross section at the evaporator is ρv then the corresponding momentum flux/unit will be given by $\rho v \times v$ or ρv^2. This momentum flux in the axial direction must be provided by the inertial term of the pressure gradient.

Hence:

(2.42) $\Delta P'_v = \rho v^2$

Note that $\Delta P'_v$ is independent of the length of the evaporator section. The way in which $\Delta P'_v$ varies along the length of the evaporator is shown in Fig. 2.15(a). If we assume laminar flow, we can estimate the viscous contribution to the total evaporator pressure loss by integrating the Hagen–Poiseuille equation. If the rate of mass entering the evaporator per unit length $d\dot{m}/dz$ is constant we find by integrating Eq. (2.22) along the length of the evaporator section:

(2.43) $\Delta P''_v = \dfrac{8\mu_v \dot{m} l_e}{\rho_v \pi r_v^4} \dfrac{1}{2}$
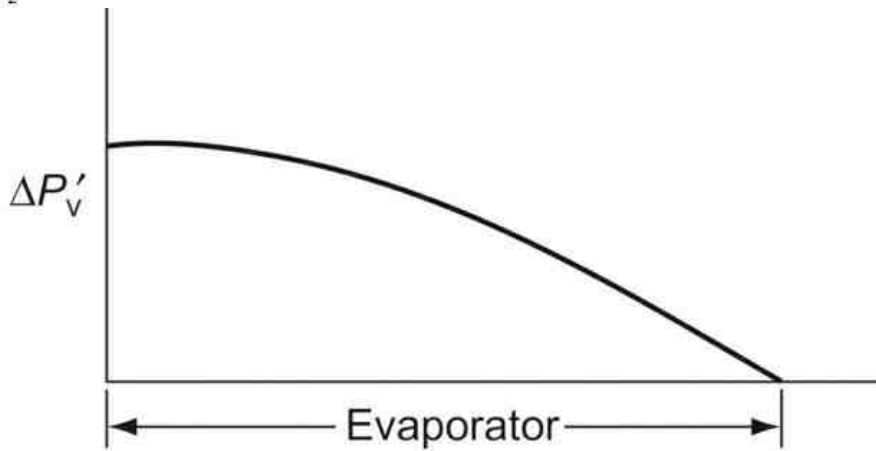
(a) Pressure variation along the evaporator
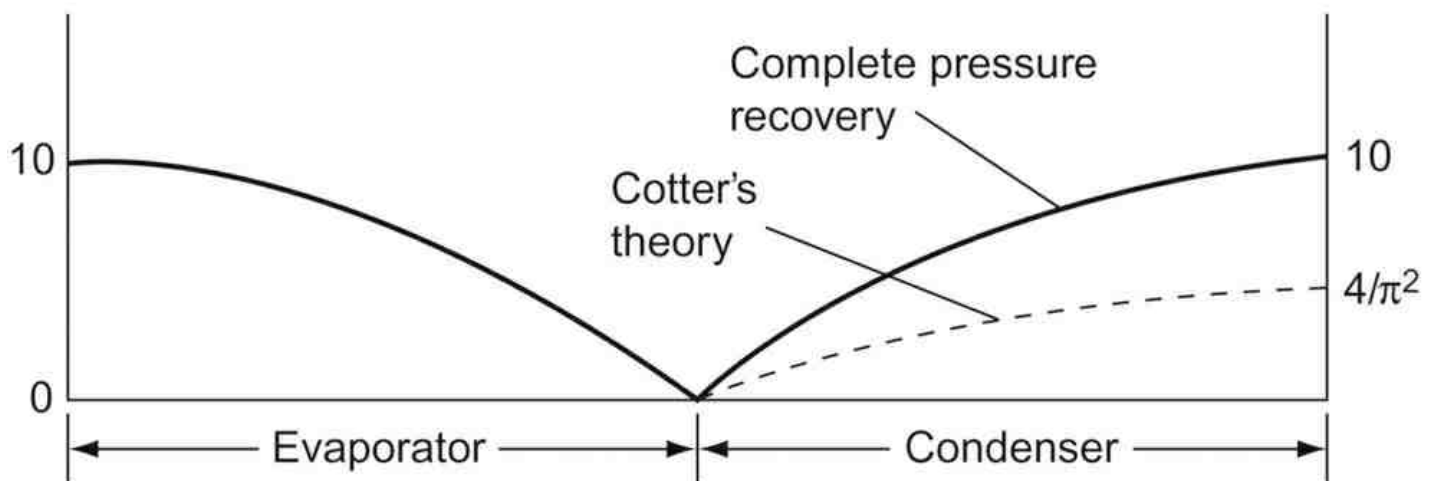
(b) Pressure recovery of inertial pressure term (Adiabatic section omitted)

Figure 2.15: Vapour pressure change due to inertial effects

Thus the total pressure drop in the evaporator region ΔP_{ve} will be given by the sum of the two terms:

(2.44) $\Delta P_{vc} = \Delta P'_v + \Delta P''_v$

$\Delta P_{vc} = \rho v^2 + \dfrac{8\mu_v \dot{m}}{\rho \pi r_v^4} \dfrac{l_c}{2}$

The condenser region may be treated in a similar manner, but in this case axial momentum will be lost as the vapour stream is brought to rest so the inertial term will be negative, that is there will be pressure recovery. For the simple theory the two inertial terms will cancel and the total pressure drop in the vapour phase will be due entirely to the viscous terms. It is shown later that it is not always possible to recover the initial pressure term in the condensing region.

In the adiabatic section the pressure difference will contain only the viscous term which will be given either by the Hagen–Poiseuille equation or the Fanning equation depending on whether the flow is laminar or turbulent.

For laminar flow:

(2.45) $\Delta P_{va} = \dfrac{8\mu_v \dot{m}}{\rho \pi r_v^4} l_a \quad Re < 2100$

For turbulent flow:

(2.46) $\Delta P_{va} = \dfrac{2}{r_v} f \dfrac{1}{2} \rho_v v^2 l_a \quad Re > 2100$

where $f = (0.0791/Re^{0.25}), \quad 2100 < Re < 10^5$ (Eq. (2.25)).

Hence the total vapour pressure drop, ΔP_v is given by:

(2.47) $\Delta P_v = \Delta P_{ve} + \Delta P_{vc} + \Delta P_{va}$

$= \rho v^2 + \dfrac{8\mu_v \dot{m}}{\rho \pi r_v^4}\left[\dfrac{l_e + l_c}{2} + l_a \right]$

for laminar flow with no pressure recovery, and

(2.48) $\Delta P_v = \Delta P_{ve} + \Delta P_{vc} + \Delta P_{va}$

$= \dfrac{8\mu_v \dot{m}}{\rho \pi r_v^4}\left[\dfrac{l_e + l_c}{2} + l_a \right]$

for laminar flow with full pressure recovery.

Equations (2.47) and (2.48) enable the calculation of vapour pressure drops in simple heat pipe design and are used extensively.

2.3.5.3 Incompressible Flow – One-Dimensional Theories of Cotter and Busse

In addition to the assumption of incompressibility the above treatment assumes a fully developed flow velocity profile and complete pressure recovery. It does, however, give broadly correct results. A considerable number of papers have been published giving a more precise treatment of the problem. Some of these will now be summarised in this and the following section.

The earliest theoretical treatment of the heat pipe was by Cotter [1]. For $Re_r \ll 1$ Cotter used the following result obtained by Yuan and Finkelstein for laminar incompressible flow in a cylindrical duct with uniform injection or suction through a porous wall.

$\dfrac{dP_v}{dz} = \dfrac{8\mu_v \dot{m}}{\pi \rho_v r_v^4}\left[1 + \dfrac{3}{4}Re_r - \dfrac{11}{270}Re_r^2 \right]$

He obtained the following expression:

(2.49) $\Delta P_{ve} = \dfrac{4\mu_v l_e \dot{Q}}{\pi \rho_v r_v^4 L}$

which is equivalent to Eq. (2.43).

For $Re_r \gg 1$ Cotter used the pressure gradient obtained by Knight and McInteer for flow with injection or suction through porous parallel plane walls. The resulting expression for pressure gradient is:

$$\Delta P_{ve} = \frac{\dot{m}^2}{8\rho_v r_v^4}$$

which may be rewritten as:

(2.50) $\Delta P_{ve} = \frac{(\rho_v \pi r_v^2 v)^2}{8\rho_v r_v^4} = \frac{\pi^2}{8}\rho_v v^2 \approx \rho_v v^2$

This is equivalent to [Eq. (2.42)](#), derived previously, suggesting that inertia effects dominate the pressure drop in the evaporator.

A different velocity profile was used by Cotter in the condenser region, this gave pressure recovery in the condenser as:

(2.51) $\Delta P_{vc} = -\frac{4}{\pi^2}\frac{\dot{m}^2}{8\rho_v r_v^4}$

which is $4/\pi^2$, or 0.405, of ΔP_{ve}, giving only partial pressure recovery.

In the adiabatic region, Cotter assumed fully developed laminar flow, hence [Eq. (2.46)](#) was used

$$\Delta P_{va} = \frac{8\mu_v \dot{m}}{\rho \pi r_v^4} l_a$$

The full expression for the vapour pressure drop combined [Eqs (2.46)](#), [(2.50)](#) and [(2.51)](#) to give:

(2.52) $\Delta P_v = \left(1 - \frac{4}{\pi^2}\right)\frac{\dot{m}}{8\rho_v r_v^4} + \frac{8\mu_v \dot{m} l_a}{\pi \rho_v r_v^4}$

Busse also considered the one-dimensional case, assuming a modified Hagen–Poiseuille velocity profile and using this to obtain a solution of the Navier–Stokes equation[2][18] for a long heat pipe and obtained similar results.

2.3.5.4 Pressure Recovery

We have seen that the pressure drop in the evaporator and condenser regions consists of two terms, an inertial term and a term due to viscous forces. Simple theory suggests that the inertial term will have the opposite sign in the condenser region and should cancel out that of the evaporator ([Fig. 2.15(b)](#)). There is experimental evidence for this pressure recovery. Grover et al. [19] provided an impressive demonstration with a sodium heat pipe. In these experiments they achieved 60% pressure recovery. The radial Reynolds number was greater than 10. For simplicity in [Fig. 2.15(b)](#) the viscous component of pressure drop has been omitted. The liquid pressure drop is also shown in [Fig. 2.16(a)–(c)](#). Ernst [20] has pointed out that if the pressure recovery in the condenser region is greater than the liquid pressure drop, [Fig. 2.16(b)](#), then the meniscus in the wick will be convex. Whilst this is possible in principle, under normal heat pipe operation there is excess in the condenser region so that this condition cannot occur. For this reason if $|\Delta P_{vc}| > |\Delta P_{lc}|$ it is usual to neglect pressure recovery and assume that there is no resultant pressure drop or gain in the condenser region, as indicated in [Fig. 2.16(c)](#).
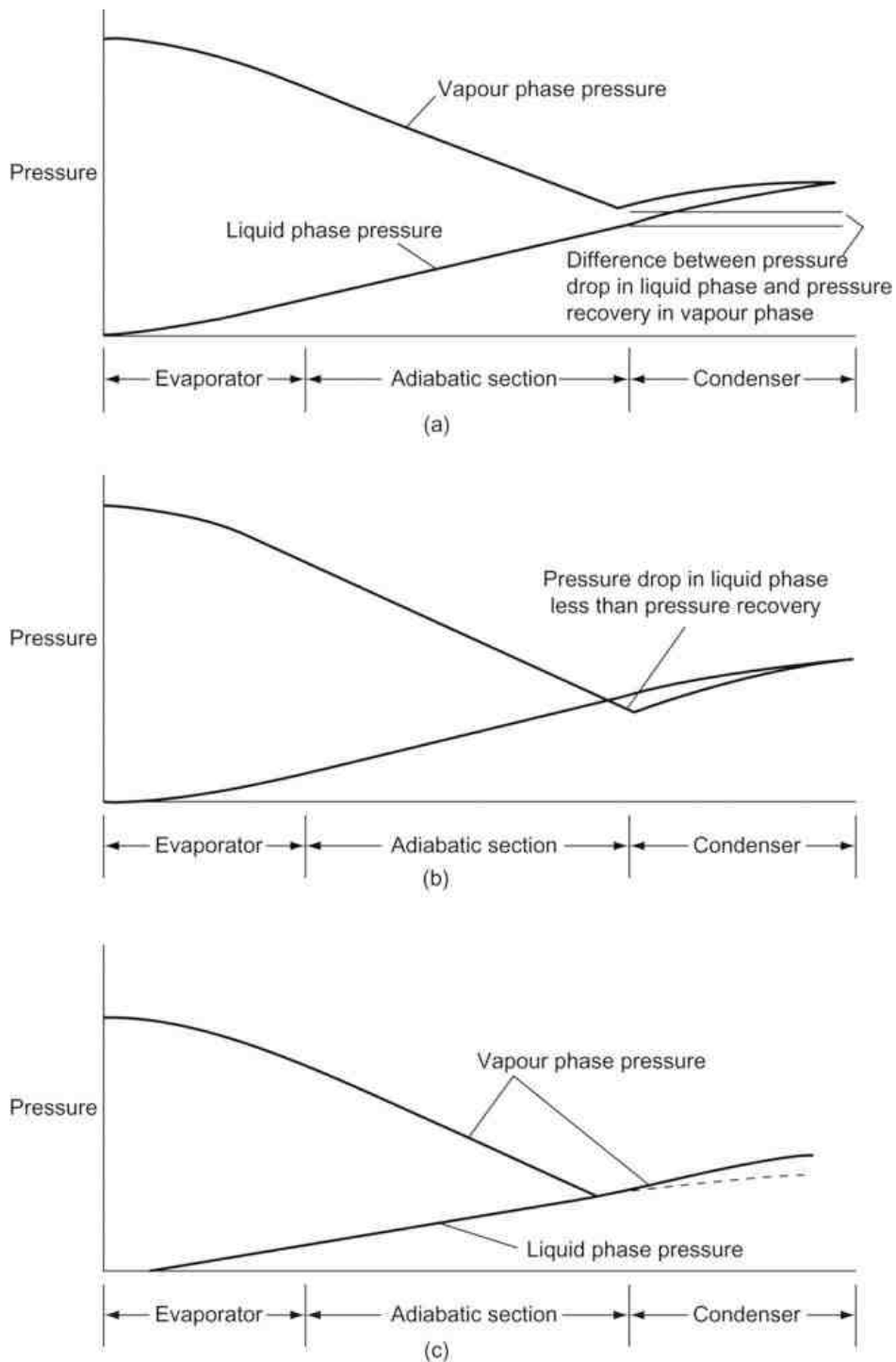
Figure 2.16: Pressure profiles showing pressure recovery in a heat pipe [20]

2.3.5.5 Two-Dimensional Incompressible Flow

The previous discussion has been restricted to one-dimensional flow. In practical heat pipes the temperature and pressure are not constant across the cross section and this variation is particularly important in the condenser region. A number of authors have considered this two-dimensional problem. Bankston and Smith [21] and Rohani and Tien [22] have solved the Navier–Stokes equation by numerical methods. Bankston and Smith showed that axial velocity reversal occurred at the end of the condenser section under conditions of high evaporation and condensation rates. Reverse flow occurs for $|Re_r| > 2.3$. In spite of this extreme divergence from the assumption of uniform flow, one-dimensional analyses yield good results for $|Re_r| < 10$. This is illustrated in Fig. 2.17.
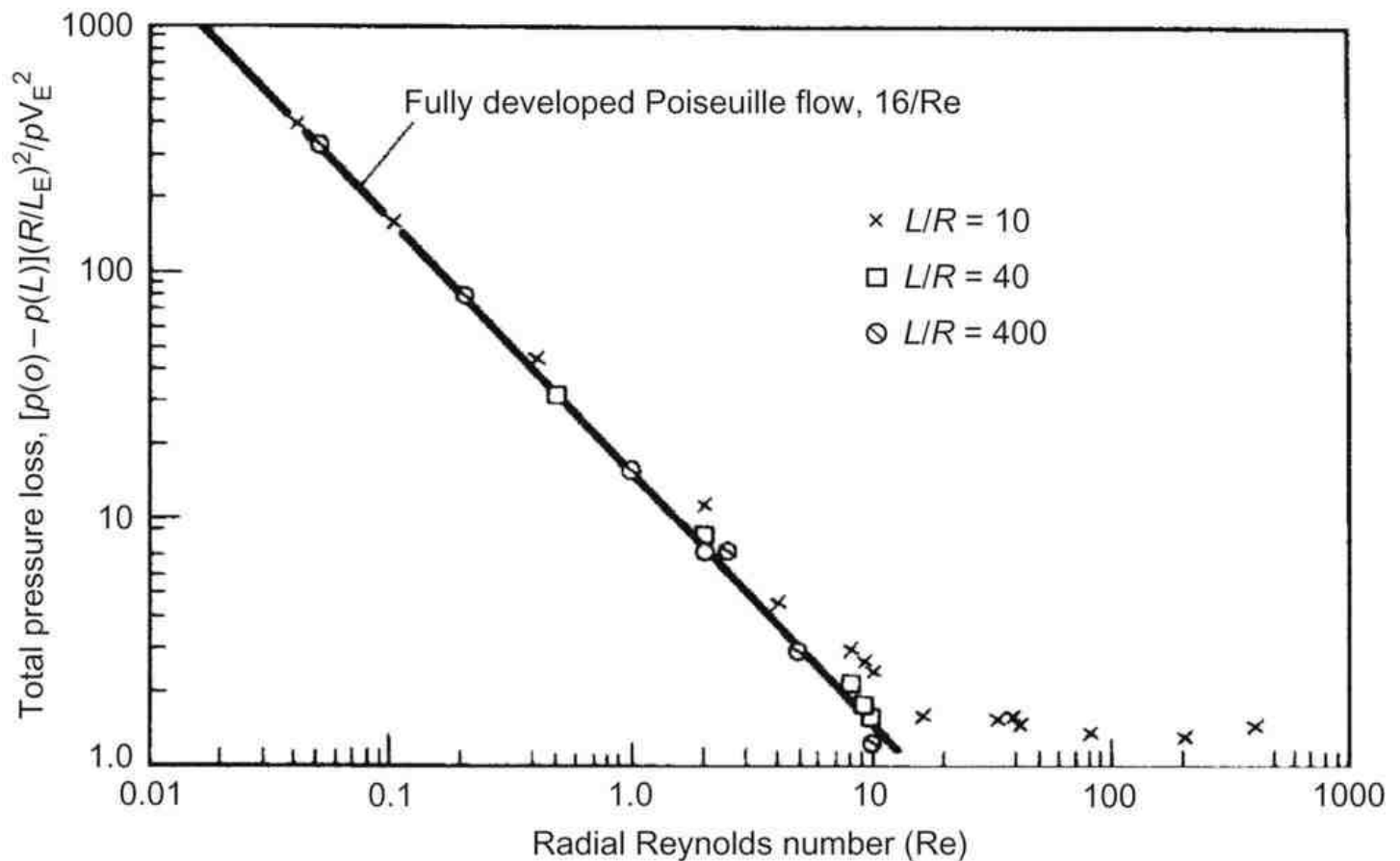
Figure 2.17: Comparison of pressure loss in symmetrical heat pipes with that predicted for Poiseuille flow [21]

2.3.5.6 Compressible Flow

So far we have neglected the effect of compressibility of the vapour on the operation of the heat pipe. Compressibility can be important during start-up and also in high-temperature liquid metal heat pipes; it is discussed in this section.

In a cylindrical heat pipe the axial mass flow increases along the length of the evaporator region to a maximum value at the end of the evaporator; it will then decrease along the condenser region. The flow velocity will rise to a maximum value at the end of the evaporator region where the pressure will have fallen to a minimum. Deverall et al. [23] have drawn attention to the similarity in flow behaviour between such a heat pipe and that of a gas flowing through a converging-diverging nozzle. In the former the area remains constant but the mass flow varies, whereas in the latter the mass flow is constant but the cross-sectional area is changed. It is helpful to examine the behaviour of the convergent-divergent nozzle in more detail before returning to the heat pipe. Let the pressure of the gas at the entry to the nozzle be kept constant and consider the effect of reducing the pressure at the outlet. With reference to the curves in Fig. 2.18 we can see the effect of increasing the flow through a nozzle. For the flow of Curve A, the pressure difference between inlet and outlet is small. The gas velocity will increase to a maximum value in the position of minimum cross section, or throat, falling again in the divergent region. The velocity will not reach the sonic value. The pressure passes through a minimum in the throat. If the outlet pressure is now reduced the flow will increase and the situation shown in Curve B can be attained. Here the velocity will increase through the convergent region, rising to the sonic velocity in the throat. As before, the velocity will reduce during travel through the diverging section and there will be some pressure recovery. If the outlet pressure is further reduced the flow rate will remain constant and the pressure profile will follow Curve C. The gas will continue to accelerate after entering the divergent region and will become supersonic. Pressure recovery will occur after a shock front. Curve D shows that for a certain exit pressure the gas can be caused to accelerate throughout the diverging region. Further pressure reduction will not affect the flow pattern in the nozzle region. It should be noted that after Curve C pressure reduction does not affect the flow pattern in the converging section, hence the mass flow does not increase after the throat velocity has attained the sonic value. This condition is referred to as choked flow.
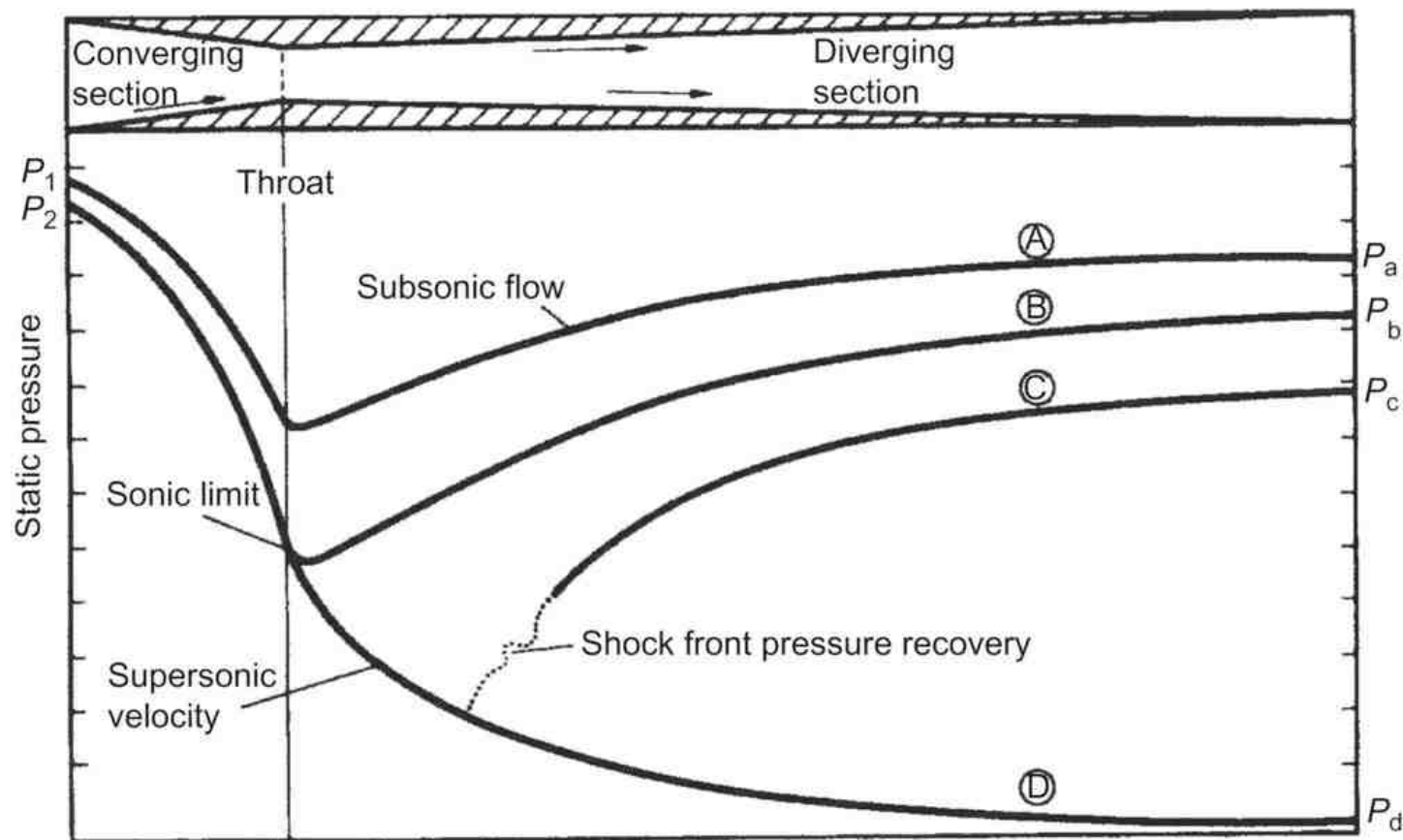
Figure 2.18: Pressure profiles in a converging-diverging nozzle

Kemme [24] has shown very clearly that a heat pipe can operate in a very similar manner to the diverging nozzle. His experimental arrangement is shown in Fig. 2.19. Kemme used sodium as the working fluid and maintained a constant heat input of 6.4 kW. He measured the axial temperature variation, but since this is related directly to pressure his temperature profile can be considered to be the same as the pressure profile.
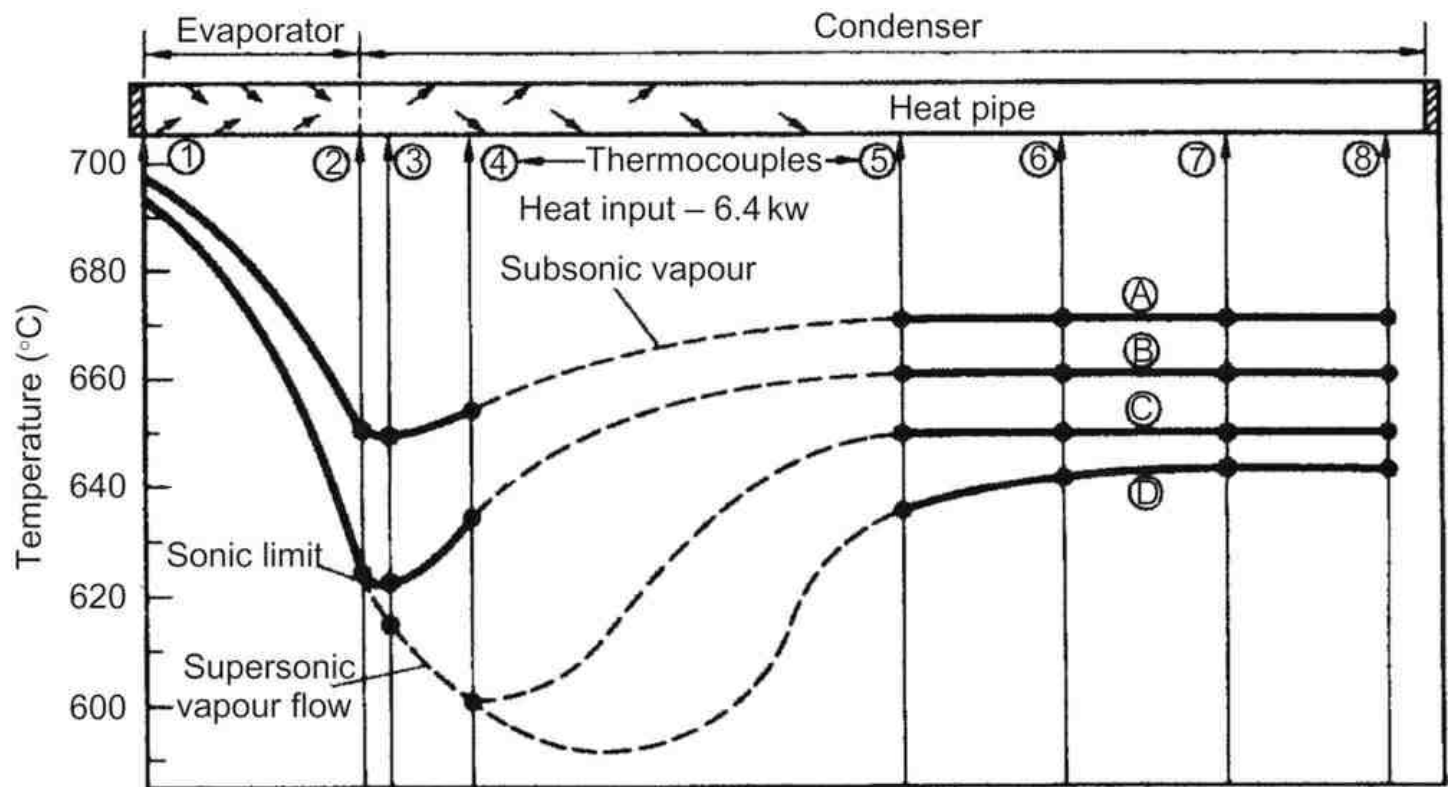
Figure 2.19: Temperature profiles in a sodium heat pipe [24]

Kemme arranged to vary the heat rejection at the condenser by means of a gas gap, the thermal resistance of which could be altered by varying the argon–helium ratio of the gas. Kemme's results are shown in Fig. 2.19. Curve A demonstrates subsonic flow with pressure recovery; Curve B, obtained by lowering the condenser temperature, achieved sonic velocity at the end of the evaporator, and hence operated under choked flow conditions. Further decrease in the thermal resistance between the condenser and heat sink simply reduced the condenser region temperature but did not increase the heat flow which was limited by the choked flow condition and fixed axial temperature drop in the evaporator [25]. It should be noted that under these conditions of sonic limitation considerable axial temperature and pressure changes will exist and the heat pipe operation will be far from isothermal.

Deverall et al. [23] have shown that a simple one-dimensional model provides a good description of the compressible flow behaviour. Consider the evaporator section using the nomenclature of Fig. 2.19.

The pressure $P_1 = P_o$, where P_o is the stagnation pressure of the fluid. The pressure drop along the evaporator is given by Eq. (2.42).

(2.53) $\quad P_2 - P_o = \rho v^2$

The equation state for a gas at low pressure may be written as:

(2.54) $\quad P = \rho_v R T$

and the sonic velocity, C, may be expressed as:

(2.55) $\quad C = \sqrt{\gamma R T}$

The Mach number, M, is defined as:

$$M = \frac{v}{C}$$

Hence, substituting into Eq. (2.53), we get:

(2.56) $\quad \dfrac{P_o}{P_2} - 1 = \dfrac{\rho_v v^2}{P_2} = \dfrac{M^2 \gamma R T_2}{R T_2} = \gamma M^2$

Defining the total temperature T_o such that:

(2.57) $\quad \dot{m} c_p T_o = \dot{m}\left(c_p T_2 + \dfrac{v^2}{2}\right)$

and remembering that $c_p = (\gamma/\gamma - 1)$

(2.58) $\quad \dfrac{T_o}{T_2} = 1 + M^2 \dfrac{\gamma - 1}{2}$

The density ratio may be expressed as:

(2.59) $\quad \dfrac{\rho_o}{\rho_2} = \dfrac{P_o T_2}{P_2 T_o} = \dfrac{1 + \gamma M^2}{1 + (\gamma - 1/\gamma)M^2}$

Finally, the energy balance for the evaporator section gives:

(2.60) $\quad \begin{aligned} \dot{Q} &= \rho_v A v L \\ &= \rho_v A M C L \end{aligned}$

where C is the sonic velocity at T_2. The heat flow may be expressed in terms of the sonic velocity C_o corresponding to the stagnation temperature T_o. In this case:

(2.61) $\quad \dot{Q} = \dfrac{\rho_v A M C_o L}{\sqrt{2(\gamma + 1)}}$

The pressure, temperature and density ratio for choked flow may be obtained by substituting $M=1$ into Eqs (2.59)–(2.61), respectively, and the values are presented in Table 2.2.

Table 2.2: Effect of γ on Compressibility Parameters

	Monatomic Gas	Diatomic Gas	Triatomic Gas
γ	1.66	1.4	1.3

Table 2.2: Effect of γ on Compressibility Parameters

	Monatomic Gas	Diatomic Gas	Triatomic Gas
$\dfrac{P_0}{P_{2,c}} = 1 + \gamma$	2.66	2.4	2.3
$\dfrac{T_0}{T_{2,c}} = \dfrac{1+\gamma}{2}$	1.33	1.2	1.15
$\dfrac{P_0}{\rho_{2,c}} = 2$	2	2	2

The sonic limit is discussed more fully in Ref. [26]. It is noted that the analysis of compressible flow is generally assumed to be either isothermal or isentropic. The authors also propose a model assuming that the conditions remain saturated throughout the adiabatic region. It is concluded that the results obtained are generally close, irrespective of the underlying assumption. However, based on the experimental work of Gangeaux [27] it is important that the appropriate reference temperature is chosen and this should be the temperature at the base of the evaporator.

2.3.5.7 Summary of Vapour Flow

The equations presented in this section permit the designer to predict the pressure drop due to the vapour flow in a heat pipe. These relatively simple equations give acceptable results for most situations encountered within heat pipes. An excellent summary of the analysis of vapour side pressure drop is presented in Ref. [28]. For applications which present exceptional problems, the designer should consider using one of the many computational fluid dynamics computer packages on the market which can deal with three-dimensional and compressible flows.

2.3.6 Entrainment

In a heat pipe the vapour flows from the evaporator to the condenser and the liquid is returned by the wick structure. At the interface between the wick surface and the vapour the latter will exert a shear force on the liquid in the wick. The magnitude of the shear force will depend on the vapour properties and velocity and its action will be to entrain droplets of liquid and transport them to the condenser end. This tendency to entrain is resisted by the surface tension in the liquid. Entrainment will prevent the heat pipe operating and represents one limit to performance. Kemme observed entrainment in a sodium heat pipe and reports that the noise of droplets impinging on the condenser end could be heard.

The Weber number, *We*, which is representative of the ratio between inertial vapour forces and liquid surface tension forces, provides a convenient measure of the likelihood of entrainment.

The Weber number is defined as:

(2.62) $\quad We = \dfrac{\rho_v v^2 z}{2\pi \sigma_1}$

where ρ_v is the vapour density, v is the vapour velocity, σ_1 is surface tension and *z* is a dimension characterising the vapour–liquid surface.

In a wicked heat pipe *z* is related to the wick spacing.

It should be noted that some authors, including Kim and Peterson [29] define the Weber number as

(2.63) $\quad We' = \dfrac{\rho_v v^2 z}{\sigma_1} = 2\pi We$

A review of 11 models of entrainment by Kim and Peterson reported critical Weber numbers (as defined by Eq. (2.63)) principally in the range 0.2–10.

It may be assumed that entrainment may occur when *We* is of the order 1. The limiting vapour velocity, v_c, is thus given by:

(2.64) $\quad v_c = \sqrt{\dfrac{2\pi \sigma_1}{\sigma_v z}}$

and, relating the axial heat flux to the vapour velocity using:

$\dot{q} = \rho_v L v$

The entrainment limited axial flux is given by:

(2.65) $\hat{q} = \sqrt{\dfrac{2\pi\rho_v L^2 \sigma_1}{z}}$

Extracting the fluid properties from Eq. (2.65) suggests $\rho_v L^2 \sigma_1$ as a suitable figure of merit for working fluids from the point of view of entrainment.

Cheung [30] has plotted this figure of merit against temperature for a number of liquid metals, and this is reproduced as Fig. 2.20.
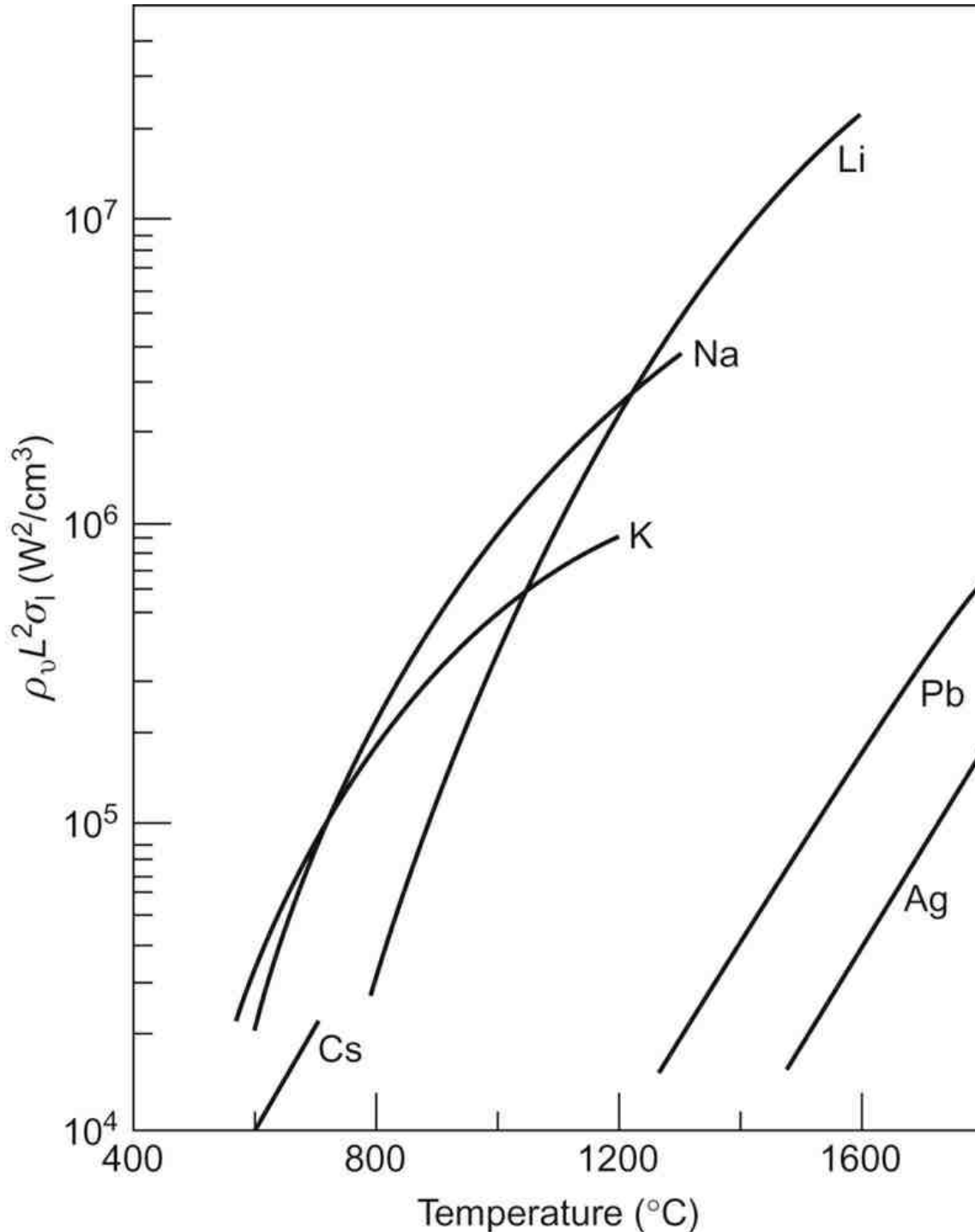
Figure 2.20: Entrainment merit number for liquid metals [30]

A number of authors report experimental results on the entrainment limit. Typically, they select a value of *z* which fits their results and show that the temperature dependence of the limit is as predicted by Eq. (2.65).

Kim and Peterson [29] used the Weber number:

(2.66) $We' = \frac{\rho_v v^2 z}{\sigma_1}$

defined in Eq. (2.63), and the viscosity number

(2.67) $N_{vl} = \frac{\mu_l}{\sqrt{\rho_l \sigma_l \lambda_c / 2\pi}}$

where λ_c is the critical wavelength derived from the Rayleigh–Taylor instability [31]. N_{vi} represents the stability of a liquid interface. They derived a correlation, Eq. (2.68), from their experimental measurements with water on mesh wicks for the critical Weber number:

(2.68) $We_{vc} = 10^{-1.163} N_{vl}^{-0.744} \left(\frac{\lambda_c}{d_1}\right)^{-0.509} \left(\frac{D_h}{d_2}\right)^{0.276}$

where d_1 and d_2 are the mesh wire spacing and thickness, respectively, and D_h is the equivalent diameter of the vapour space.

2.3.7 Heat Transfer and Temperature Difference

2.3.7.1 Introduction

In this section we consider the transfer of heat and the associated temperature drops in a heat pipe. The latter can be represented by thermal resistances and an equivalent circuit is shown in Fig. 2.21.

Figure 2.21: Temperature drops and equivalent thermal resistances in a heat pipe

Heat can both enter and leave the heat pipe by conduction from a heat source/sink, by convection or by thermal radiation. The

pipe may also be heated by eddy currents or by electron bombardment, and cooled by electron emission. Further temperature drops will occur by thermal conduction through the heat pipe walls at both the evaporator and condenser regions. The temperature drops 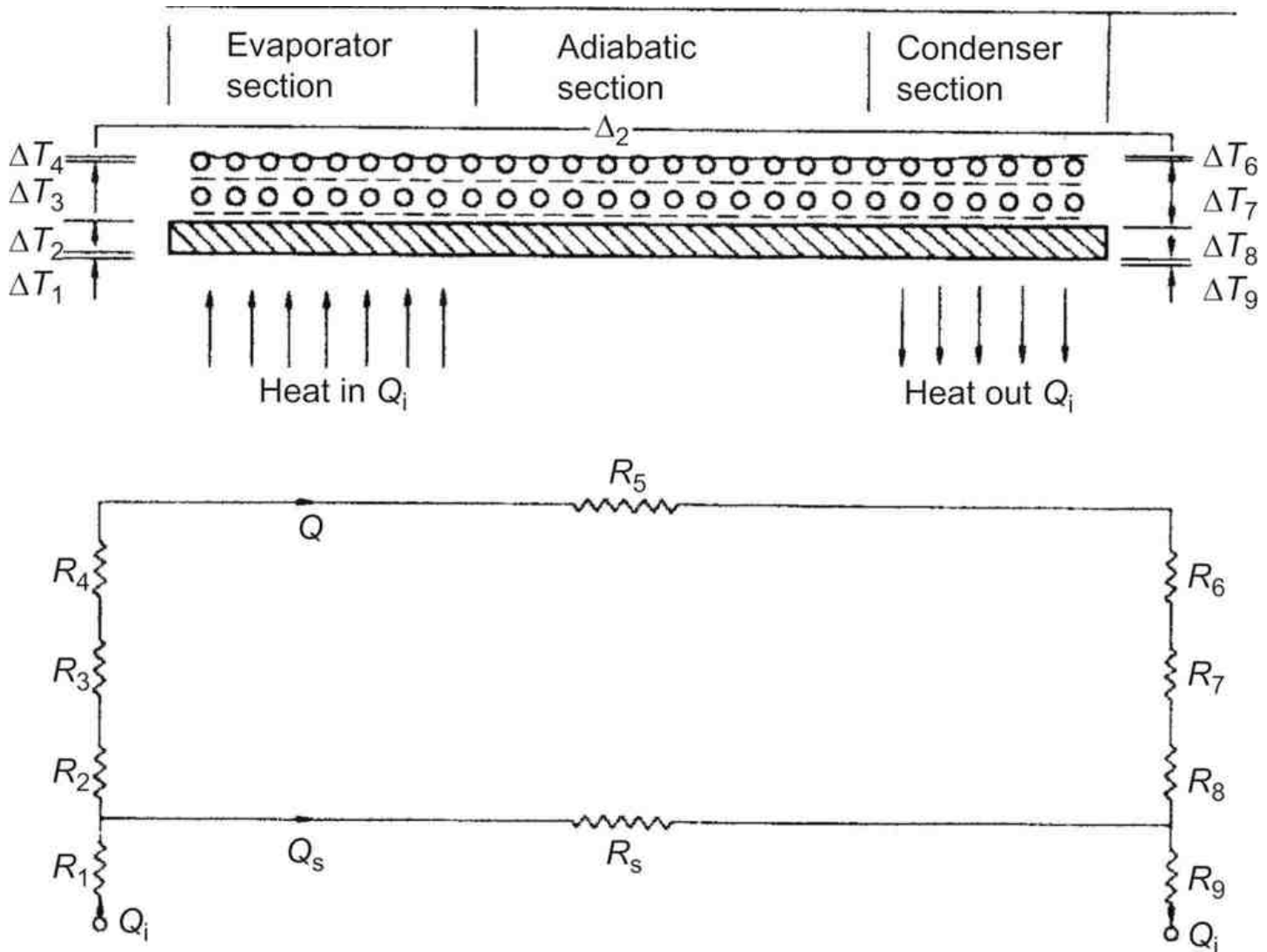through the wicks arise in several ways and are discussed in detail later in this section. It is found that a thermal resistance exists at the two vapour–liquid surfaces and also in the vapour column. The processes of evaporation and condensation are examined in some detail both in order to determine the effective thermal resistances and also to identify the maximum heat transfer limits in the evaporator and condenser regions. Finally the results for thermal resistance and heat transfer limits are summarised for the designer.

2.3.7.2 Heat Transfer in the Evaporator Region

For low values of heat flux the heat will be transported to the liquid surface partly by conduction through the wick and liquid and partly by natural convection. Evaporation will be from the liquid surface. As the heat flux is increased the liquid in contact with the wall will become progressively superheated and bubbles will form at nucleation sites. These bubbles will transport some energy to the surface by latent heat of vaporisation and will also greatly increase convective heat transfer. With further increase of flux a critical value will be reached, burnout, at which the wick will dry out and the heat pipe will cease to operate. Before discussing the case of wicked surfaces the data on heat transfer from plane, unwicked surfaces will be summarised. Experiments on wicked surfaces are then described and correlations given to enable the temperature drop through the wick and the burnout flux to be estimated. The subject is complex and further work is necessary to provide an understanding of the processes in detail.

2.3.7.3 Boiling Heat Transfer from Plane Surfaces

In 1934 Nukiyama [32] performed a pool boiling experiment, passing an electric current through a platinum wire immersed in water. The heat flux was controlled by the current through and voltage across the wire and the temperature of the wire was determined from its resistance. Similar results are obtained when boiling from a plane surface or from the surface of a cylinder. An apparatus for measuring pool boiling heat transfer is shown schematically in Fig. 2.22. Nukiyama then proposed a boiling curve of the form shown in Fig. 2.23.

Condenser

Vapour

Liquid

Heated cylinder
(or flat surface)
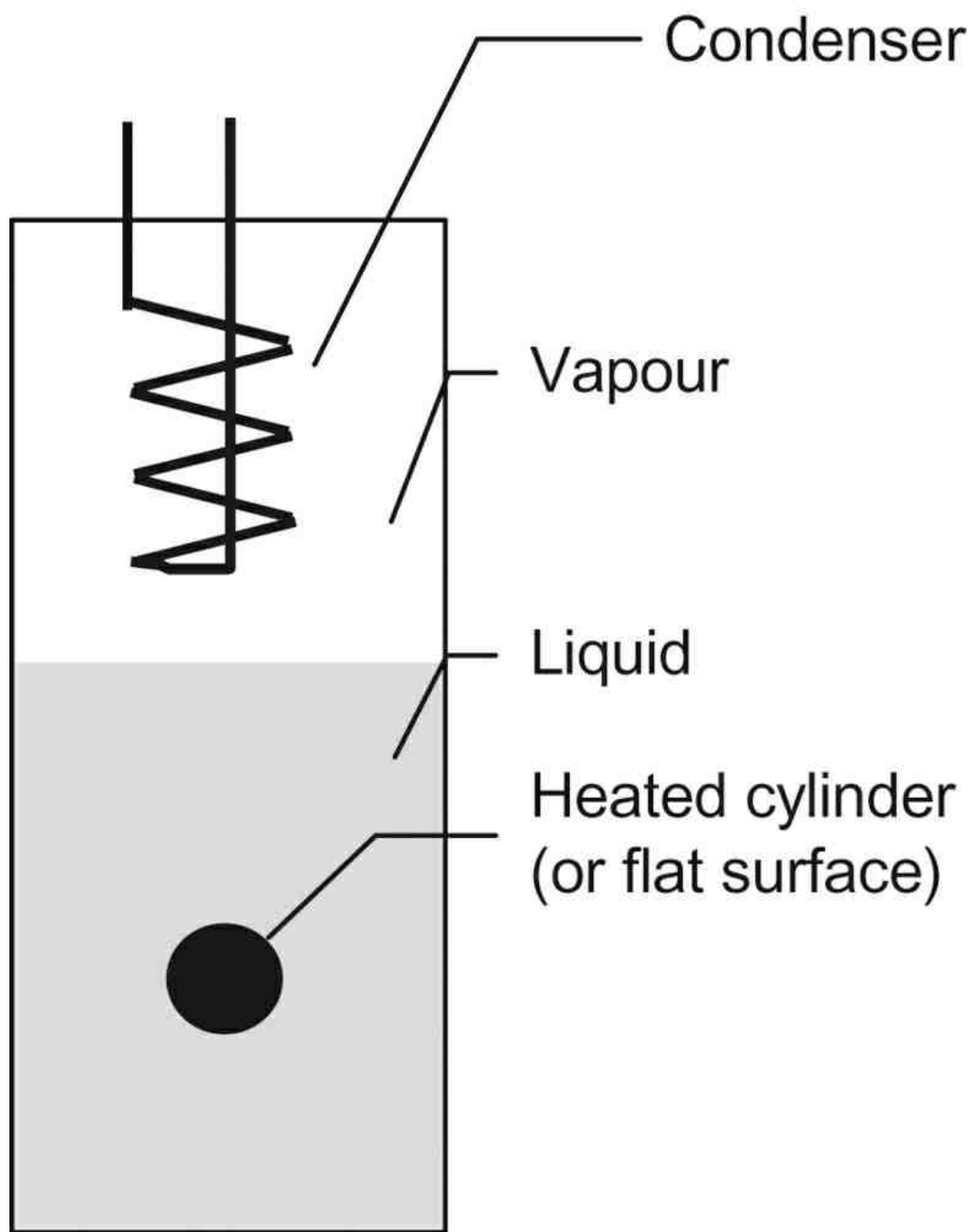
Figure 2.22: Schematic diagram of pool boiling experiment
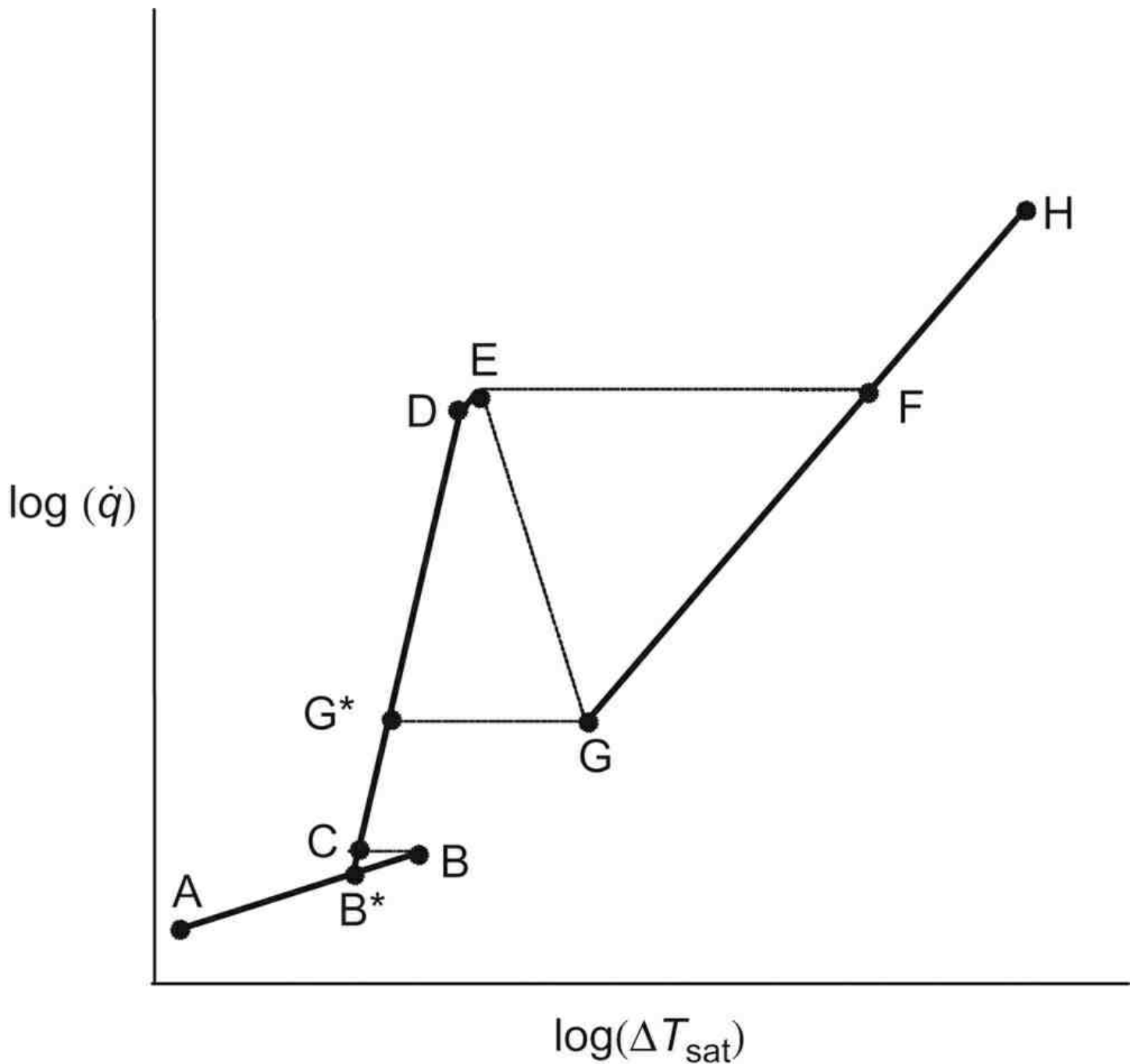
Figure 2.23: Boiling curve for pool boiling from plane surface, cylinder or wire (not to scale)

Since we have a liquid and vapour coexisting in the apparatus, both must be at (or during boiling, very close to) the saturation temperature of the fluid at the pressure in the container. If the surface temperature of the heater, T, the temperature of the fluid, T_{sat}, the rate of energy supply to the heater, $\dot{Q}$, and the heater surface area, A, are measured, then a series of tests may be carried out and a graph of $\log \dot{Q}$, or more usually $\log \dot{q} = \log(\dot{Q}/A)$, is plotted against $\log \Delta T_{sat}$, where $\Delta T_{sat} = (T - T_{sat})$, often referred to as the wall superheat.

For the case of controlled heat flux (e.g. electric heating) the various regimes may be described.

For increasing heat flux, in the region 'A'–'B' heat transfer from the heater surface is purely by single-phase natural convection. Superheated liquid rises to the surface of the reservoir and evaporation takes place at this surface. As the heat flux is increased beyond the value at 'B' bubbles begin to form on the surface of the heater, depart from the heater surface and rise through the liquid; this process is referred to as nucleate boiling. At this stage a reduction of heater surface temperature to 'C' may be observed. Reducing the heat flux would now result in the heat flux temperature difference relationship following the curve 'C'–'B*'. This type of phenomenon, for which the relationship between a dependent and independent variable is different for increasing and decreasing values of the independent variable, is known as hysteresis.

After the commencement of nucleate boiling, further increase in heat flux leads to increased heater surface temperature to point 'D'. Further increase beyond the value at 'D' leads to vapour generation at such a rate that it impedes the flow of liquid back to the surface and transition boiling occurs between 'D' and 'E'. At 'E' a stable vapour film forms over the surface of the heater and this has the effect of an insulating layer on the heater resulting in a rapid increase in temperature from 'E' to 'F'. The heat flux at 'E' is known as the critical heat flux. The large temperature increase which occurs if an attempt is made to maintain the heat flux above the level of the critical heat flux is frequently referred to as burnout. However, if physical burnout does not occur it is possible to maintain boiling at point 'F' and then adjust the heat flux; the heat flux temperature difference relationship will then follow the line 'G'–'H'. This region on the boiling curve corresponds to the stable film boiling regime. Reduction of the heat flux below the value at 'G' causes a return to the nucleate boiling regime at 'G*'.

The factors which influence the shape of the boiling curve for a particular fluid include fluid properties, heated surface characteristics and physical dimensions and orientation of the heater. The previous history of the system also influences the behaviour, particularly at low heat flux.

Clearly several relationships, defining both the extent of each region and the appropriate shape of the curve for that region, are required to describe the entire curve. It is the nucleate boiling region, 'C'–'D', which is of greatest importance in most engineering applications. However, it is clearly important that the designer ensures that the critical heat flux is not inadvertently exceeded, and there are some systems which operate in the film boiling regime. Many correlations describing each region of the boiling curve have been published. Additionally, the temperature difference at which nucleation first occurs, i.e. the temperature at 'C', influences the boiling regime during flow boiling and the hysteresis.

If the temperature of the heater, rather than the heat flux, was to be controlled then increasing temperature above that corresponding to the critical heat flux would result in a decrease in heat flux with increasing temperature from 'E' to 'G', followed by an increase along the line G–H. The point 'G' is sometimes referred to as the Leidenfrost Point. Temperature controlled heating of a surface is found in many heat exchangers and boilers – the temperature of the wall being necessarily below the temperature of the other fluid in the heat exchanger. Experimentally, it is difficult to maintain surface temperatures over a wide range with the corresponding range of heat fluxes. To obtain boiling curves for varying ΔT_{sat} it is usual to plunge an ingot of high conductivity material into a bath of the relevant fluid. The surface temperature is measured directly and the heat flux can then be calculated from the geometry of the ingot and the rate of change of temperature.

This suggests that some feature of the surface encourages bubble nucleation. The explanation for the importance of surface finish lies in the mechanism of bubble formation. It has been observed that nucleation occurs in cavities within the surface; these cavities contain minute bubbles of trapped gas or vapour which act as starting points for bubble growth. This is illustrated schematically in Fig. 3.20. When the bubble leaves the site a small bubble remains in the cavity which acts as the start for the next bubble.

Consideration of idealised nucleation sites allows some indication of their necessary size if they are to play a part in boiling, with reference to an idealised conical cavity as shown in Fig. 2.24.
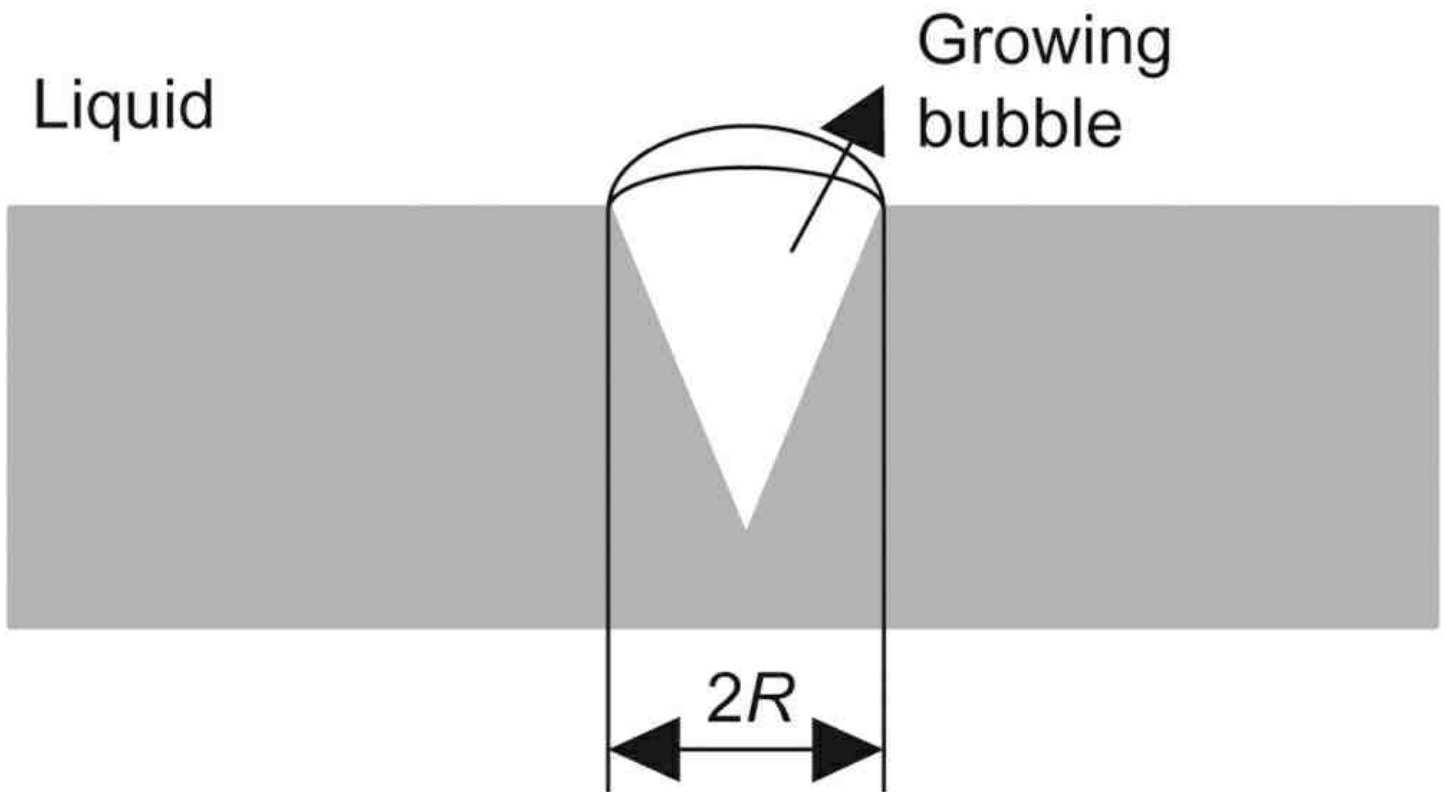
Figure 2.24: Idealised cavity acting as a nucleation site

The pressure, P_B, inside a bubble is somewhat higher than the pressure in the surrounding liquid:

(2.69) $P_B = P + \dfrac{2\sigma_l}{R}$

where P is the liquid pressure, r is the radius of curvature of the bubble and σ_l is the surface tension of the liquid. The radius of curvature is a maximum when the bubble forms a hemispherical cap over the cavity, i.e. $r=R$, the radius of the mouth of the cavity. This is the condition for P_B to be a maximum. If the bubble is to grow then the wall temperature must be sufficiently high to vaporise the liquid at a pressure P_B.

In order for the bubble to grow:

(2.70) $T_W > T_{sat} + \dfrac{dT}{dP}(P_B - P)$

The Clapeyron equation states that the slope of the vapour pressure curve is given by:

(2.71) $\dfrac{dP}{dT} = \dfrac{L}{(v_V - v_l)T_{sat}}$

if v_V is very much greater than v_l we can simplify this as:

(2.72) $\dfrac{dT}{dP} = \dfrac{v_V T_{sat}}{L}$

Hence, for the bubble to grow:

(2.73) $T_W > T_{sat} + \dfrac{2\sigma_l\, v_V T_{sat}}{R}\cdot\dfrac{1}{L} = \dfrac{2\sigma_l}{R}\dfrac{\Delta T_{sat}}{\rho_V L}$

The radius of the cavity and the superheat, ΔT_{sat}, at which nucleation from the cavity starts, can be related as:

(2.74) $R = \dfrac{2\sigma_l T_{sat}}{L \rho_V \Delta T_{sat}}$

For water boiling at 1 bar ΔT_{sat} is commonly of the order of 5 K. Substitution of values for the properties of water gives a value for the smallest active cavity to be approximately 6.5×10^{-6} m radius. This demonstrates that typical active cavities are of the order of 1–10 μm.

Hsu [33] has conducted a more rigorous analysis and showed that

(2.75) $\Delta T = \dfrac{3.06\sigma_l T_{sat}}{\rho_v L \delta}$

where δ is the thermal boundary layer thickness, as a first approximation this may be taken as the average diameter of cavities on the surface. For typical heat pipe evaporators this is approximately 25 μm. Taking δ=25 μm allows the superheat for nucleation to be calculated for various fluids, values of this superheat for various fluids at atmospheric temperature are shown in Table 2.3.

Table 2.3: Superheat for the Initiation of Nucleate Boiling at Atmospheric Pressure, Calculated from Eq. (2.75)

Fluid	Boiling Point (K)	Vapour Density (kg/m^3)	Latent Heat (kJ/kg)	Surface Tension (N/m)	ΔT (°C)
Ammonia (NH_3)	239.7	0.3	1350	0.028	2.0
Ethyl alcohol (C_2H_5OH)	338	2.0	840	0.021	0.51
Water	373	0.60	2258	0.059	1.9
Potassium	1047	0.486	1938	0.067	8.9
Sodium	1156	0.306	3913	0.113	26.4
Lithium	1613	0.057	19700	0.26	44.6

Correlation of data in nucleate boiling region. Nucleate boiling is very dependent on the heated surface and factors such as release of absorbed gas, surface roughness, surface oxidation and wettability greatly affect the surface to bulk liquid temperature difference. The nature of the surface may change over a period of time – a process known as conditioning. (The effect of pressure is also important.) For these reasons reproducibility of results is often difficult. However a number of authors have proposed correlations, some empirical and some based on physical models. Some of these are listed below. The straight line C–D on Fig. 2.23 and experimental results for nucleate boiling indicate that correlations may be represented by an equation of the form:

$\dot{q} = a\Delta T_{sat}^{m}$

This may be rearranged in terms of a heat transfer coefficient, α,

(2.76) $\alpha = \dfrac{\dot{q}}{\Delta T_{sat}} = aT^{m-1}$ or $\alpha = bq^n$

The value of m is generally in the range 3–3.33, corresponding to n being in the range 0.67–0.7.

Rohsenow[34]. An early nucleate boiling correlation is that due to Rohsenow, following the example of turbulent forced convective heat transfer correlations. Rohsenow argued that:

$Nu = f(Re, Pr)$

$Nu = \dfrac{\alpha d}{k_l} \quad Re = \dfrac{\rho_l v d}{\mu} \quad Pr_l = \dfrac{\mu_l c_{pl}}{k_l}$

If the fluid properties are all those for the liquid this still left the problem of choosing a suitable velocity and representative length, d.

The velocity may be taken as the velocity with which the liquid flows towards the surface to replace that which has been vaporised:

$v = \dfrac{\dot{q}}{\rho_l L}$

and the representative length is given by:

$d = \left[\dfrac{\sigma_l}{g(\rho_l - \rho_v)} \right]^{0.5}$

The correlation thus produced was:

$Nu = \dfrac{1}{C_{sf}} Re^{1-x} Pr^{-y}$

which is frequently presented in the form:

(2.77) $\dfrac{c_{pf}\Delta T_{sat}}{L} = C_{sf}\left[\dfrac{\dot{q}}{\mu_l L}\left(\dfrac{\sigma_l}{g(\rho_l - \rho_v)}\right)^{0.5}\right]^{x}\left[\dfrac{\mu_l c_{pl}}{k_l}\right]^{1+y}$

For most fluids the recommended values of the exponents were: x=0.33, y=0.7.

This correlation then corresponds to:

$\dot{q} = $ [constant depending upon fluid properties and surface] $\times \Delta T^3$

The value of the constant C_{sf} depends upon the fluid and the surface and typical values range between 0.0025 and 0.015. Since, for a given value of ΔT_{sat} the heat flux is proportional to C_{sf}^3 the correlation is very sensitive to selection of the correct value.

It is arguable that the complexity of the correlation is not warranted because of the need for this factor.

Some values of C_{sf} for use in Eq. (2.77) are given in Table 2.4.

Table 2.4: Values of C_{sf} for Use in Eq. (2.77) [34]

Fluid	Surface	C_{sf}
Water	Nickel	0.006
Water	Platinum	0.013
Water	Copper	0.013
Water	Brass	0.006
Carbon tetrachloride	Copper	0.013
Benzene	Chromium	0.010
n-Pentane	Chromium	0.015
Ethanol	Chromium	0.0027
Isopropanol	Copper	0.0025
n-Butanol	Copper	0.0030

Mostinski [35]

(2.78) $\alpha = 0.106 P_{cr}^{0.69}(1.8 P_r^{0.17} + 4 P_r^{1.2} + 10 P_r^{10})\dot{q}^{0.7}$

Cooper [36]

(2.79a) $\alpha = 55 P_r^{(0.12 - 0.2 \log \varepsilon)}(-\log P_r)^{-0.55} M^{-0.5}\dot{q}^{0.67}$

where ε is the surface roughness in microns. Typically a value of 1 may be used, thus simplifying the equation.

(2.79b) $\alpha = 55 P_r^{0.12}(-\log P_r)^{-0.55} M^{-0.5}\dot{q}^{0.67}$

P_r in Eqs (2.78), (2.79a) and (2.79b) is the reduced pressure, defined as P/P_{cr}, and P_{cr} is the critical pressure of the fluid.

Mostinski and Cooper are both dimensional equations; therefore, the units must be consistent with the constants given. For the forms quoted here pressures are in bar and heat flux in W/m^2, giving heat transfer coefficients in W/m^2 K.

Comprehensive references on liquid metal boiling are Subbotin [37] and Dwyer [38].

Burnout correlations

As for nucleate boiling the critical peak flux or boiling crisis flux is also very dependent on surface conditions. For water at atmospheric pressure the peak flux lies in the range 130–950 kW/m^2 and this is between 3 and 8 times the value obtained for organic liquids. The corresponding temperature difference for both water and organics is between 20°C and 50°C. Liquid metals have the advantage of low viscosity and high thermal conductivity and the alkali metals in the pressure range 0.1–10 bar give peak flux values of 100–300 kW/m^2 with a corresponding temperature difference of around 5°C.

A number of authors have provided relationships to enable the critical heat flux $\dot{q}_{cr}$ to be predicted. One of these was developed by Rohsenow and Griffith [39] who obtained the following expression:

(2.80) $\dot{q}_{cr} = 0.012 L \rho_v \left[\dfrac{\rho_l - \rho_v}{\rho_v} \right]^{0.6}$

Another correlation due to Caswell and Balzhieser [40] applies to both metals and non-metals.

(2.81) $\dot{q}_{cr} = 1.02 \times 10^{-6} \dfrac{L^2 \rho_v k_l}{c_p^2} \left[\dfrac{\rho_l - \rho_v}{\rho_v} \right]^{0.65} Pr^{0.71}$

2.3.7.4 Boiling from Wicked Surfaces

There is a considerable literature on boiling from wicked surfaces. The work reported includes measurements on plane surfaces and on tubes, the heated surfaces can be horizontal or vertical, and either totally immersed in the liquid or evaporating in the heat pipe mode. Water, organics and liquid metals have all been investigated. The effect of the wick is to further complicate the boiling process since in addition to the factors referred to in the section on boiling from smooth surfaces the wick provides sites for additional nucleation and significantly modifies the movement of the liquid and vapour phases to and from the heated surface.

At low values of heat flux the heat transfer is primarily by conduction through the flooded wick. This is demonstrated in the results of Philips and Hinderman [41] who carried out experiments using a wick of 220.5 nickel foam 0.14 cm thick and one layer of stainless steel screen attached to a horizontal plate. Distilled water was used as the working fluid. Their results are shown in Fig. 2.25. The solid curve is the theoretical curve for conduction through a layer of water of the wick thickness.
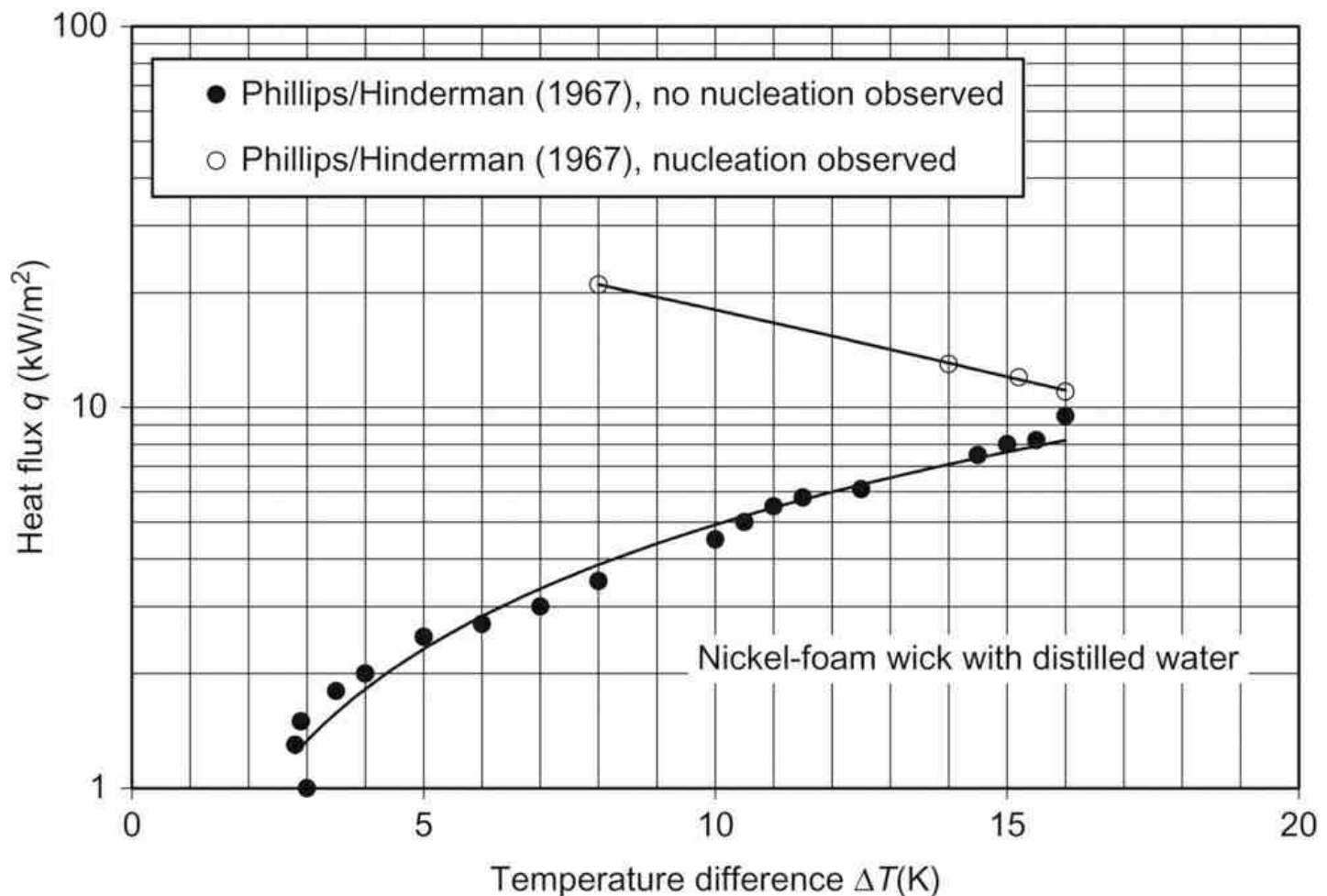
Figure 2.25: Heat transfer from a submerged wick data from Ref. [41]

At higher values of heat flux nucleation occurs. Ferrell and Alleavitch [42] studied the heat transfer from a horizontal surface covered with beds of Monel beads. Results are reported on 30–40 mesh and 40–50 mesh using water at atmospheric pressure as the working fluid and a total immersion to a depth of 7.5 cm. The bed depth ranged from 3 mm to 25 mm. They concluded that the heat transfer mechanism was conduction through a saturated wick liquid matrix to a vapour interface located in the first layer of beads. Agreement was good between the theoretical predictions of this model and the experimental results. No boiling was observed. Figure 2.26 shows these results together with the experimental values obtained for the smooth horizontal

surface. It is seen that the latter agrees well with the Rohsenow correlation but that for low values of temperature difference the heat flux for the wicked surface is much greater than for the smooth surface. This effect has been observed by other workers, for example Corman and Welmet [43]; the curves cross over at higher values of heat flux, probably because of increased difficulty experienced by the vapour in leaving the surface.
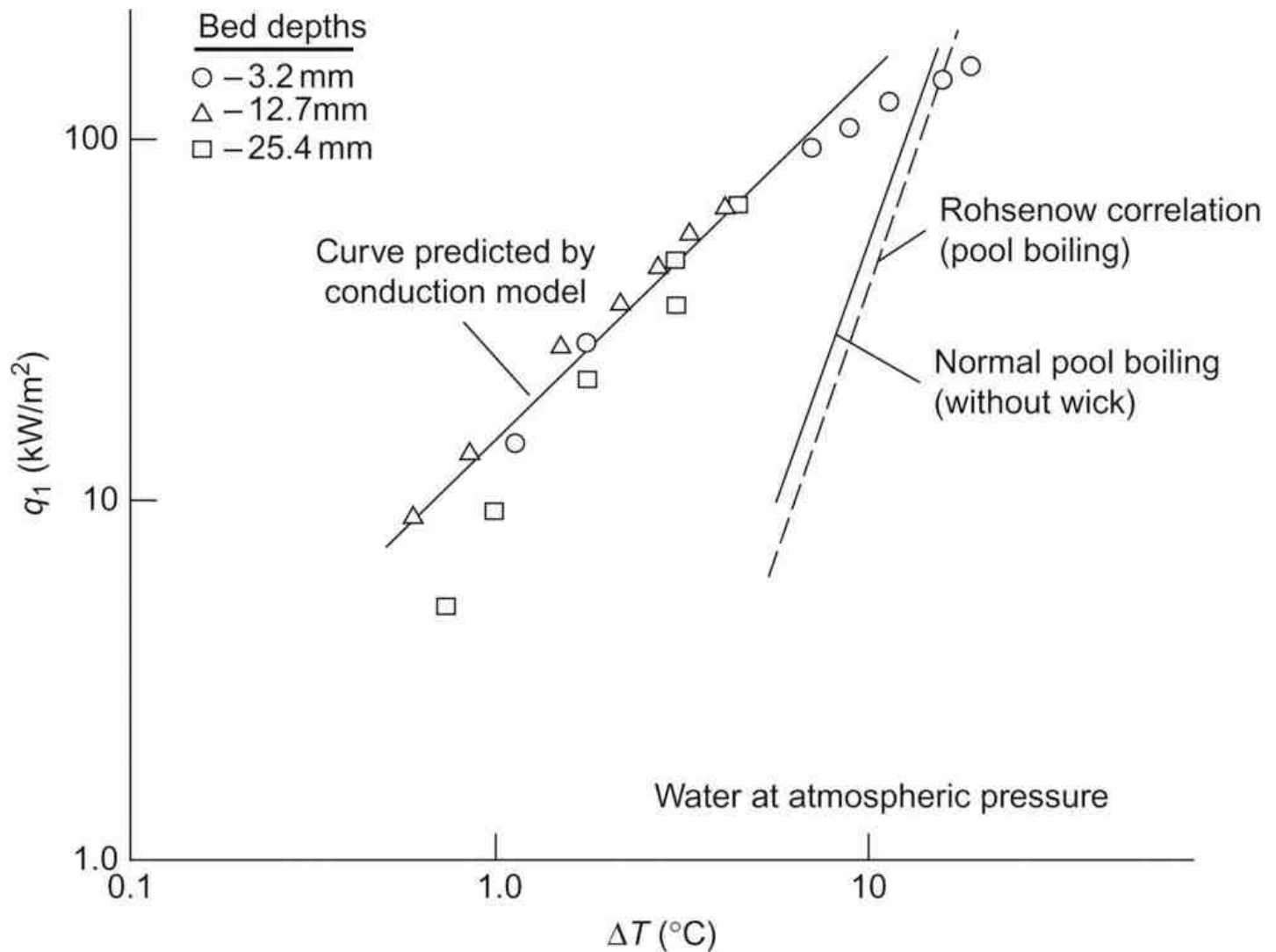
Figure 2.26: Evaporation from a submerged wick compared with boiling from a smooth surface [42]

This concept has been developed further by Brautsch and Kew [44], who examined boiling from a bare surface and the surface covered with mesh wicks. Samples of these results are shown in Fig. 2.27.
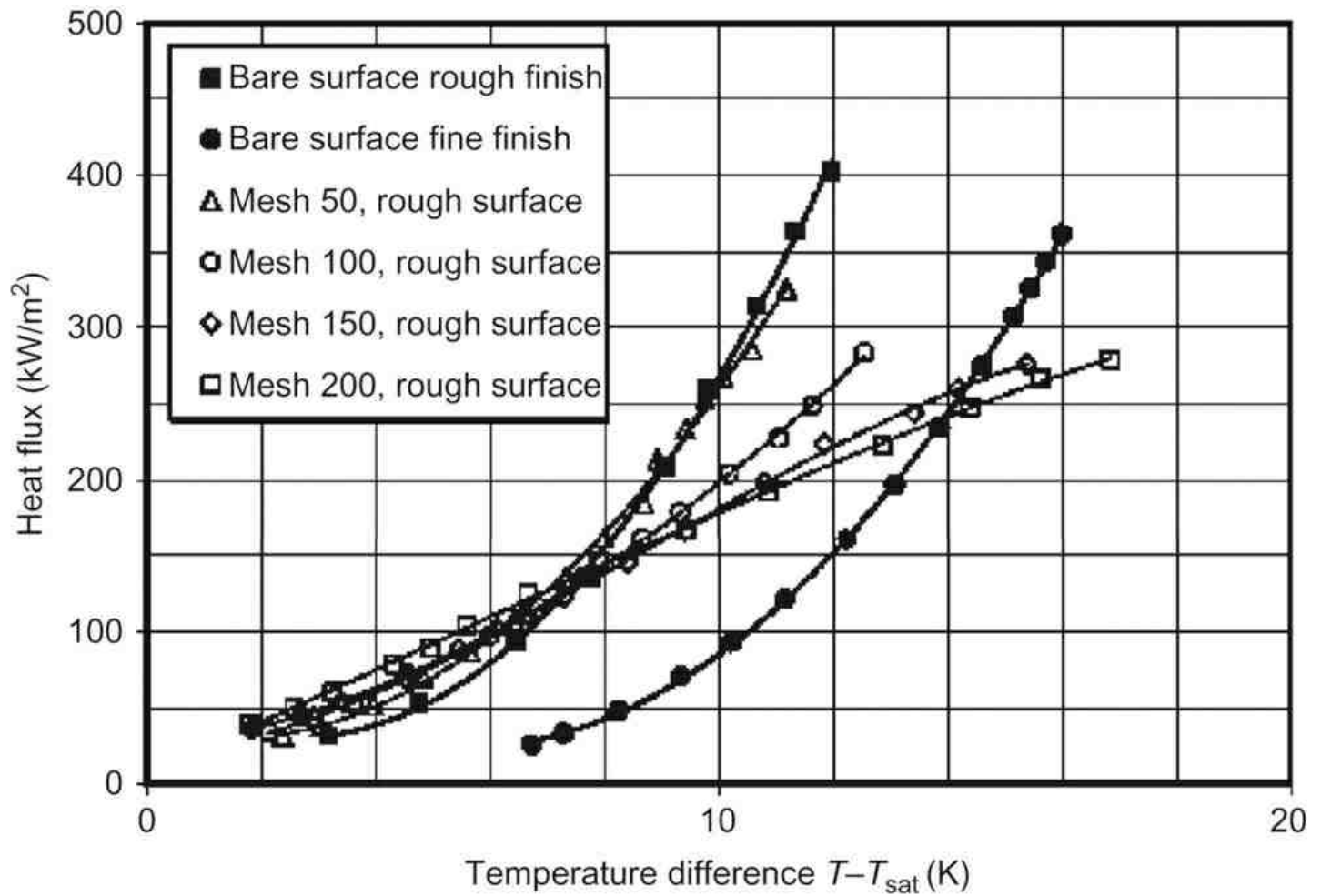
Figure 2.27: Effects of surface finish and mesh on heat transfer [44]

Brautsch [44–46] correlated the heat transfer from the mesh-covered surface by comparing it with a reference heat transfer coefficient obtained for boiling of water and R141b from a smooth plate. Having observed the boiling process using high-speed video it was noted that the mesh acted to enhance nucleation due to the provision of additional nucleation sites, but the presence of the mesh impeded departure of bubbles from the surface. This yielded an equation of the form:

(2.82) $$\frac{\alpha}{\alpha_0} = E(1 - B)$$

where E and B were defined as enhancement and blocking factors respectively and correlated by:

(2.83) $$E = \left[1 + \left(\frac{d_b}{d_{m,i}}\right)^m \left(\frac{R_a}{R_{a_0}}\right)^n \frac{q_0}{q}\right]^r$$

and

(2.84) $$B = \left(\frac{d_b}{d_{m,i}}\right)^u \left(\frac{R_a}{R_{a_0}}\right)^v K^{-1}\left(\left(\frac{q}{q_0}\right)^2 + \frac{q}{q_0}\right)$$

with

(2.85) $$d_b = 0.851 \beta_0 \sqrt{\frac{2\sigma}{g(\rho_1 - \rho_v)}}$$

where β_0 is the contact angle (radians), and the exponents m, n, r, u, v and the fitting factor K are summarised in Table 2.5.

Table 2.5: Relevant
Material Parameters,
Exponents and the Fitting
Factor Used in the
Equations

	All Surface Finishes
m	1
n	0.69
r	1.8
u	1.2
v	0.12
K	2.0E+07

The Cooper correlation (Eq. (2.79)) was found to predict the reference heat transfer coefficient, α_0, well (Fig. 2.28).
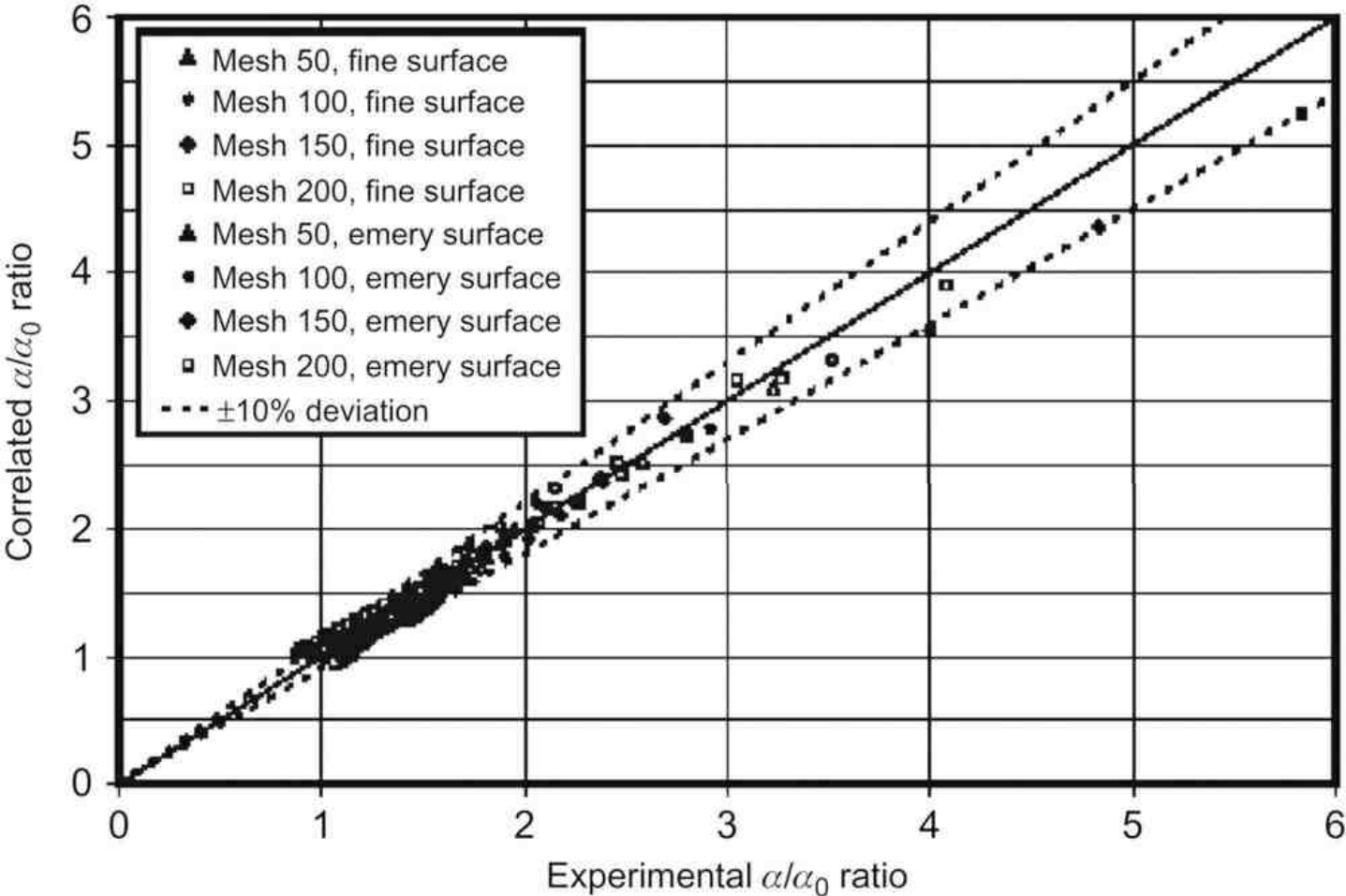
Figure 2.28: Comparison between correlated and experimental heat transfer coefficient ratio for different mesh sizes on different heater surface roughnesses [44]

This correlation showed good agreement with experimental data from Asakavicius et al. [47] who tested multiple brass and stainless steel screen layers in Freon-113, ethyl alcohol and water; Liu et al. [48], who published experimental results for a single layer of mesh 16 and mesh 50, both for the working fluids methanol and HFE-7100; and the results of Tsay et al. [49], single layers of mesh 24 and mesh 50 with distilled water as the working fluid.

Several researchers have worked on evaporation from wicks and selected results are summarised in Fig. 2.29. Abhat and Seban [50] reported on heat transfer measurements on vertical tubes using water, ethanol and acetone as the working fluids. In this series of experiments results were given for smooth surfaces, immersed wicks and evaporating wicks. The authors concluded that up to heat fluxes of 15 W/cm^2 the heat transfer coefficient for a screen or felt wicked tube was similar to that of the bare tube and also not very different from that for the evaporating surface.
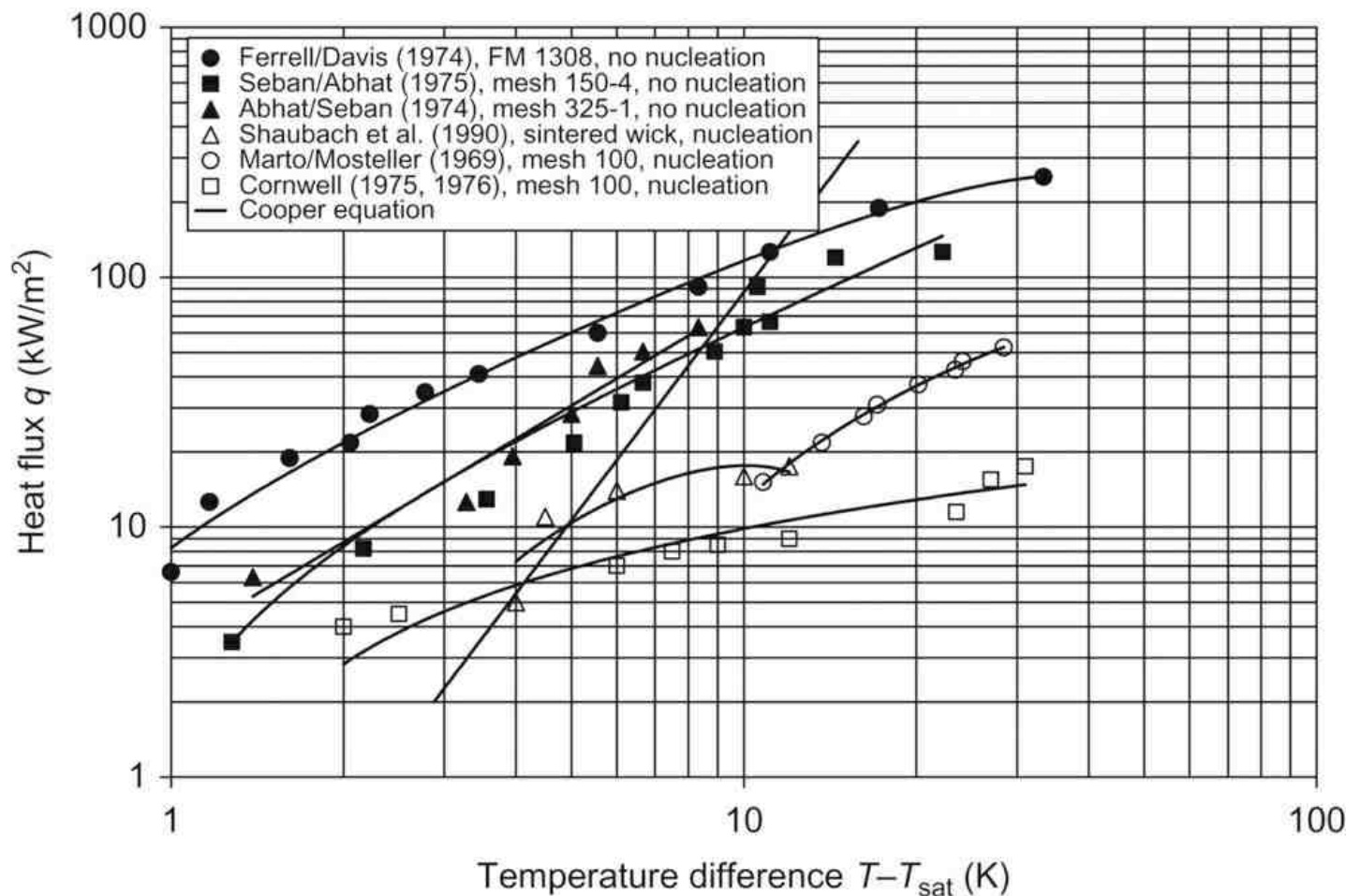
(Data from Refs [50–55]).

Figure 2.29: Results from researchers measuring boiling and convection in the wick material, working fluid distilled water [45]

Marto and Mosteller [51] used a horizontal tube surrounded by four layers of 100 mesh stainless steel screen and water as the working fluid. The outer container was of glass so it was possible to observe the evaporating wick surface. They measured the superheat as a function of heat flux. They found that the critical radius was 0.013 mm compared to the effective capillary radius of 0.6 mm.

There is some evidence that the critical heat flux for wicked surfaces may be greater than that for smooth surfaces; for example, a report by Costello and Frea [56] suggests that the critical heat flux could be increased by about 20% over that for a smooth tube.

Reiss and Schreitzman [57] report very high values of critical heat flux for sodium in grooved heat pipes. They report values from 2 to 10 times the critical values reported by Balzieser [58] in the temperature region around 550°C. The authors observed the grooves as dark stripes on the outer side of the heat pipe and concluded that evaporation was from the grooves only. Their results are plotted in Fig. 2.30 and the heat flux is calculated on the assumption that evaporation is from the groove only. Moss and Kelley [59] constructed a planar evaporator using a stainless steel wick 1/4 inch thick and water as the working fluid. The authors employed a neutron radiographic technique to measure the water thickness. In order to explain their results they proposed two models; in the first it was assumed that vaporisation occurs at the liquid–vapour interface, and in the second model a vapour blanket was assumed to occur at the base of the wick.
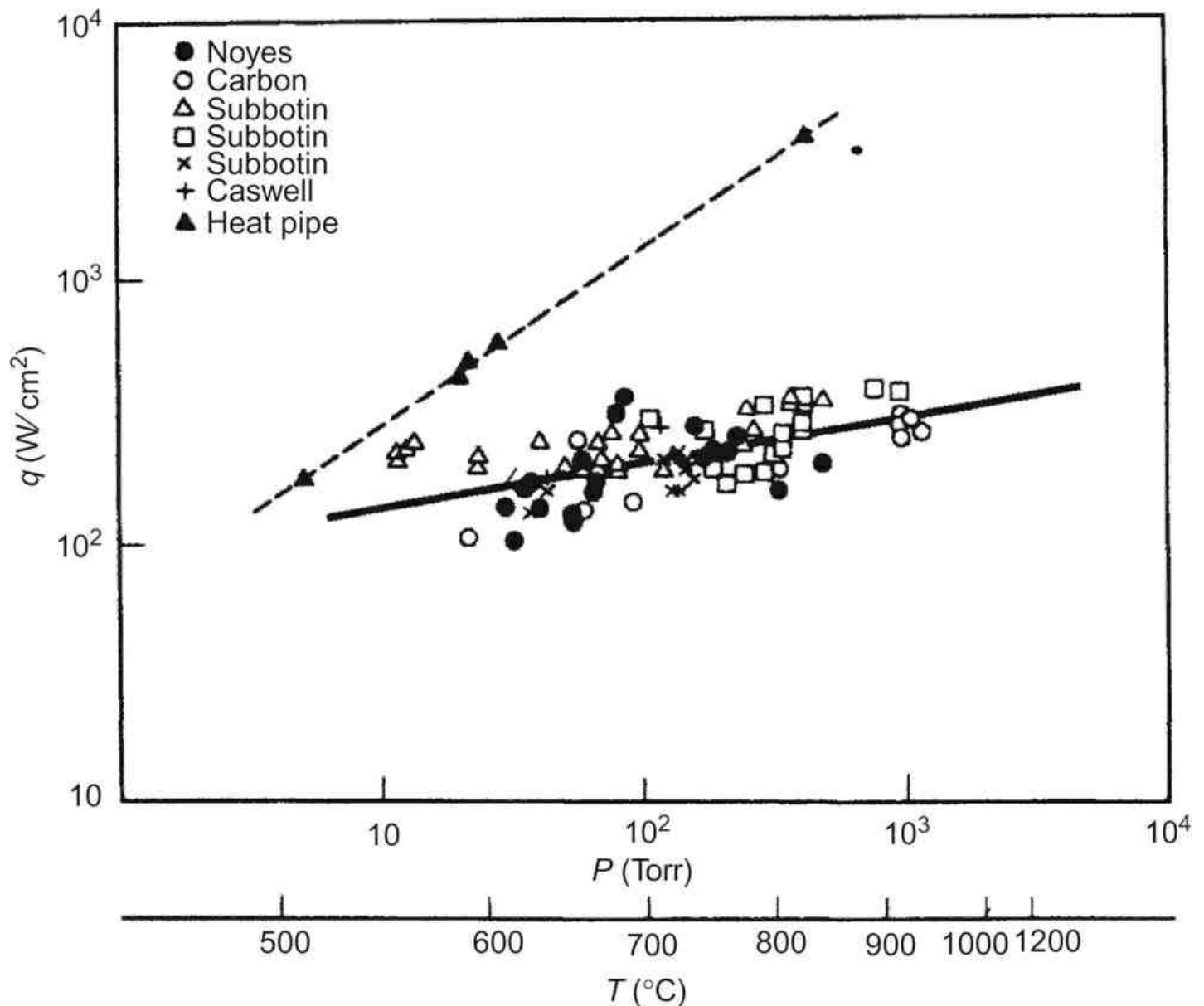
Figure 2.30: Critical flux for sodium pool boiling compared to critical flux in grooved sodium heat pipes [57]

Both the Moss and Kelley models can be used to explain most of the published data. These models are discussed in a paper by Ferrell et al. [52] who describe experiments aimed at differentiating between them. The two models are described by the authors as follows:

1. A layer of liquid-filled wick adjacent to the heated surface with conduction across this layer and liquid vaporisation at the edge of the layer. In this model liquid must be drawn into the surface adjacent by capillary forces.

2. A thin layer of vapour-filled wick adjacent to the heated surface with conduction across this layer to the saturated liquid within the wick. In this model the liquid is vaporised at the edge of this layer and the resulting vapour finds its way out of the wick along the surface and through large pore size passages in the wick. This model is analogous to conventional film boiling.
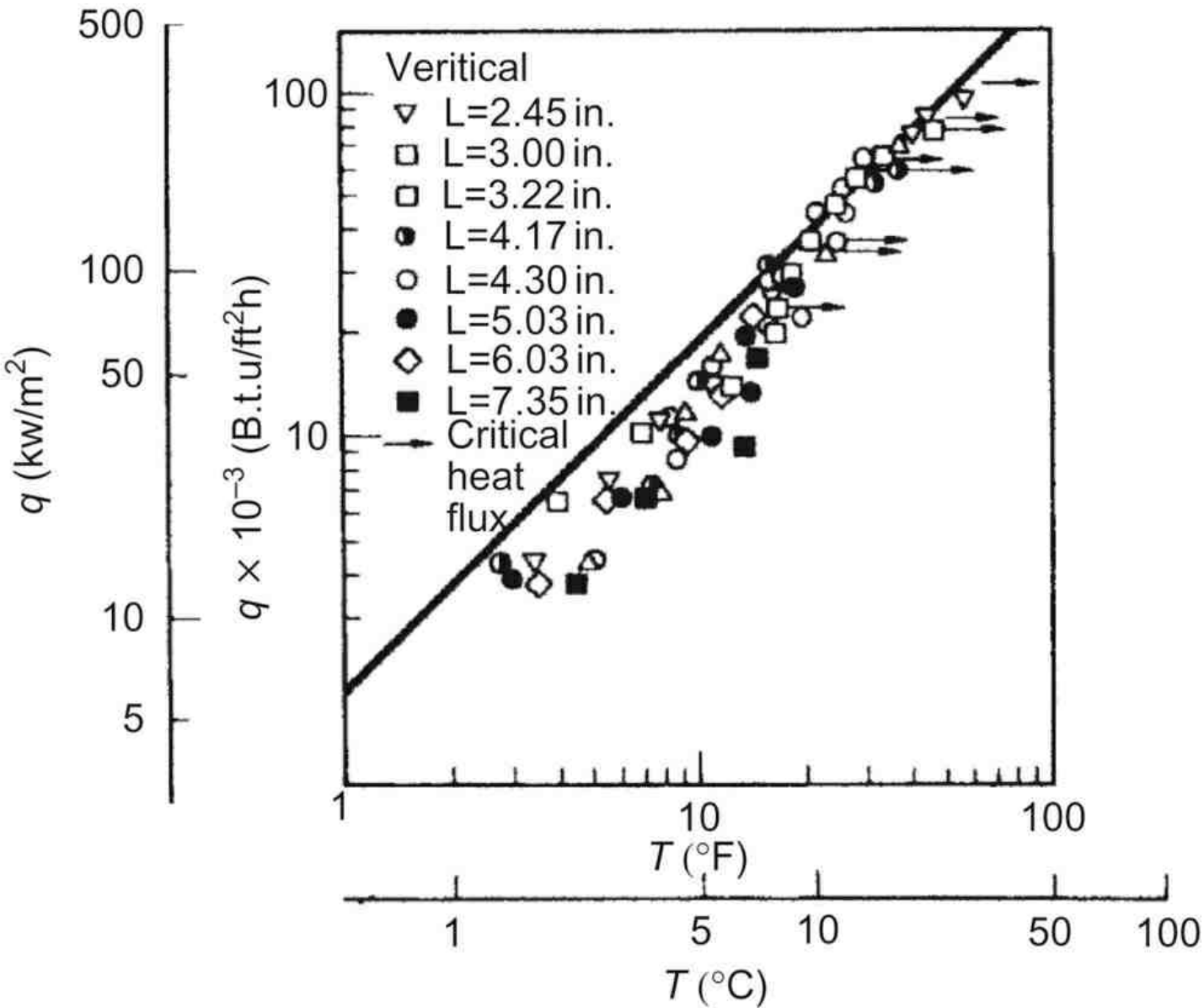
Figure 2.31: Potassium boiling from vertical wick FM1308 [60] (*L* is vertical height above pool)
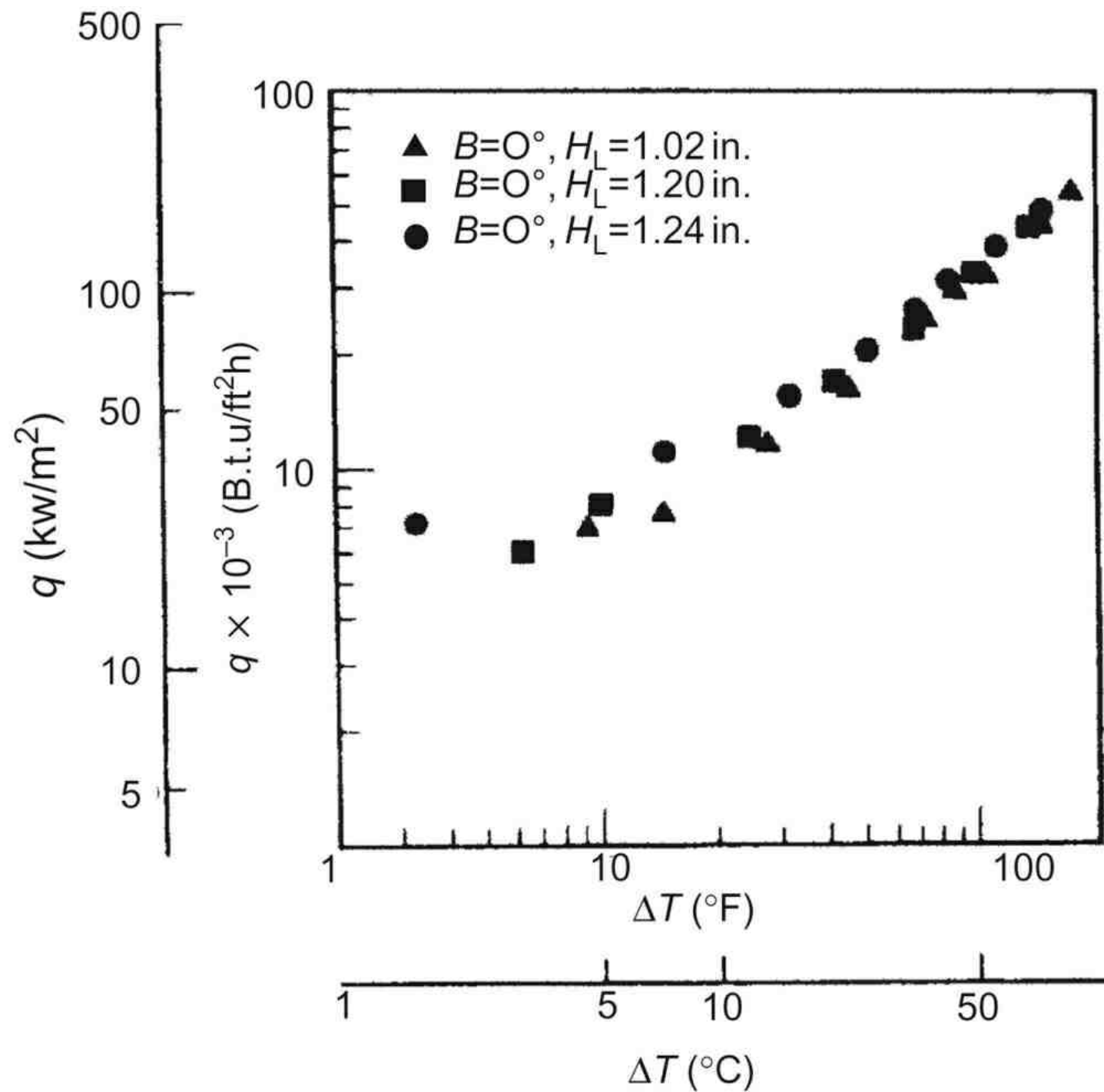
Figure 2.32: Potassium boiling from horizontal wick FM1308 [60]

Experiments were carried out using a stainless steel felt wick FM1308 and both water and potassium as the working fluids. Though the results were not entirely conclusive the authors believed that the second model is the most likely mechanism. Davis and Ferrell [60] report further work using potassium as the working fluid and both a stainless steel felt wick FM1308 and a steel sintered powder wick Lamipore 7.4. The properties of these wicks are given in Table 2.6.

<p style="text-align:center">Table 2.6: Dimensions and Properties of Wick Materials</p>

Material	Thickness (m)	Porosity	Permeability (m²×l0¹⁰)	Capillary Rise (m)
FM1308	3.2×10^{-3}	0.58	0.55	0.26
Lamipore 7.4	1.5×10^{-3}	0.61	0.48	0.35

The data for the vertical heat pipe were different from the heat pipe in the horizontal positions for both types of wick. Figures 2.31 and 2.32 give the results for the FM1308 wick in the vertical and horizontal positions. For the vertical position the heat transfer coefficient for FM1308 increased with increasing flux becoming constant at a value 10.2 kW/m² K. For Lamipore 7.4

the coefficient decreases with increasing heat flux from 18.2 kW/m^2 K to 14.8 kW/m^2 K.

The effective thermal conductivities of the two wick structures have been calculated using the parallel model (Eq. (2.91)) and the series model (Eq. (2.92)). These results are given in Table 2.7 together with the experimentally measured heat transfer coefficients.

Table 2.7: Heat Transfer Coefficients for Potassium in Vertical Heat Pipe (α in kW/m^2 K)

Wick	Parallel Model, k_w	Series Model, k_w	Experimental Result, α
FM1308	9.6	8.5	10.2
Lamipore 7.4	19	18	18.2–14.8

The agreement between the limits of the two models and the measured value for FM1309 is close. The agreement for Lamipore is good at low heat fluxes and there was evidence for the development of a poor thermal contact during the experiment, which may explain the discrepancy at high flux values.

The heat transfer coefficients for the heat pipe in the horizontal position were much lower than for the vertical case (1.1–5 kW/m^2 K) and similar to results obtained for a bare horizontal surface with no boiling. It is suggested that in the horizontal case further temperature drop occurs by conduction through an excess liquid layer above the wick surface (this would not arise in normal heat pipe operation).

In the case of water the heat transfer coefficient is 11.3 kW/m^2 K for both the vertical and horizontal cases, as shown in Fig. 2.33. The authors conclude that the heat transfer mechanism is different for liquid metals from the mechanism which applies to water and other non-metallic fluids. In the case of non-metallic fluids they suggest that the vaporisation process occurs within the porous media. This vaporisation is probably initiated by inert gas trapped in the porous media or nucleation on active sites on the heated surface. Once initiated the vapour phase spreads out to form a stable layer. The data for water shows that high fluxes are drawn for quite low values of temperature difference, whereas much larger values of temperature difference might be expected if the mechanism is one of conventional film boiling. The mechanism may be of nucleate boiling at activation sites on the heating surface and wick adjacent to it. This was confirmed by the observations of Brausch [45].
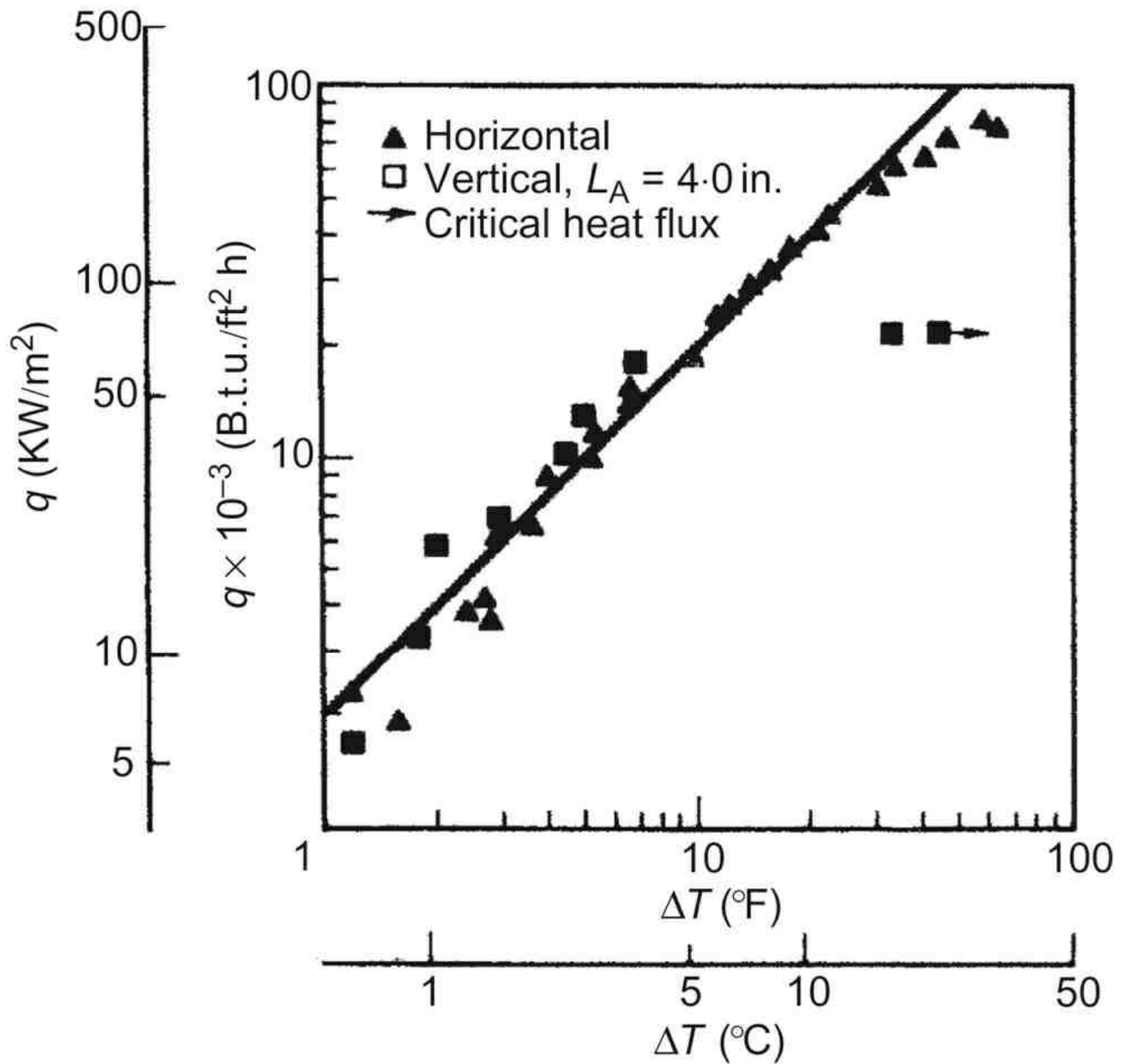
(Data for vertical and horizontal wick is taken from Ref. [58]).

Figure 2.33: Water boiling from FM1308 wick

It is difficult to initiate bubbles in liquid metals and the experimental results of Ref. [45] strongly suggested that for these fluids the wick is saturated and that vaporisation occurs at the liquid surface on the outside of the wick. Hence for liquid metals the heat transfer coefficient can be accurately predicted by considering conduction through the wick using Eqs (2.91) and (2.92).

One limit to the radial heat transfer to the evaporating fluid will be set by the 'wicking', that is when the capillary forces are unable to feed sufficient liquid to the evaporator.

The limiting heat flux $\dot{q}_{crit}$ will be given by the expression:

$$\dot{q}_{crit} = \frac{\dot{m}L}{\text{area of evaporator}}$$

where the mass flow in the wick is related to the pressure head, ΔP, by an expression such as Eq. (2.32).

Ferrel et al. [61] have derived a relationship for a planar surface with a homogeneous wick.

$$(2.86) \quad \dot{q}_{crit} = \frac{g(h_{co}\rho_l(\sigma_l/\sigma_{lo}) - \rho_l l \sin \phi)}{(l_e \mu_l/L\rho_l kd)[(l_e/2) + l_a]}$$

where

- h_{co} is the capillary height of the fluid in the wick measured at a reference temperature;

- σ_{lo}, ρ_{lo} are the fluid surface tension and density measured at the same reference temperature;

- σ_l, ρ_l, μ_l are the fluid surface tension, density and viscosity measured at the operating temperature.

All other symbols have their usual significance. Ferrell and Davis [52] extended their equation by including a correction for thermal expansion of the wick.

$$(2.87) \quad \dot{q}_{crit} = \frac{g(h_{co}\rho_l(\sigma_l/\sigma_{lo}) - \rho_l l \sin \phi (1 + \alpha_t \Delta T))}{(l_e \mu_l/L\rho_l kd(1 + \alpha_t \Delta T))[(l_e/2) + l_a]}$$

where α_t is the coefficient of linear expansion of the wick and ΔT the difference between the operating and reference temperature.

Figure 2.34 shows a comparison of measured values of $\dot{q}_{crit}$ against predicted values from Eq. (2.87) for both water and potassium. The equation successfully predicts heat flux limits for potassium up to a value of 315 kW/m^2. It is also in good agreement for water up to 130 kW/m^2. Above this value the experimental values fall below the values predicted by Eq. (2.87) showing that another mechanism is limiting the flux. The limiting factor is probably due to difficulty experienced by water vapour in leaving the heat surface through the wick. The reduction in heat flux below the predicted value for water further supports the view that for non-metallic fluids vaporisation occurs within the wick. More recent work on radial heat flux measurements and observation of vapour/liquid proportions and nucleation within wicks has resulted in more data showing that nucleation is not detrimental to heat pipe performance.
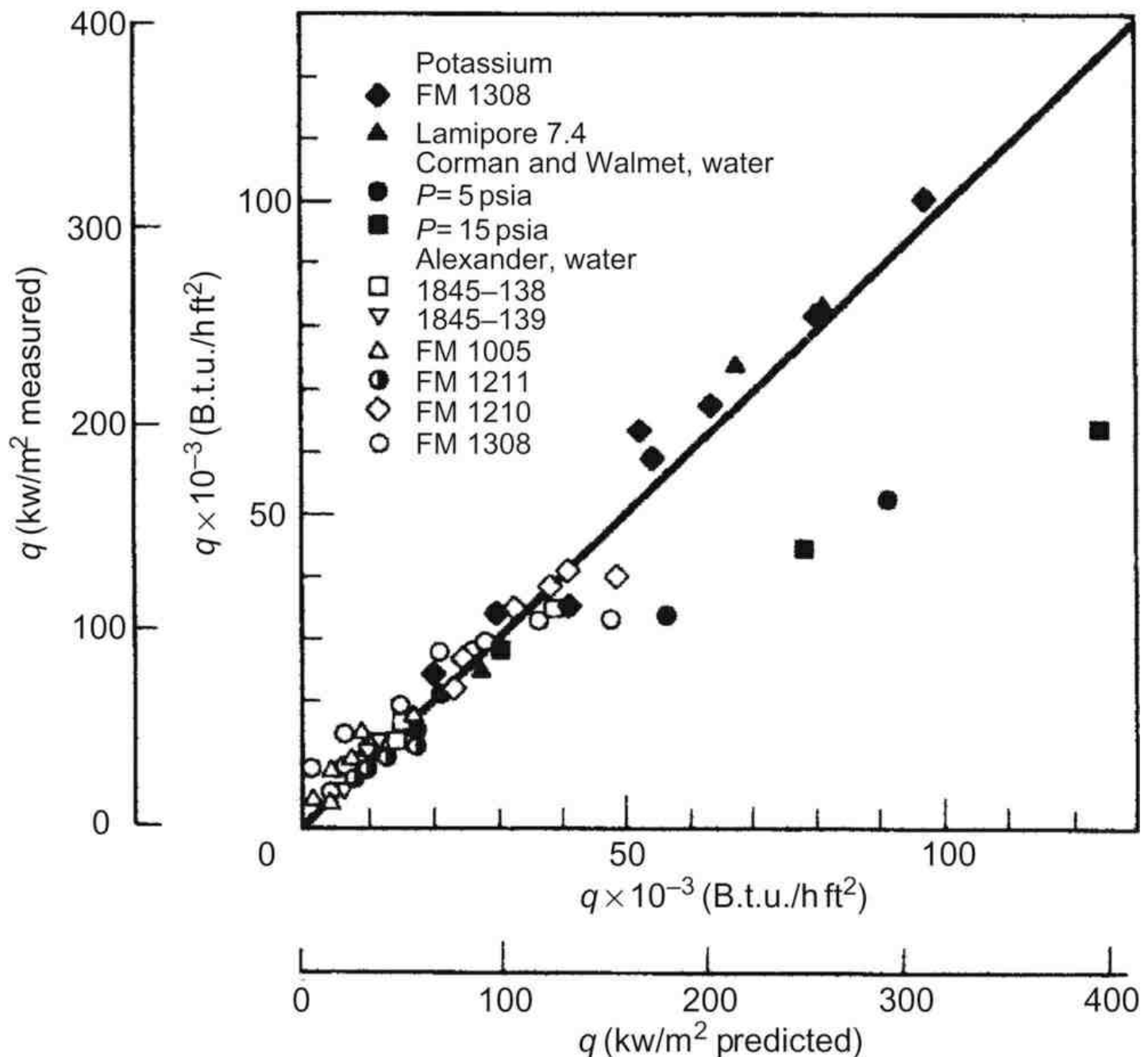
Figure 2.34: Comparison of measured and predicted burnout for water and potassium [60]

2.3.7.5 Liquid–Vapour Interface Temperature Drop

Consider a liquid surface; there will be a continuous flux of molecules leaving the surface by evaporation. If the liquid is in equilibrium with the vapour above its surface an equal flux of molecules will return to the liquid from the vapour and there will be no net loss or gain of mass. However, when a surface is losing mass by evaporation clearly the vapour pressure and hence temperature of the vapour above the surface must be less than the equilibrium value. In the same way, for net condensation to occur the vapour pressure and temperature must be higher than the equilibrium value.

The magnitude of the temperature drop can be estimated as follows.

First consider the vapour near the interface. The average velocity V_{av} in a vapour at temperature T_V and having molecular mass M is given by kinetic theory as:

(2.88) $$V_{av} = \sqrt{\frac{8 k_B T_v}{\pi M}}$$

where k_B is Boltzmann constant.

The average flow of molecules in any given direction is:

$$\frac{nV_{av}}{4} / \text{unit area}$$

and the corresponding flow of heat per unit area is:

$$\frac{MLnV_{av}}{4}$$

where n is the number of molecules per unit volume and L is the latent heat.

For a perfect gas

$$P_v = nk_B T_v$$

hence the heat flux to the liquid surface from the $\text{vapour} = P_v L \sqrt{(M/2\pi kT_v)}$

The heat flux away from the liquid surface is given by $P_l L \sqrt{(M/2\pi kT_l)}$.

Setting $T_v = T_l = T_s$ allows evaluation of the net heat flux across the surface:

$$(2.89) \qquad \dot{q} = (P_l - P_v)L \sqrt{\frac{M}{2\pi k_B T_s}}$$
$$= \frac{(P_l - P_v)L}{\sqrt{2\pi RT}}$$

By using the Clapeyron equation,

$$\frac{dP}{dT} = \frac{L}{(v_v - v_l)T_{sat}}$$

and assuming that the vapour behaves as a perfect gas and the liquid volume is negligible:

$$\frac{\Delta P}{\Delta T} = \frac{PL}{RT^2}$$

Eq. (2.90) may be written as:

$$(2.90) \qquad \dot{q} = \frac{\Delta T L^2 P}{(2\pi RT_s)^{0.5}} \frac{1}{RT_s^2}$$

thus permitting calculation of the interfacial temperature change in the evaporator and condenser.

Values of $(\dot{q}/P_l - P_v)$ for liquids near their normal boiling points are given in Table 2.8.

Table 2.8: Interfacial Heat Flux as a Function of Pressure Difference [62]

Fluid	T_b (K)	$\dot{q}/P_l - P_v$ (kW/cm^2 atm)
Lithium	1613	55
Zinc	1180	18
Sodium	1156	39
Water	373	21.5
Ethanol	351	13.5
Ammonia	238	15.2

2.3.7.6 Wick Thermal Conductivity

The effective conductivity of the wick saturated with the working fluid is required for calculating the thermal resistance of the wick at the condenser region and also, under conditions of evaporation when the evaporation is from the surface for the evaporator region. Two models are used in the literature (see also Chapter 3).

  i. *Parallel case*. Here it is assumed that the wick and working fluid are effectively in parallel.

If K_l is the thermal conductivity of the working fluid and k_s is the thermal conductivity of the wick material and:

$$\varepsilon = \text{Voidage fraction} = \frac{\text{Volume of working fluid in wick}}{\text{Total volume of wick}}$$

(2.91) $k_w = (1-\varepsilon)k_s + \varepsilon k_l$

ii. *Series case*. If the two materials are assumed to be in series.

(2.92) $k_w = \dfrac{1}{((1-\varepsilon)/k_s) + (\varepsilon/k_l)}$

Additionally, convection currents in the wick will tend to increase the effective thermal conductivity.

2.3.7.7 Heat Transfer in the Condenser

Vapour will condense on the liquid surface in the condenser, the mechanism is similar to that discussed in Section 2.3.7.5 on the mechanism of surface evaporation and there will be a small temperature drop and hence thermal resistance. Further temperature drops will occur in the liquid film and in the saturated wick and in the heat pipe envelope.

Condensation can occur in two forms, either by the condensing vapour forming a continuous liquid surface or by forming a large number of drops. The former, film condensation occurs in most practical applications, including heat pipes and will be discussed here. Condensation is seriously affected by the presence of a non-condensable gas. However, in the heat pipe vapour pumping will cause such gas to be concentrated at the end of the condenser. This part of the condenser will be effectively shut off and this effect is the basis of the gas-buffered heat pipe. The temperature drop through the saturated wick may be treated in the same manner as at the evaporator.

Film condensation may be analysed using Nusselt theory. The first analysis of film condensation was due to Nusselt and given in standard text books, e.g. in Ref. [63]. The theory considers condensation onto a vertical surface and the resulting condensed liquid film flows down the surface under the action of gravity and is assumed to be laminar. Viscous shear between the vapour and liquid phases is neglected. The mass flow increases with distance from the top and the flow profile is shown in Fig. 2.35. The average heat transfer coefficient, *α*, over a distance *x* from the top is given by:

(2.93) $\alpha = 0.943 \left[\dfrac{L\rho_l^2 g k_l^3}{x\mu_l(T_s - T_w)} \right]^{0.25}$
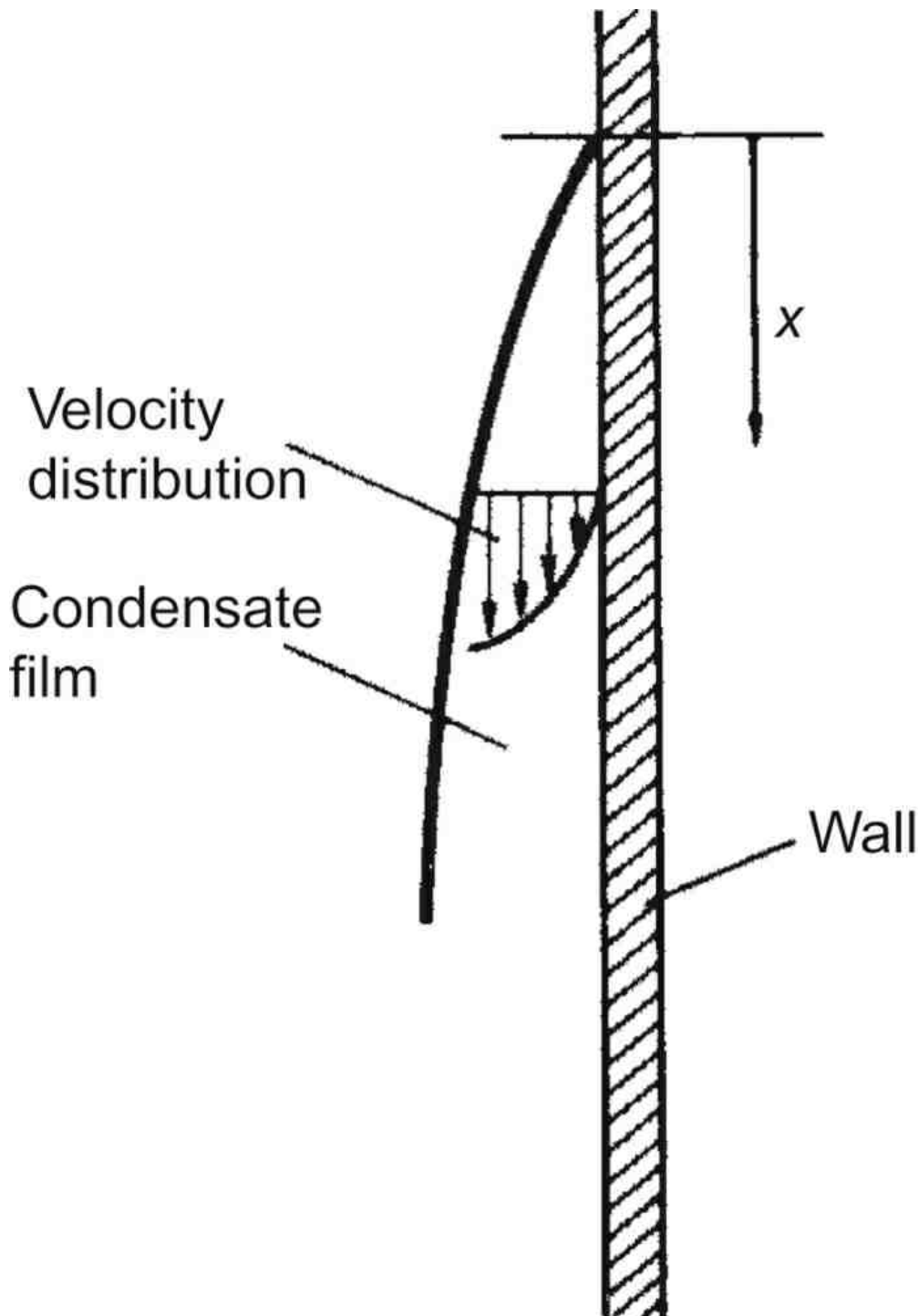
Figure 2.35: Film condensation on a vertical surface

where $(T_s - T_w)$ is the temperature drop across the liquid film.

[2]The Navier–Stokes equation, together with the continuity equation, is a relationship which relates the pressure, viscous and inertial forces in a three-dimensional, time-varying flow. A derivation and statement of the Navier–Stokes equation is given in, for example, Ref. [18].

2.4 APPLICATION OF THEORY TO HEAT PIPES AND THERMOSYPHONS

2.4.1 Wicked Heat Pipes

2.4.1.1 The Merit Number

It will be shown, with reference to the capillary limit, that if vapour pressure loss and gravitational head can be neglected then the properties of the working fluid which determine the maximum heat transport can be combined to form a figure of merit, *M*.

(2.94) $M = \dfrac{\rho_l \sigma_l L}{\mu_l}$

The way in which *M* varies with temperature for a number of working fluids is shown in Fig. 2.36.
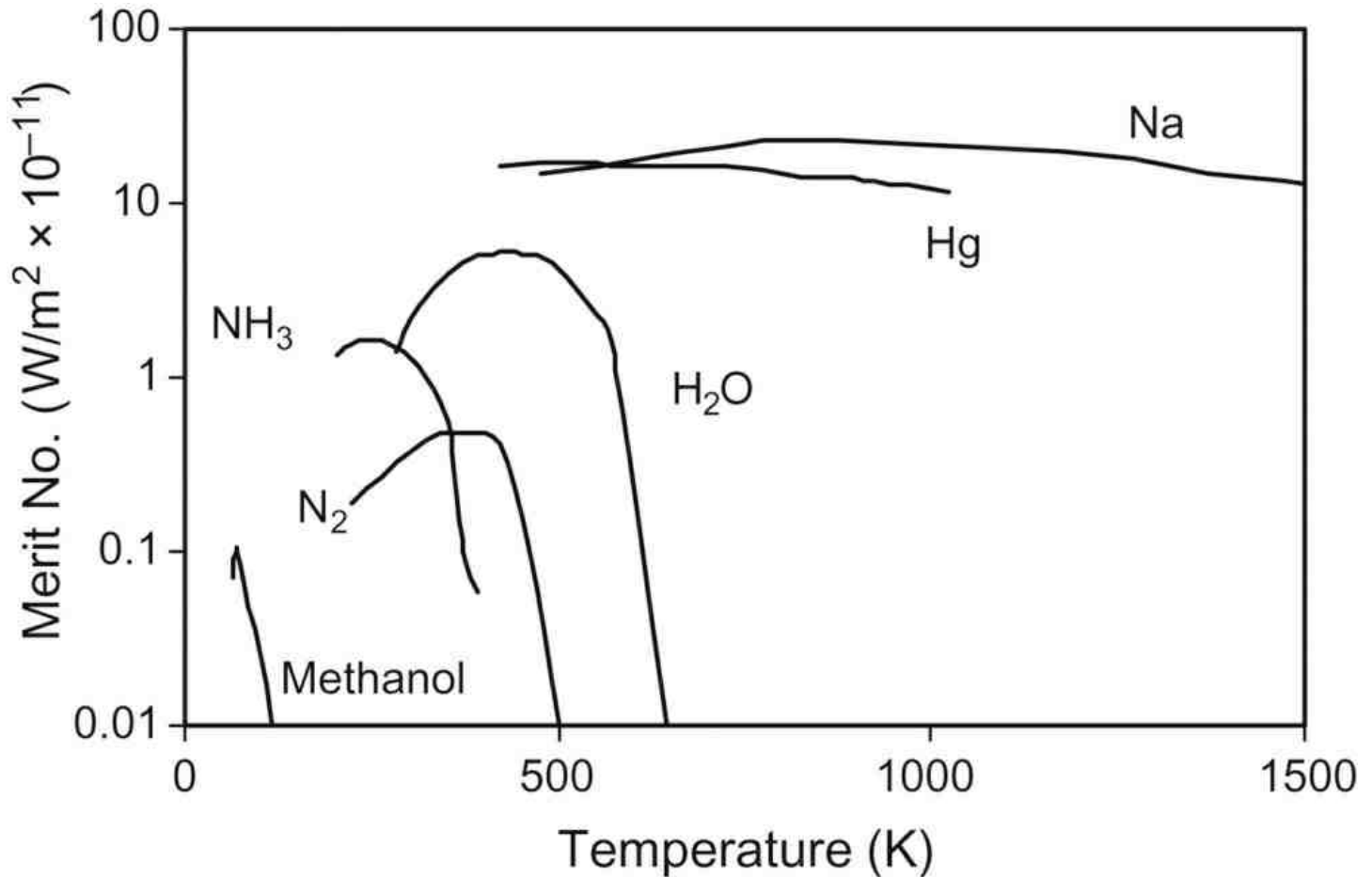
Figure 2.36: Merit number of selected working fluids

2.4.1.2 Operating Limits

Upper limits to the heat transport capability of a heat pipe may be set by one or more factors. These limits were illustrated in Fig. 2.1.

Viscous, or vapour pressure, limit. At low temperature viscous forces are dominant in the vapour flow down the pipe. Busse has shown that the axial heat flux increases as the pressure in the condenser is reduced, the maximum heat flux occurring when the pressure is reduced to zero. Busse carried out a two-dimensional analysis; finding that the radial velocity component had a significant effect, he derived the following equation:

(2.95) $\dot{q} = \dfrac{r_v L \rho_v P_v}{16 \mu_v l_{eff}}$

where P_v and ρ_v refer to the evaporator end of the pipe. This equation agrees well with published data [64]. The vapour pressure limit is described well in the ESDU Data Item on capillary-driven heat pipes [65]. It is stated that when the vapour pressure is very low, the minimum value must occur at the closed end of the condenser section, the vapour pressure drop can be constrained by this very low – effectively zero – pressure, and the low vapour pressure existing at the closed end of the evaporator section. The maximum possible pressure drop is therefore equal to the vapour pressure in the evaporator. Because the vapour pressure difference naturally increases as the heat transported by the heat pipe rises, the constraint on this pressure difference thus necessitates that $\dot{q}$ is limited. The limit is generally only of importance in some units during start-up. A criterion for avoidance of this limit is given in Ref. [65] as:

$$\frac{\Delta P_{\mathrm{v}}}{P_{\mathrm{v}}} < 0.1$$

Sonic limit. At a somewhat higher temperature choking at the evaporator exit may limit the total power handling capability of the pipe. This problem was discussed in Section 2.3.5. The sonic limit is given by:

(2.96) $\dot{q} = 0.474 L(\rho_{\mathrm{v}} P_{\mathrm{V}})^{0.5}$

There is good agreement between this formula and experimental results. Figure 2.37, due to Busse [64], plots the temperature at which the sonic limit is equal to the viscous limit as a function of l_{eff}/d^2 for some alkali metals, where $d = 2r_{\mathrm{V}}$, the vapour space diameter.

Figure 2.37: Transition from viscous to sonic limit

Entrainment limit. This was discussed in Section 2.3.6. Equation (2.65) gave the entrainment limiting flux as:

(2.65) $\dot{q} = \sqrt{\frac{2\pi \rho_{\mathrm{v}} L^2 \sigma_1}{z}}$

Kemmes experiments suggest a rough correlation of this failure mode with the centre-to-centre wire spacing for *z*, and that a very fine screen will suppress entrainment.
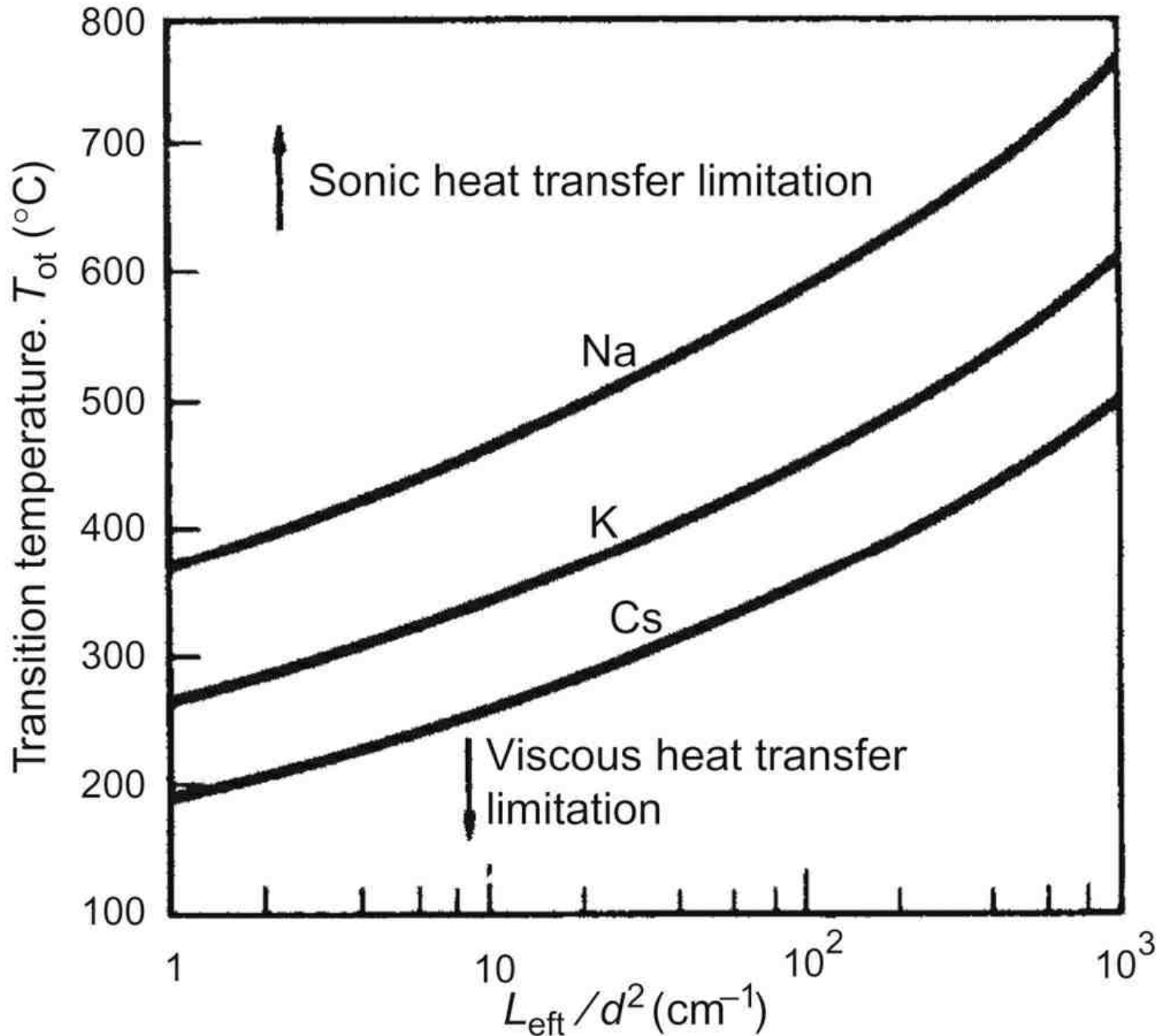
A number of workers have presented data on entrainment limits for specific cases. Tien and Chung [66] present equations which, it is claimed, enable the user to predict the maximum heat transfer rate due to the entrainment limitation. Some experimental data suggest that the equations give accurate results. Data are presented for 'gravity-assisted wickless heat pipes' (thermosyphons), gravity-assisted wicked heat pipes, horizontal heat pipes, grooved heat pipes and rotating heat pipes. Experiments with gravity-assisted heat pipes employing simple wick structures were carried out by Coyne Prenger and Kemme [67] in order to arrive at a correlation which could be used to predict the entrainment limits for all the data investigated.

This work led to the conclusions that the entrainment limits in the cases studied were vapour-dominated and were essentially independent of the fluid inventory. The entrainment limits were successfully correlated with a physical model based on a critical Weber number (see Eq. (2.62)), the expression being:

$$(2.97) \quad \dot{Q} = \sqrt{\frac{2\pi E_t}{\alpha_v} \frac{\delta}{\delta^*}}$$

where E_t is a dimensionless entrainment parameter defined by $(\sigma_l / \rho_l L \delta)$, α_v the velocity profile correction factor, δ the surface depth and δ^* a reference surface depth.

The characteristic length in the Weber number formulation was the depth of the wick structure (an example being cited by the authors as the depth of grooves in a circumferentially grooved wick). In the case of mesh wicks, one half of the wire diameter of the innermost layer is used (this also allows for mesh composite wicks). The limit is also discussed for gravity-assisted heat pipes by Nguyen-chi and Groll where it is also called the flooding limit – as the condenser becomes flooded.

Capillary limit or wicking limit. In order for the heat pipe to operate, Eq. (2.2) must be satisfied, namely

$$(2.2) \quad \Delta P_{c,max} \geq \Delta P_l + \Delta P_v + \Delta P_g$$

Expressions to enable these quantities to be calculated are given in Section 2.3.

An expression for the maximum flow rate m may readily be obtained if we assume that

   i. the liquid properties do not vary along the pipe,

   ii. the wick is uniform along the pipe,

   iii. the pressure drop due to vapour flow can be neglected.

$$(2.98) \quad \dot{m}_{max} = \left[\frac{\rho_l \sigma_l}{\mu_l}\right]\left[\frac{KA}{l}\right]\left[\frac{2}{r_e} - \frac{\rho_l g l}{\sigma_l}\sin\phi\right]$$

and the corresponding heat transport $\dot{Q}_{max} = \dot{m}_{max} L$ is given by:

$$(2.99) \quad \dot{Q}_{max} = \dot{m}_{max}L = \dot{m}_{max} = \left[\frac{\rho_l \sigma_l L}{\mu_l}\right]\left[\frac{KA}{l}\right]\left[\frac{2}{r_e} - \frac{\rho_l g l}{\sigma_l}\sin\phi\right]$$

The group defined in Eq. (2.94) as:

$$\frac{\rho_l \sigma_l L}{\mu_l}$$

depends only on the properties of the working fluid and is known as the figure of merit, or merit number, M, plotted for several fluids on Fig. 2.36.

2.4.1.3 Burnout

Burnout will occur at the evaporator at high radial fluxes. A similar limit on peak radial flux will also occur at the condenser. These limits are discussed in Section 2.3.7. At the evaporator Eq. (2.87) gives a limit which must be satisfied for a homogeneous wick. This equation, which represents a wicking limit, is shown to apply to potassium up to 315 kW/m^2 and probably is applicable at higher values for potassium and other liquid metals. For water and other non-metallics vapour production in the wick becomes important at lower flux densities (130 kW/m^2 for water) and there are no simple correlations. For these fluids experimental data in Table 3.3 should be used as an indication of flux densities which can be achieved. Tien [68] has summarised the problem of nucleation within the wick, and the arguments for possible performance enhancement in the presence of nucleation. Because of phase equilibrium at the interface, liquid within the wick at the evaporator is always superheated to some degree, but it is difficult to specify the degree of superheat needed to initiate bubbles in the wick. While boiling is often taken as a limiting feature in wicks, possibly upsetting the capillary action, Cornwell and Nair [55] found that

nucleation reduces the radial temperature difference and increases heat pipe conductance. One factor in support of this is the increased, thermal conductivity of liquid saturated wicks in the evaporator section, compared with that in the condenser.

Tien believed that the boiling limit will become effective only when the bubbles generated within the wick become trapped there, forming a vapour blanket. This was confirmed by Brautsch [45]. Thus, some enhancement of radial heat transfer coefficient in the evaporator section can be obtained by nucleate boiling effects; however, excessive nucleate boiling disrupts the capillary action and reduces the effective area for liquid flow. It is useful to compare the measurements of radial heat flux as a function of the degree of superheat (in terms of the difference between wall temperature T_w and saturation temperature T_{sat}) for a number of surfaces and wick forms which have been the subject of recent studies. These are shown in Table 2.9. Abhat and Seban [50], in discussing their results as shown in Table 2.9, stated that for every pool depth, there was a departure from the performance recorded involving a slow increase in the evaporator temperature. In order to guarantee indefinite operation of the heat pipe without dry-out, the authors therefore suggested that the operating flux should be considerably less than that shown in Table 2.9. They also found that their measurements of radial flux as a function of $T_w - T_{sat}$ were similar, regardless of whether the surface was flat, contained mesh, or a felt. This is partly borne out by the results of Wiebe and Judd [70], also given in Table 2.9. Costello and Frea, however, dispute this [56] (Fig. 2.38).

Table 2.9: Measured Radial Heat Fluxes in Wicks

Reference	Wick	Working Fluid	Superheat (°C)	Flux (W/cm^2)
Wiebe and Judd [70]	Horizontal flat surface	Water	3	0.4
			6	1.2
			11	8
			17	20
Abhat and Seban [50]	Meshes and felts	Water	5	
			6	5
			11	12
			17	20
Cornwell and Nair [55]	Foam	Water	5	2
			10	10
			20	18
	Mesh (100)	Water	5	7
			10	9
			20	13
Abhat and Nguyen-chi [69]	Mesh*	Water	6	1
			10	8
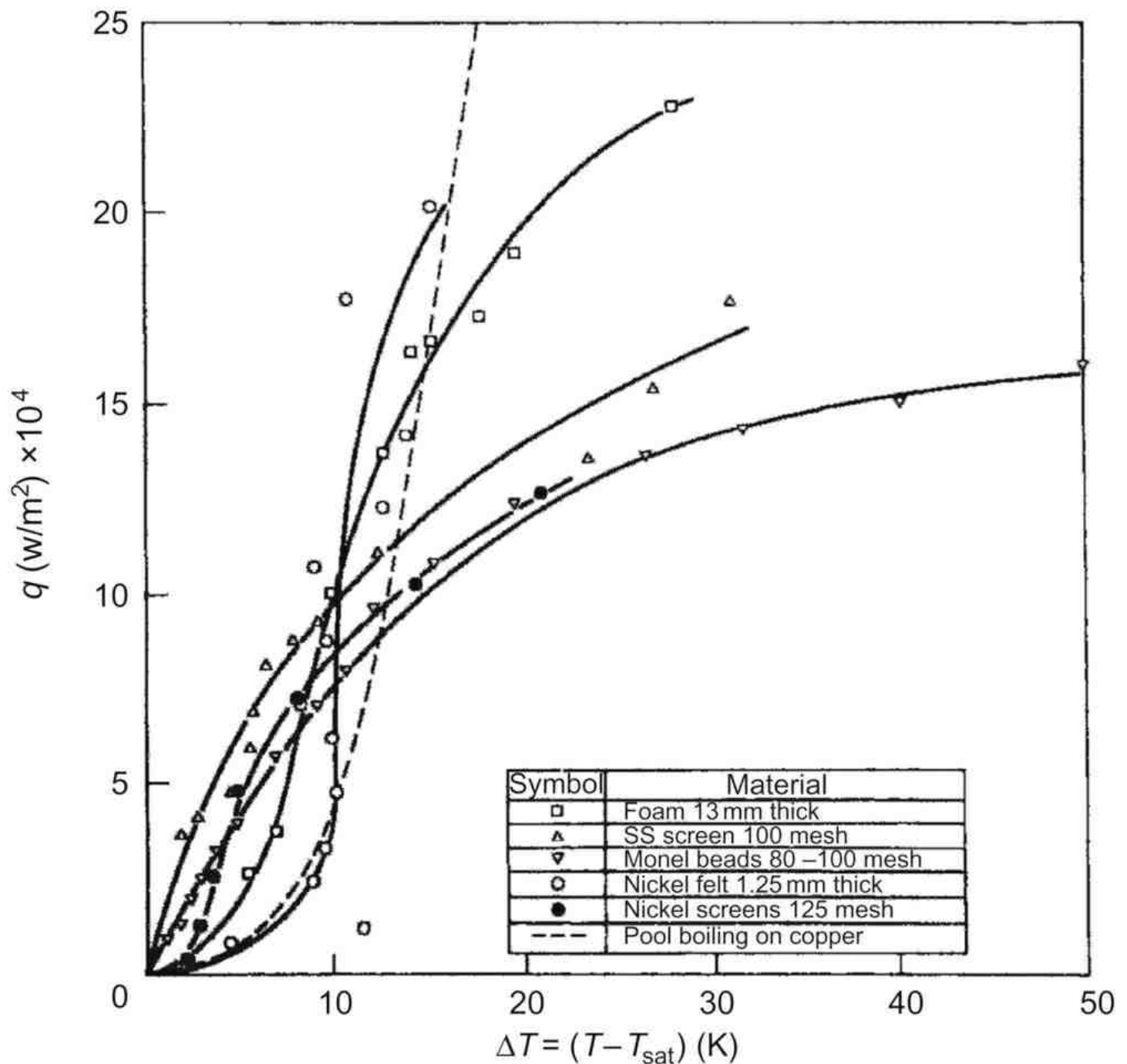
Figure 2.38: Variation of heat flux with superheat for water in porous media [54]

The work of Cornwell and Nair [54] gives results similar to those of Abhat and Seban [50]. Some of Cornwell and Nair's results are presented in Fig. 2.38 and compared with theory. Cornwell and Nair found that some indication of the $\dot{q}/\Delta T$ curve for boiling within a wick could be obtained by assuming that boiling occurs only on the liquid-covered area of the heating surface (measured from observations) and that $\dot{q}$ based on this area may be expressed by a nucleate boiling type correlation:

$$\dot{q} = C\Delta T^a$$

where C is a constant and a is in the range 2–6.

The results of Brautsch [45] followed the same trends as those of Cornwell and Nair. The enhancement due to a mesh wick at low heat fluxes, and the reduction in heat transfer due to the wick at higher heat fluxes, was explained in terms of the competing effects of additional nucleation sites and vapour blocking the liquid in the wick; the resulting correlation is given as Eq. (2.82).

These analyses are restricted to situations where the vapour formed in the wick escapes through the wick surface, and not out of the sides or through grooves in the heating surface.

A different approach was taken by Nishikawa and Fujita [71], who have investigated the effect of bubble population density on the heat flux limitations and the degree of superheat. While this work is restricted to flat surfaces, the authors' suggested nucleation factor may become relevant in studies where the wick contains channels or consists solely of grooves, possibly flooded, in the heat pipe wall.

The work of Saaski [72] on an inverted meniscus wick is of considerable interest. This concept, illustrated in Fig. 2.39, embodies in the high heat transfer coefficient of the circumferential groove while retaining the circumferential fluid transport capability of a thick sinter or wire mesh wick. With ammonia, heat transfer coefficients in the range 2–2.7 W/m^2 K were measured at radial heat flux densities of 20 W/cm^2. These values were significantly higher than those obtained for other non-boiling evaporative surfaces. Saaski suggested that the heat transfer enhancement may be due to film turbulence generated by vapour shear, or surface tension–driven convection. He contemplated an increase in groove density as one way of increasing the heat transfer coefficient, as first results have indicated a direct relationship between groove density and heat transfer coefficient. Vapour resulting from evaporation at the inverted meniscus interface flows along to open ends of the grooves, where it enters the central vapour core.
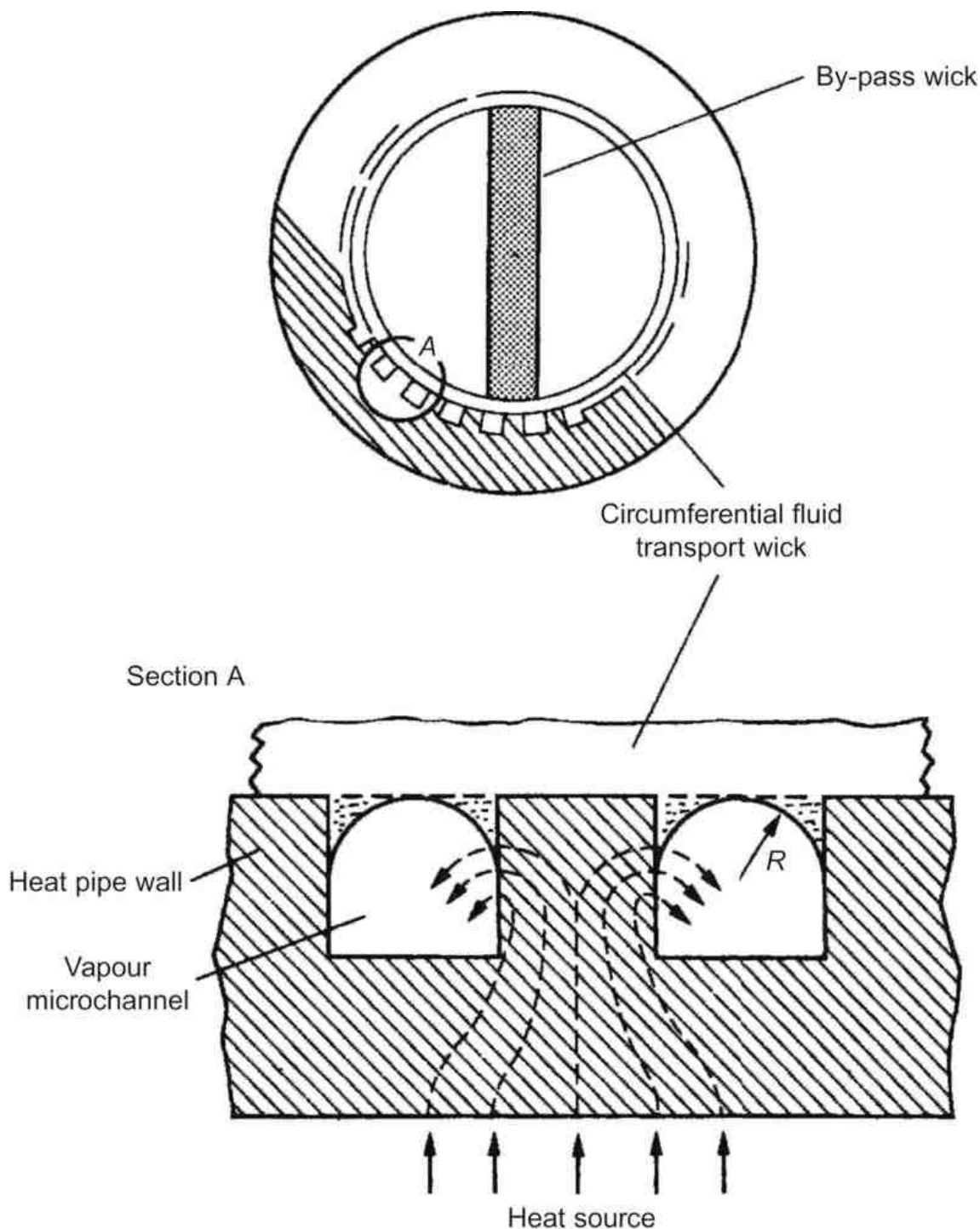
Figure 2.39: High performance inverted meniscus hybrid wick proposed by Saaski [72]

The main theoretical requirement for inverted meniscus operation, according to Saaski, is the maintenance of a sufficiently low vapour pressure drop in each channel of the wick. Recession of the inverted meniscus, which is the primary means of high evaporative heat transfer, reduces capability considerably. The equation given below describing the heat flux capability contains a term (j) which is a function of vapour microchannel pressure drop, being defined as the ratio of this pressure drop the maximum capillary priming potential.

Thus, $j = (\Delta P_v / (2\sigma / r_c))$

The heat flux q_{max} is defined by:

(2.100)
$$q_{\max} = \frac{jN^2 x^4}{8\pi} \left[\frac{\rho_v L \sigma}{\mu_v M} \right] \frac{1}{N^3 d_g^2 r_c}$$

$$x = \cos \frac{\Psi}{2} \Big/ \left[1 + \sin \frac{\Psi}{2} \right]$$

where Ψ is the groove angle (deg), M the molecular weight of working fluid, N the number of grooves per centimetre, d_g the heat pipe diameter at inner groove radius ($q_{\max}$ is given in W/cm^2 by Eq. (2.101)).

Feldman and Berger [73] carried out a theoretical analysis to determine surfaces having potential in a high heat flux water heat pipe evaporator. Following a survey of the literature, circumferential grooves were chosen, these being of rectangular and triangular geometry. The model proposed that:

i. at heat fluxes below nucleate boiling, conduction is the main mode of heat transfer and vaporisation occurs at the liquid–vapour interface without affecting capillary action;

ii. as nucleation progresses, the bubbles are readily expelled from the liquid in the grooves, with local turbulence, and convection becomes the main mode of heat transfer;

iii. at a critical heat flux, nucleation sites will combine forming a vapour blanket, or the groove will dry out.

Both (ii) and (iii) result in a sharp increase in evaporator temperature.

It is claimed that film coefficients measured by other workers supported the computer model predictions, and Feldman stated that evaporator film coefficients as high as 8 W/cm^2 K could be obtained with water as the working fluid. Using triangular grooves, it was suggested that radial fluxes of up to 150 W/cm^2 could be tolerated. However, such a suggestion appears largely hypothetical, bearing in mind the measured values given in Table 2.9.

Winston et al. [74] reported further progress on the prediction of maximum evaporator heat fluxes, including a useful alternative to Eq. (2.86). Based on modification of an equation first developed by Johnson [75] the relationship given below takes into account vapour friction in the wick evaporator section:

(2.101) $\dot{q}_{crit}$
$$= \frac{g[h_{co} \rho_{lo} (\sigma_1 / \alpha_{1o}) - \rho_1 (l_a + l_e) \sin \Phi]}{(l_e \mu_1 / L \rho_1 K \varepsilon (r_{cc} - r_v))[(l_e/2) + 1_a] + (\mu_v / K \rho_v)((r_{cc} - r_v)/(\varepsilon - \varepsilon_1)L)}$$

The solution of the equation was accomplished by arbitrarily varying the porosity for liquid flow, ε_1 from zero to a maximum given by the wick porosity ε. The portion of the wick volume not occupied by liquid was assumed to be filled with vapour. Eq. (2.101) has been used to predict critical heat fluxes, and a comparison with measured values for water has shown closer agreement than that obtained using Eqs (2.86) and (2.87), although the validity of these two latter equations is not disputed for liquid metal heat pipes.

2.4.1.4 Gravity-Assisted Heat Pipes

The use of gravity-assisted heat pipes, as opposed to reliance on simple thermosyphons, has been given some attention. The main areas of study have centred on the need to optimise the fluid inventory, and to develop wicks which will minimise entrainment. Deverall and Keddy [76] used helical arteries, in conjunction with meshes for evaporator liquid distribution, and obtained relatively high axial fluxes, albeit with sodium and potassium as the working fluids. This, together with the work of Kemme [25], led to the recommendation that more effort be devoted to the vapour flow limitations in gravity-assisted heat pipes. The work was restricted to heat pipes having liquid metal working fluids, and the significance in water heat pipes is uncertain.

However, for liquid metal heat pipes, Kemme discusses in some detail a number of vapour flow limitations in heat pipes operating with gravity assistance. As well as the pressure gradient limit discussed above, Kemme presents equations for the viscous limit, described by Busse as:

(2.102) $\dot{q}_v = \frac{A_v D^2 L}{64 \mu_v l_{eff}} \rho_{ve} P_{ve}$

where A_v is the vapour space cross-sectional area, D is the vapour passage diameter and suffix 'e' denotes conditions in the evaporator. Kemme also suggested a modified entrainment limitation to cater for additional buoyancy forces during vertical operation:

(2.103)
$$\dot{Q}_{max} = A_v L \left[\frac{\rho_v}{A} \left(\frac{2\pi\gamma}{\lambda} + \rho g D \right) \right]^{1/2}$$

where λ is the characteristic dimension of the liquid–vapour interface, and was calculated as d_w plus the distance between the wires of the mesh wick used. $\rho g d$ is the buoyancy force term.

Abhat and Nguyen-chi [67] report work carried out at IKE, Stuttgart, on gravity-assisted copper/water heat pipes, retaining a simple mesh wick located against the heat pipe wall. Tests were carried out with heat pipes at a number of angles to the horizontal, retaining gravity assistance, with fluid inventories of up to five times that required to completely saturate the wick. Thus a pool of liquid was generally present in at least part of the evaporator section. The basis of the analysis carried out by Abhat and Nguyen-chi to compare their experimental results with theory was the model proposed by Kaser [77]which assumed a liquid puddle in the heat pipe varying along the evaporator length from zero at the end of the heat pipes to a maximum at the evaporator exit. Results obtained by varying the operating temperature, tilt angle and working fluid inventory (see Fig. 2.40) were compared with Kaser's model, which was, however, found to be inadequate. Kaser believed that the limiting value of heat transport occurred when the puddle commenced receding from the end of the evaporator. However, the results of Abhat and Nguyen-chi indicate that the performance is limited by nucleate boiling in the puddle. While these results are of interest, much more work is needed in this area. Strel'tsov [78] carried out a theoretical and experimental study to determine the optimum quantity of fluid to use in gravity-assisted units. Without quantifying the heat fluxes involved, he derived expressions to permit determination of the fluid inventory. Of particular interest was his observation that film evaporation, rather than nucleation, occurred under all conditions in the evaporator section, using water and several organic fluids, this seeming to contradict the findings of Abbat and Nguyen-chi, assuming that Strel'tsov achieved limiting heat fluxes. Strel'tsov derived the following expression for the optimum fluid inventory for a vertical heat pipe:

(2.104)
$$G = (0.8l_c + l_a + 0.8l_e) \sqrt[3]{\frac{3\dot{Q}\mu_1\rho_1\pi^2D^2}{Lg}}$$
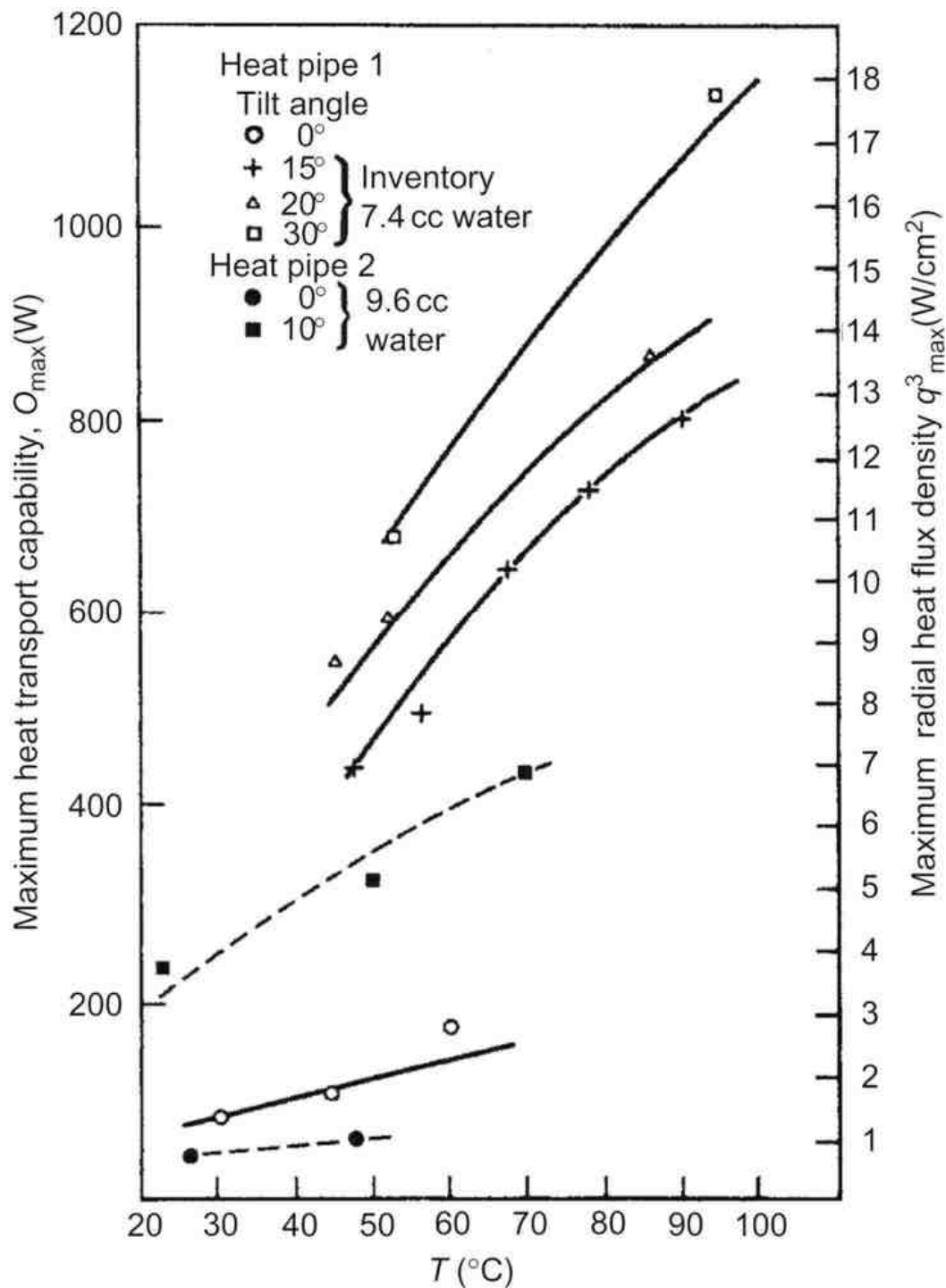
Figure 2.40: The effect of temperature on heat pipe performance for various tilt angles (gravity-assisted angle measured from the horizontal) [69]

where $\dot{Q}$ is the heat transport (W).

For a given heat pipe design and assumed temperature level, the dependence of the optimum quantity of the working fluid is given by the expression:

$$G = K\sqrt[3]{\dot{Q}}$$

where K is a function of the particular heat pipe under consideration.

The predicted performance of a heat pipe using methanol as the working fluid at a vapour temperature of 55°C is compared with measured values in Fig. 2.41.
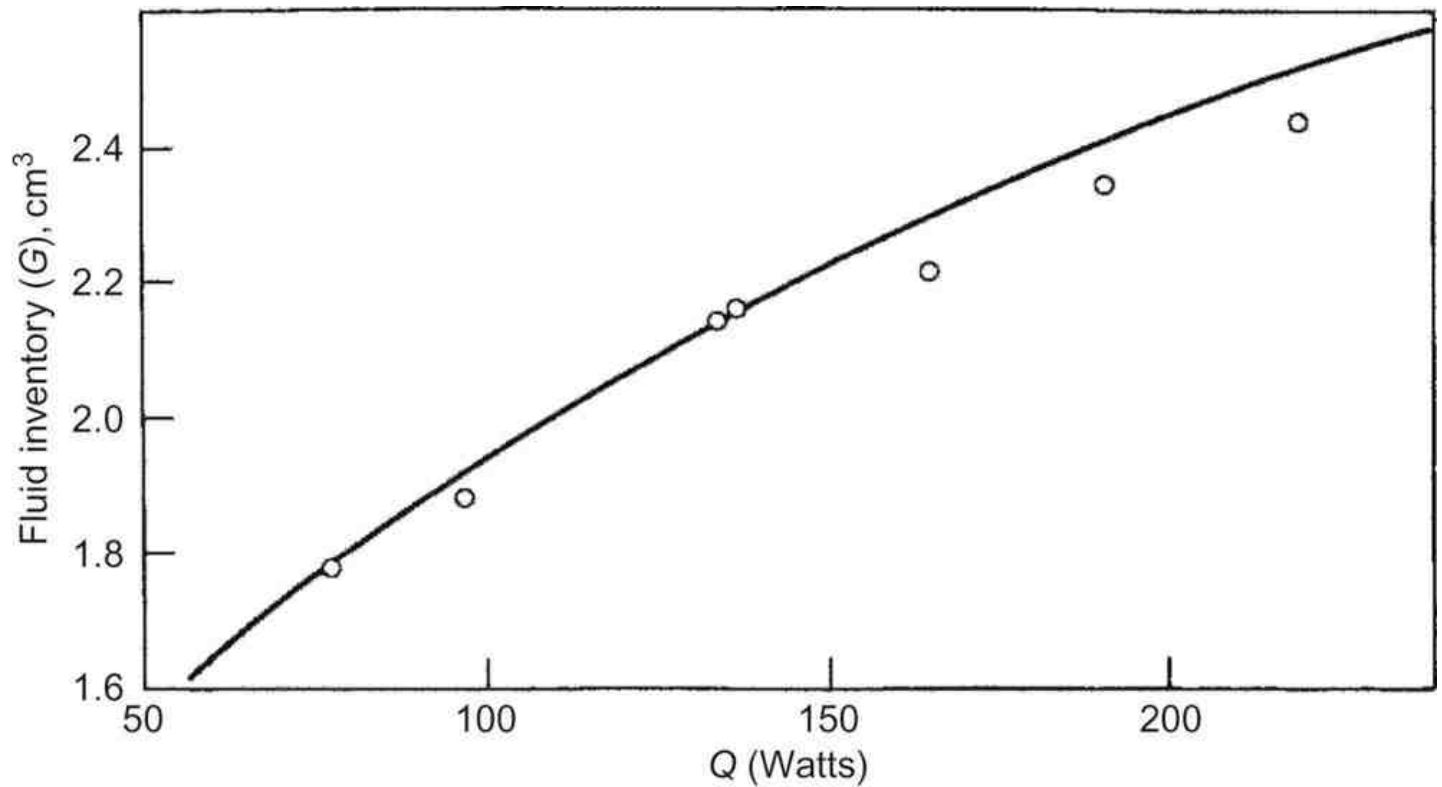
Figure 2.41: The measured effect of fluid inventory on the performance of a methanol heat pipe, and a comparison with results predicted by Eq. (2.104) [78]

The use of arteries in conjunction with grooved evaporator and condenser surfaces has been proposed by Vasiliev and Kiselyov [79]. The artery is used to transfer condensate between the condenser and evaporator, thus providing an entrainment-free path, while triangular grooves in the evaporator and condenser wall are used for distribution and collection of the working fluid. It is claimed that this design has a higher effective thermal conductivity than a simple thermal syphon, particularly at high heat fluxes.

The equation developed for the maximum heat flux of such a heat pipe is:

(2.105) $\quad \hat{q}_{max}(W/m^2) = 3.26 \times 10^{-2} a \cos\frac{\Psi}{2} \cos\theta \cdot \theta(\Psi) \cdot \frac{\sigma \rho_l L}{\mu_l}$

where a is the groove width, Ψ the groove angle, θ the contact angle and

$$ f(\Psi) = \left[tg\Psi + c \cdot tg\Psi - \frac{((\pi/2) - \Psi)}{\cos^2\Psi} \right]^3 \cos^2\Psi $$

Other data on gravity-assisted heat pipes, in particular dry-out limits, suggests that two contrary types of dry-out can be shown to exist. Busse and Kemme [80] state that the 'axial dry-out' arises from a lack of hydrostatic driving force and makes itself evident when the heat flux increases. The so-called 'azimuthal dry-out' is, however, caused by an excess of hydrostatic driving force, and was found to be characterised by a concentration of the liquid flow on the lower part of the heat pipe cross section, without any lack of axial liquid return. It was recommended that graded capillary structures were the best technique for overcoming this limit.

Of particular interest is the use of wick-type structures in thermosyphons for enhancing internal heat transfer coefficients. As part of a project leading to the development of improved heat pipe exchangers, UKAEA Harwell inserted longitudinal grooves in the walls of thermosyphons. Using plain bore thermosyphons of near-rectangular cross section, of 1 m length, with 10% of the vapour space filled with water, a series of measurements of evaporator and condenser heat transfer coefficients was made. Vapour temperatures varied from 40°C to 120°C, with power inputs of 2 and 3 kW [81].

Heat transfer coefficients varied from 15 to 21 kW/m^2 °C, with a mean for the evaporator of 17,755 W/m^2 °C and for the condenser of 17,983 W/m^2 °C.

However, with grooves on the inside wall along the complete l_m length, tests carried out with 3 kW power input revealed that condenser heat transfer coefficients of 50–100 kW/m^2 °C were achieved, a mean of 62,061 W/m^2 °C being recorded.

2.4.1.5 Total Temperature Drop

Referring back to Fig. 2.21 shows the components of the total temperature drop along a heat pipe and the equivalent thermal resistances.

- R_1 and R_9 are the normal heat transfer resistances for heating a solid surface and are calculated in the usual way.

- R_2 and R_8 represent the thermal resistance of the heat pipe wall.

- R_3 and R_7 take account of the thermal resistance of the wick structure and include any temperature difference between the wall and the liquid together with conduction through the saturated wick. From the discussion in Section 2.3.7.4 it is seen that the calculation of R_3 is difficult if boiling occurs. R_7 is made up principally from the saturated wick but if there is appreciable excess liquid then a correction must be added.

- R_4 and R_6 are the thermal resistances corresponding to the vapour–liquid surfaces. They may be calculated from Eq. (2.89) but can usually be neglected.

- R_5 is due to the temperature drop ΔT_5 along the vapour column. ΔT_5 is related to the vapour pressure drop ΔP by the Clapeyron equation.

$$\frac{dP}{dT} = \frac{L}{TV_v}$$

or combining with the gas equation

$$\frac{dP}{dT} = \frac{LP}{RT^2}$$

Hence,

(2.106) $\quad \Delta T_5 = \frac{RT^2}{LP} \Delta P_v$

where ΔP_V is obtained from Section 2.5 and ΔT_5 can usually be neglected.

- R_s is the thermal resistance of the heat pipe structure, and it can normally be neglected but may be important in the start-up of gas-buffered heat pipes.

It is useful to have an indication of the relative magnitude of the various thermal resistances (Table 2.10) (from Asselman and Green [60]) lists some approximate values/cm^2 for a water heat pipe.

Table 2.10:
Representative Values
of Thermal Resistances

Resistance	°C cm^2/W
R_1	10^3–10
R_2	10^{-1}
R_3	10
R_4	10^{-5}
R_5	10^{-8}
R_6	10^{-5}
R_7	10
R_8	10^{-1}
R_9	10^3–10

Expressions for calculation of thermal resistance are given in Table 2.11.

Table 2.11: Summary of Thermal Resistances in a Heat Pipe

Term	Defining Relation	Thermal Resistance	Comment
1	$\dot{Q}_i = \alpha_e A_e \Delta T_1$	$R_1 = \dfrac{1}{\alpha_e A_e}$	

Note R_X = Thermal resistance = (temperature difference/heat flow) = $(\Delta T / \dot{Q})_X$

Total heat flow = $\dot{Q}_i = Q + \dot{Q}_s$, $Q, \dot{Q}_i$ and $\dot{Q}_s$ are defined in Fig. 2.21.

Heat flux = $\dot{q} = (\dot{Q}/A)$

ΔT_X and R_X are defined in Fig. 2.21.

Other symbols:

$\dot{q}_e, \dot{q}_c$ heat flux through the evaporator and condenser walls

k thermal conductivity of the heat pipe wall

t heat pipe wall thickness

r_1, r_2 inner and outer radii of cylindrical heat pipe

d wick thickness

k_w effective wick thermal conductivity

P_v vapour pressure

L latent heat

R gas constant for vapour

T absolute temperature

ΔP_v total vapour pressure drop in the heat pipe

A_w cross-sectional area of wick

A_{wall} cross-sectional area of wall

Table 2.11: Summary of Thermal Resistances in a Heat Pipe

Term	Defining Relation	Thermal Resistance	Comment
2	Plane geometry $\dot{q}_e = \dfrac{k\Delta T_2}{t}$ Cylindrical geometry $\dot{q}_e = (k\Delta T_2 / r_2 \ln(r_2/r_1))$	$R_2 = \dfrac{\Delta T_2}{A_e \dot{q}_e}$	For thin-walled cylinders $r_2 \ln \dfrac{r_2}{r_1} = t$
3	Equation (2.91) or (2.92)	$R_3 = \dfrac{d}{k_w A_e}$	Correct for liquid metals. Gives upper limit for non-metallics
4	$\dot{q}_e = \dfrac{L^2 P_v \Delta T_4}{(2\pi RT)^{0.5} RT^2}$	$R_4 = \dfrac{(2\pi RT)^{0.5} RT^2 L^2 P_v \Delta T_4}{L^2 P_v A_e}$	Can usually be neglected
5	$\Delta T_5 = \dfrac{RT^2 \Delta P_v}{L P_v}$	$R_5 = \dfrac{RT^2 \Delta P_v}{\dot{Q} L P_v}$	Can usually be neglected ΔP_v from Section 2.3.5
6	$\dot{q}_e = \dfrac{L^2 P_v \Delta T_6}{(2\pi RT)^{0.5} RT^2}$	$R_6 = \dfrac{(2\pi RT)^{0.5} RT^2 L^2 P_v \Delta T_4}{L^2 P_v A_c}$	Can usually be neglected
7	Equation (2.91) or (2.92)	$R_7 = \dfrac{d}{k_w A_c}$	If excess working fluid is present, an allowance should be made for the additional resistance
8	Plane geometry $\dot{q}_e = \dfrac{k\Delta T_8}{t}$ Cylindrical geometry $\dot{q}_e = (k\Delta T_8 / r_2 \ln(r_2/r_1))$	$R_8 = \dfrac{\Delta T_8}{A_e \dot{q}_e}$	For thin-walled cylinders $r_2 \ln \dfrac{r_2}{r_1} = t$
9	$\dot{Q}_i = \alpha_e A_e \Delta T_1$	$R_9 = \dfrac{1}{\alpha_e A_e}$	
	$\dot{Q}_s = \Delta T_s /((l_e + l_a + l_c)/(A_w k_w + A_{wall} k))$	$R_s = \dfrac{l_e + l_a + l_c}{A_w k_w + A_{wall} k}$	Axial heat flow by conduction

Note R_X = Thermal resistance = (temperature difference / heat flow) = $(\Delta T / \dot{Q})_X$

Total heat flow = $\dot{Q}_i = Q + \dot{Q}_s$, $\dot{Q}$, $\dot{Q}_i$ and $\dot{Q}_s$ are defined in Fig. 2.21.

Heat flux = $\dot{q} = (\dot{Q}/A)$

ΔT_X and R_X are defined in Fig. 2.21.

Other symbols:

$\dot{q}_e, \dot{q}_c$ heat flux through the evaporator and condenser walls

k thermal conductivity of the heat pipe wall

t heat pipe wall thickness

r_1, r_2 inner and outer radii of cylindrical heat pipe

d wick thickness

k_w effective wick thermal conductivity

P_v vapour pressure

L latent heat

R gas constant for vapour

T absolute temperature

ΔP_v total vapour pressure drop in the heat pipe

A_w cross-sectional area of wick

A_{wall} cross-sectional area of wall

2.4.2 Thermosyphons

2.4.2.1 Working Fluid Selection

Obviously there is no equivalent of the wicking limit, due to the absence of a wick in a thermosyphon. However, the temperature drop may be appreciable, in which case the fluid must be selected to minimise this. A figure of merit M' may be defined for thermosyphon working fluids. This figure of merit, which has the dimensions

$$\frac{kg}{K^{3/4} s^{5/2}}$$

is defined as:

(2.107) $\qquad M' = \left(\dfrac{L k_l^3 \rho_l^2}{\mu_l}\right)^{1/4}$

where k_l is the liquid thermal conductivity.

As with the heat pipe figure of merit, M' should be maximised for optimum performance. Data on M' for a variety of working fluids of use in the vapour temperature ranging from −60°C to 300°C are presented in Ref. [82], in graphical and tabulated form.

The maximum value of M' for several working fluids, together with the corresponding temperature is given in Table 2.12.

Table 2.12: Maximum Thermosyphon Merit Number for Selected Fluids

Fluid	Temperature (°C)	M' max $(kg/K^{3/4} s^{5/2})$
Water	180	7542
Ammonia	−40	4790
Methanol	145	1948
Acetone	0	1460
Toluene	50	1055

The thermosyphon merit number is relatively insensitive to temperature, for example water remains above 4000 for the range 0.01°C–350°C.

A potential disadvantage of water as a working fluid is that if a thermosyphon may be exposed to temperatures below 0°C prior to operation freezing may impede start-up of the thermosyphon. MacGregor et al. [83] have shown that a water–5% ethylene glycol gives good performance, and further widens the applicability of water as a thermosyphon working fluid. Further data on

this work are given in Section 5.3.4.

2.4.2.2 Entrainment Limit

The limit is described by Nguyen-chi and Groll [84] where it is also called the flooding limit – as the condenser becomes flooded – and in the ESDU Data Item on thermosyphons [85] – where it is additionally described as the counter-current flow limit. A correlation derived in Ref. [86] gives good agreement with the available experimental data. For thermosyphons, this gives the maximum axial vapour mass flux as:

(2.108) $\quad Q_{max}/AL = f_1 f_2 f_3 (\rho_v)^{0.5} [g(\rho_l - \rho_v)\sigma_1]^{0.25}$

where f_1 is a function of the Bond number, defined as:

(2.109) $\quad Bo = D \dfrac{g(\rho_l - \rho_v)^{0.5}}{\rho_l}$

Values of f_1 can be obtained from Fig. 2.42, where it is plotted against Bo.
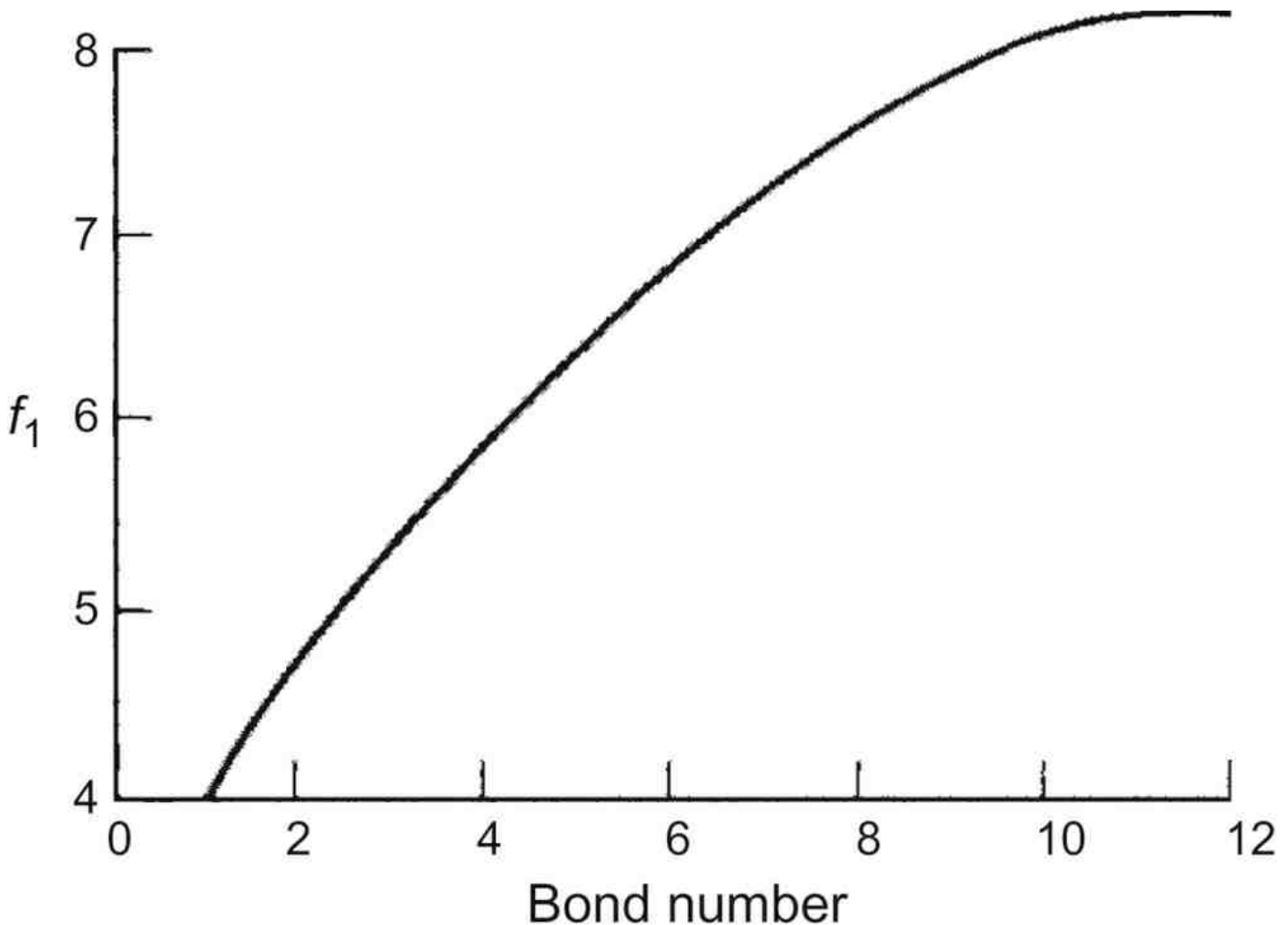
Figure 2.42: Variation of factor f_1 with Bond number

The factor f_2 is a function of a dimensionless pressure parameter, K_p, where K_p is defined in Ref. [84] as:

(2.110) $\quad K_p = \dfrac{P_v}{g(\rho_l - \rho_v)\sigma_1^{0.5}}$

and

$f_2 = K_p^{-0.17} \quad$ when $\quad K_p \le 4 \times 10^4$

$f_2 = K_p^{-0.17} \quad$ when $\quad K_p > 4 \times 10^4$

The factor f_3 is a function of the inclination angle of the thermosyphon. When the thermosyphon is operating vertically, $f_3=1$; when the unit is inclined, the value of f_3 may be obtained by reading Fig. 2.43, where it is plotted against the inclination angle to the horizontal, φ, for various values of the Bond number. (Note that the product f_1, f_2, f_3 is sometimes known as the Kutateladze number.)
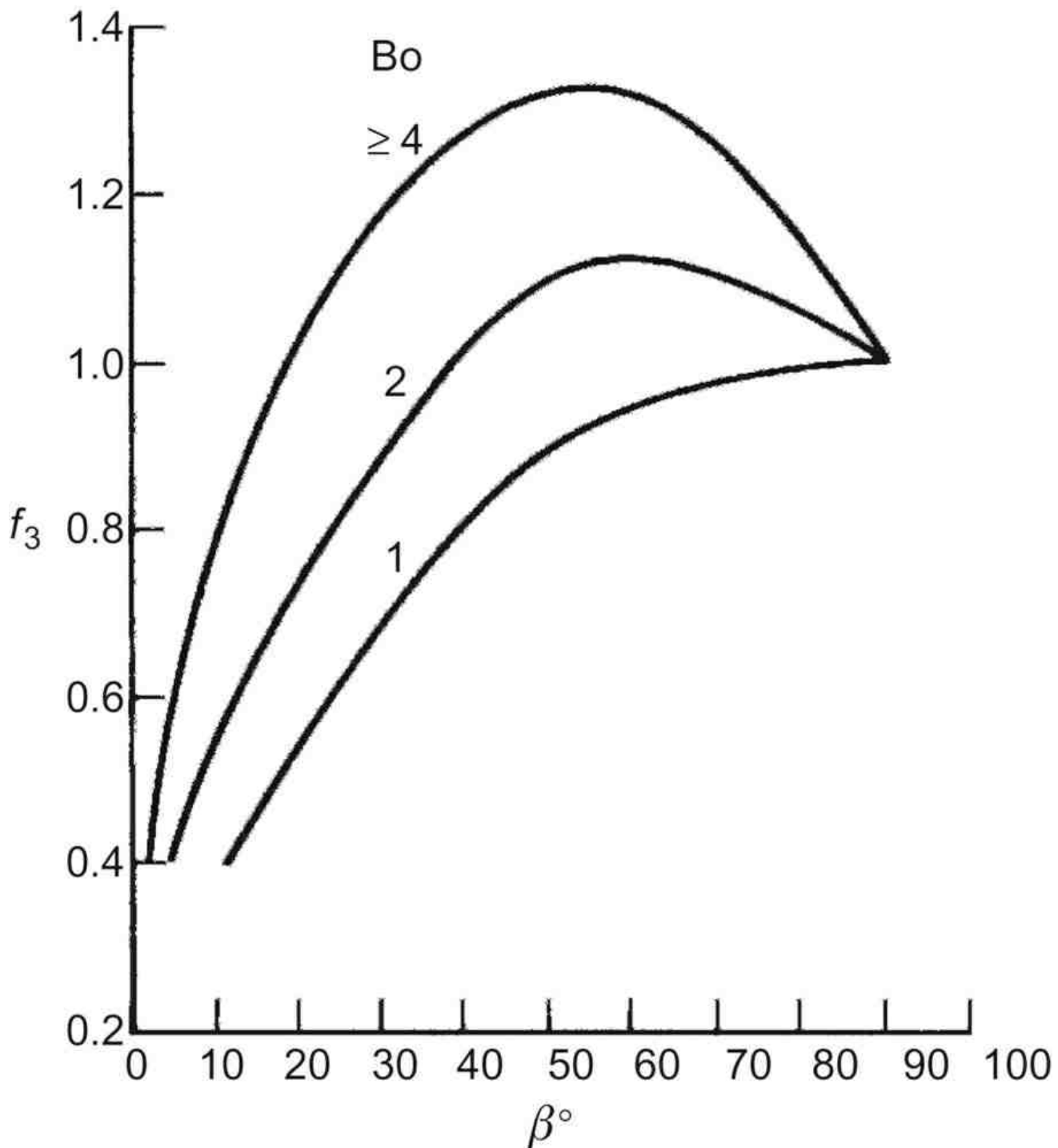
Figure 2.43: Variation of factor f_3 with thermosyphon inclination angle and Bond number

Note that much of the experimental evidence on the performance of thermosyphons indicates that the maximum heat transport capability occurs when the thermosyphon is at 60°–80° to the horizontal, i.e. not vertical. Data are given by Groll [87] and Terdtoon et al. [85] concerning this behaviour.

2.4.2.3 Thermal Resistance and Maximum Heat Flux

Payakaruk et al. [88] has investigated the influence of inclination angle on thermosyphon performance and have correlated the minimum resistance R_m to the resistance of the thermosyphon, R_{90}, in the vertical position. This correlation is shown in Eq. (2.111) (Fig. 2.44).

(2.111) $R_m/R_{90} = 0.647 Ku^{0.0297}$

• W d=7.5 mm	□ W d=11.1 mm	◐ W d=25.4 mm	✷ Water d=7.5 mm	✶ Water d= 11.1 mm
• Water d=25.4 mm	◆ E d=7.5 mm	◨ E d=11.1 mm	◐ E d=25.4 mm	✶ Ethanol d=7.5 mm
✕ Ethanol d=11.1 mm	✦ Ethanol d=25.4 mm	◐ Ra d=7.5 mm	◨ Ra d=11.1 mm	◐ Ra d=25.4 mm
✕ R134a d=7.5 mm	✦ R 134a d=11.1 mm	◐ R123 d=7.5 mm	◐ R123 d=25.4 mm	
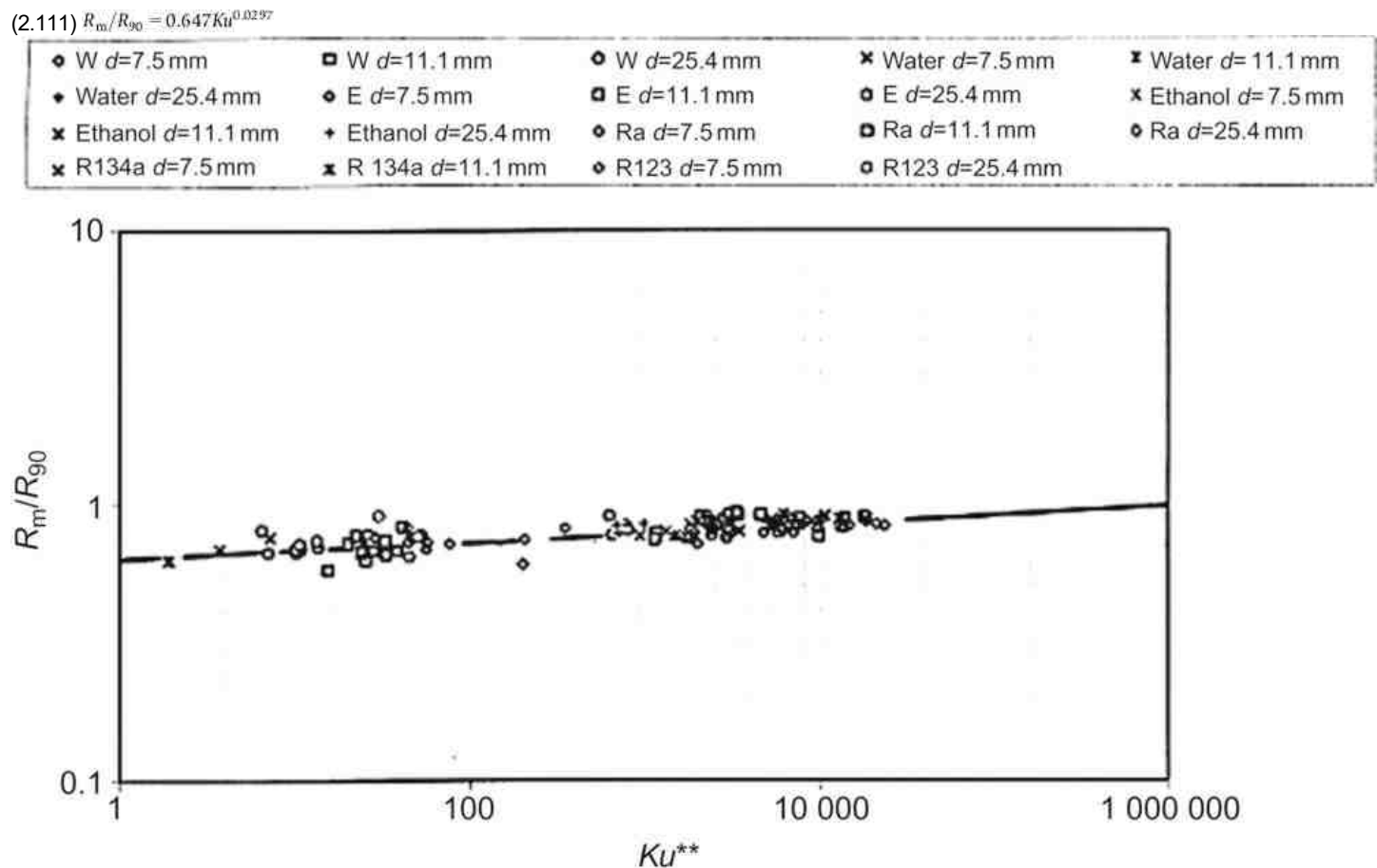
Figure 2.44: (R_m/R_{90}) as a function of Ku^{**} for a range of operating conditions compared with Eq. (2.111) [88]

where

$$Ku = \frac{\dot{q}}{L\rho_v[\sigma_1 g(\rho_1 - \rho_v)/\rho_v^2]^{0.25}}$$

and

$$Ku^{**} = Ku \times \frac{l_e}{2r_v} \times \frac{\rho_1}{\rho_v}$$

Golobic and Gaspersic [101] have conducted a review of correlations for the prediction of thermosyphon maximum heat flux and developed a correlation based on the principle of corresponding states. This formulation has the advantage of requiring little data regarding fluid properties – only molecular weight, critical temperature, critical pressure and Pitzer acentric factor are needed. The acentric factor may be calculated from:

(2.112) $\omega = -1 - \log(p/p_{c(Tr=0.7)})$

hence requiring knowledge of the vapour pressure at a reduced pressure of 0.7 (Table 2.13).

Table 2.13: Correlations for the Maximum Heat Flux in Thermosyphons [89]

Reference	Correlations Kutateladze Number $Ku = q_{co}/\{\Delta h_{lv} \rho_v^{0.5}[\sigma g(\rho_1 - \rho_v)]^{0.25}\}$
Sakhuja [90]	$Ku = \frac{0.725^2}{4} Bo^{1/2} \frac{(d_e/l_e)}{[1 + (\rho_v/\rho_1)^{1/4}]^2}$
Nejat [91]	$Ku = 0.09 Bo^{1/2} \frac{(d_e/l_e)^{0.9}}{[1 + (\rho_v/\rho_1)^{1/4}]^2}$
Katto [92]	$Ku = \frac{0.1}{1 + 0.491(l_e/d_e)Bo^{-0.3}}$

Table 2.13: Correlations for the Maximum Heat Flux in Thermosyphons [89]

Reference	Correlations Kutateladze Number $Ku = q_{co}/\{\Delta h_{lv}\rho_v^{0.5}[\sigma g(\rho_1 - \rho_v)]^{0.25}\}$
Tien and Chang [93]	$Ku = \dfrac{3.2(d_e/l_e)}{4[1 + (\rho_v/d_1)^{1/4}]^2}; \quad Bo \geq 30$
	$Ku = \dfrac{3.2}{4}[\tan h(0.5Bo^{1/2})]^2 \dfrac{(d_e/l_e)}{[1 + (\rho_v/\rho_1)^{1/4}]^2}$
Harada et al. [94]	$Ku = 9.64(d_e/l_e)\rho_v h_{lv} C\left(\dfrac{\sigma}{\rho_v}\right)^{1/2}; \quad C\left(\dfrac{\sigma}{\rho_v}\right)^{1/2} \geq 0.079$
	$Ku = 14.1(d_e/l_e)\rho_v h_{lv}\left[C\left(\dfrac{\sigma}{\rho_v}\right)^{1/2}\right]^{1.15}; \quad C\left(\dfrac{\sigma}{\rho_v}\right)^{1/2} \geq 0.079$
	$C = 1.58\left(\dfrac{d_e}{\sigma}\right)^{0.4}; \dfrac{d_e}{\sigma} < 0.318 \quad C = 1; \dfrac{d_e}{\sigma} \geq 0.318$
Gorbis and Savchenkov [95]	$Ku = 0.0093(d_e/l_e)^{1.1}(d_e/l_e)^{-0.88}F_e^{-0.74}\times(1+0.03Bo)^2; \quad 2 < Bo < 60$
Bezrodnyi [96]	$Ku = 2.55(d_e/l_e)\left\{\dfrac{\sigma}{\rho}\left[\dfrac{g(\rho_1-\rho_v)}{\sigma}\right]^{1/2}\right\}^{0.17}; \dfrac{\sigma}{\rho}\left[\dfrac{g(\rho_1-\rho_v)}{\sigma}\right]^{1/2} \geq 2.5\cdot10^{-5}$
	$Ku = 0.425(d_e/l_e); \dfrac{\sigma}{\rho}\left[\dfrac{g(\rho_1-\rho_v)}{\sigma}\right]^{1/2} < 2.5\cdot10^{-5}$
Groll and Rösler [97]	$Ku = f_{1(Bo)}f_2 f_{3(\varphi,Bo)}(d_e/l_e)$
	$f_2 = 0.165; \quad \dfrac{\sigma}{\rho}\left[\dfrac{g(\rho_1-\rho_v)}{\sigma}\right]^{1/2} \geq 2.5\cdot10^{-5}$
Prenger [98]	$Ku = 0.747(d_e/l_e)[g\sigma(\rho_1 - \rho_v)]^{0.295}(h_{lv}\rho_v)^{-0.45}$
Fukano et al. [99]	$Ku = 2(d_e/l_e)^{0.83}P_e^{0.03}\left\{\dfrac{[\sigma g(\rho_1 - \rho_v)]^{1/2}}{h_{lv}\rho_v}\right\}^{0.2}$
Imura et al. [100]	$Ku = 0.16\{1 - \exp[-(d_e/l_e)(\rho_1 - \rho_v)^{0.13}]\}$
Pioro. and Voronenva [101]	$Ku = 0.131\{1 - \exp[-(d_e/l_e)(\rho_1/\rho_v)^{0.13}\cos^{1.8}(\varphi - 55°)]\}^{0.8}$
Golobic and Gaspersic [102]	$q_{co} = \dfrac{0.16d_e T_c^{1/3}p_c^{11/12}g^{1/4}}{l_e M^{1/4}}\tau\exp(2.530 - 8.233\tau + 1.387\omega + 17.096\tau^2)$
	$- 4.944\tau\omega^2 + 15.542\tau^2\omega^2 - 23.989\tau^3 - 19.235\tau^3\omega - 18.071\tau^3\omega^2$
	$q_{co} = \dfrac{0.16d_e T_c^{1/3}p_c^{11/12}g^{1/4}}{l_e M^{1/4}}\tau\exp(2.530 - 13.137\tau^2)$

Additional Nomenclature for Table 2.13

Nomenclature	
Bo	Bond number $= d_e/[g(\rho_1 - \rho_v)/\sigma]^{0.5}$
C	Parameter in equation (T6)
d_e	Evaporator diameter (m)
f_1, f_2, f_3	Parameters in equation (T9)
F_e	Fill ratio, liquid fill volume/evaporator volume
g	Gravitational acceleration (m/s^2)
Ku	Kutateladze number $= q_{co}/\{\Delta h_{lv}\rho_v^{0.5}[\sigma g(\rho_1 - \rho_v)]^{0.25}\}$
l_e	Evaporator length (m)
M	Molecular weight (kg/kmol)
p_c	Critical pressure (Pa)
q_{co}	Maximum heat flux (W/m^2)
T	Temperature (K)
T_r	Reduced temperature $= T/T_c$
T_c	Critical temperature (K)
x_1	Fluid properties parameter, Eq. (2.2)
x_2	Density ratio parameter, Eq. (2.3)
Δh_{1v}	Heat of evaporation (J/Kg)
φ	Inclination angle (°)
μ	Dipole moment (debye)
ρ_1	Liquid density (kg/m^3)
ρ_v	Vapour density (kg/m^3)
σ	Surface tension (N/m)
τ	Temperature function $= 1 - T_r$
ω	Pitzer acentric factor

2.5 NANOFLUIDS

There has been considerable interest in recent years in the use of nanofluids in various heat transfer applications. Nanofluids, first defined by Choi [103] in 1995 as base fluids, contain a suspension of nanometer-sized particles. The base fluid is typically a conventional heat transfer fluid such as water, ethylene glycol and oils. The range of nanoparticles used includes pure metals, metal oxides, carbides and nitrides and various forms of carbon. Liu and Li [104] reviewed the published application of nanofluids to heat pipes and identified some 40 experimental studies relating to various types of heat pipe including loop and oscillating heat pipes discussed in Chapter 6. The majority of studies show that under at least some conditions, the thermal resistance of the heat pipes or thermosyphons tested was lower with the addition of nanoparticles to the base fluid compared to that measured with the base fluid alone.

The reported results are summarised in Table 2.14, together with additional selected papers published after Ref. [104].

Table 2.14: Summary of Researches of Heat Pipes Using Nanofluids [104]

Type and Shape of Heat Pipe		Researcher	Working Liquid Type (Nanoparticle Size and Optimal Concentration)	Effect
Miniature micro-grooved heat pipe	Disk shaped	Chien et al. [105]	Au–water (17 nm)	+
	Cylindrical	Wei et al. [106]	Ag–water (10 nm, 0.01 wt%)	+
	Cylindrical	Kang et al. [107]	Ag–water (35 nm, 0.01 wt%)	+
	Cylindrical	Yang et al. [108]	CuO–water (50 nm, 1.0 wt%)	+
	Cylindrical	Liu and Lu [109]	CNT–water (diameter: 15 nm, length: 5–15 μm, 2.0 wt%)	+
	Flat	Do and Jang [110]	Al_2O_3–water (38.4 nm, 0.8 wt%)	+
	Cylindrical	Shafahi et al. [111]	CuO–water, Al_2O_3–water, TiO_2–water	+
	Disk shaped	Shafahi et al. [112]	CuO–water, Al_2O_3–water, TiO_2–water	+
	Cylindrical	Liu et al. [113]	CuO–water (50 nm, 1.0 wt%)	+
	Cylindrical	Wang et al. [114]	CuO–water (50 nm, 1.0 wt%)	+
Mesh wick heat pipe	Cylindrical	Tsai et al. [115]	Au–water (21 nm)	+
	Cylindrical	Liu et al. [116]	CuO–water (50 nm, 1.0 wt%)	+
	Flat	Chen et al. [117]	Ag–water (35 nm, 0.01 wt%)	+
	Cylindrical	Do et al. [118]	Al_2O_3–water (30 nm, 2.4 wt%)	+
	Cylindrical	Liu et al. [119]	CuO–water (50 nm, 1.0 wt%)	+
	Cylindrical	*Senthilkumar et al.*[120]	*Cu-n-Aqueous soln n-Hexanol, (40 nm, 0.01 wt%)*	+
	Cylindrical	*Putra et al.*[121]	*Al_2O_3–water (1–5 vol%)*	+
			Al_2O_3–ethylene glycol (1–5 vol%)	+
			TiO_2–water (1–5 vol%)	+
			TiO_2–ethylene glycol (1–5 vol%)	+
			ZnO–ethylene glycol (1–5 vol%)	+
	Cylindrical	*Wang et al.*[122]		
Sintered metal wick heat pipe	Loop heat pipe	Riehl [123]	Ni–water (40 nm, 3.5 wt%)	–
	Cylindrical	Kang et al. [124]	Ag–water (10 nm, 0.01 wt%)	+
	Cylindrical	*Morajevi et al.*[125]	*Al_2O_3–water(35 nm 1–3 wt%)*	+
Oscillating heat pipe	Closed-loop OHP	Ma et al. [126]	Diamond–water (20 and 40 nm, 2.2 wt%)	+
	Closed-loop OHP	Ma et al. [127]	Diamond–water (20 and 40 nm, 2.2 wt%)	+
	Closed-loop OHP	Shang et al. [128]	Cu–water (25 nm, 0.45 wt%)	+
	Closed-loop OHP	Lin et al. [129]	Ag–water (20 nm, 0.1 wt%)	+
	Closed-loop OHP	Park and Ma [130]	CuNi–water (40–150 nm, 8.8 wt%)	+
	Closed-loop OHP	Qu et al. [131]	Al_2O_3–water (56 nm, 0.9 wt%)	+
	Closed-loop OHP	Bhuwakietkumjohn and Rittidech [132]	Ag–ethanol	+
	Flat-plate closed-loop OHP	Cheng et al. [133]	Diamond–acetone (2 nm, 0.33 wt%)	+
			Au–water (3 nm, 0.006 wt%)	+

"+" means heat transfer enhancement and "−" means heat transfer reduction.

Italicised references were added to this table from Ref. [104].

Table 2.14: Summary of Researches of Heat Pipes Using Nanofluids [104]

Type and Shape of Heat Pipe		Researcher	Working Liquid Type (Nanoparticle Size and Optimal Concentration)	Effect
			Diamond–water (2 nm, 2.6 wt%)	–
	Closed-loop OHP	Ji et al.[134]	Al_2O_3–water (50–20 µm, 0.5 wt%)	+
	Open-loop PHP	Taslimafar et al.[135]	Fe_3O_4–water (25 nm)	+
	Open-loop PHP	Riehl et al.[136]	Cu–water (29 nm, 5 wt%)	+
Closed two-phase thermosyphon	Cylindrical	Peng et al. [137]	Al–water (30 nm, 7.8 wt%)	+
	Cylindrical	Xue et al. [138]	CNT–water (15 nm, 2.2 wt%)	–
	Cylindrical	Liu et al. [139]	CuO–water (30 nm, 1.0 wt%)	+
	Flat	Liu et al. [140]	CuO–water (15–50 nm, 1.0 wt%)	+
	Cylindrical	Khandekar et al. [141]	Al_2O_3–water (40–47 nm, 1.0 wt%), CuO–water (8.6–13 nm, 1.0 wt%)	–
			Laponite clay–water (25 nm, 1.0 wt%)	
	Cylindrical	Naphon et al. [142]	Ti–alcohol (21 nm, 0.57 wt%)	+
	Cylindrical	Naphon et al. [143]	Ti–refrigerant R11 (21 nm, 0.31 wt%)	+
	Cylindrical	Noie et al. [144]	Al_2O_3–water (20 nm, 3.0 wt%)	+
	Cylindrical	Liu et al. [145]	CNT–water (15 nm, 2.0 wt%)	+
	Cylindrical	Parametthanuwat et al. [146]	Ag–water (<100 nm, 0.5 wt%)	+
	Cylindrical	Parametthanuwat et al. [147]	Ag–water (<100 nm, 0.5 wt%)	+
	Cylindrical	Huminic et al. [148]	Iron oxide–water (4–5 nm, 20% wt%)	+
	Cylindrical	Huminic et al. [149]	Iron oxide–water (4–5 nm, 20% wt%)	+
	Cylindrical	Qu and Wu[150]	SiO_2–Water, Al_2O_3–Water (30–56 nm, 0.1–1.2 wt%)	+
	Cylindrical	Hung et al.[151]	Al_2O_3–Water (10–30 nm, 0.5–3 wt%)	+

"+" means heat transfer enhancement and "−" means heat transfer reduction.

Italicised references were added to this table from Ref. [104].

The mechanisms through which addition of a small percentage of nanoparticles to a fluid are not fully explained and it is not presently possible to predict the enhanced performance. Although there is an increase in thermal conductivity associated with the addition of metallic particles to the enhancement observed, the improvement in performance which may be achieved is considerably higher than that which would be expected from consideration of the thermal transport properties alone.

The presence of nanoparticles in a fluid decreases the contact angle between a surface and the fluid. It has been observed through scanning electron microscopy that after operation the internal surfaces of a heat pipe, including the mesh, become covered with a thin layer comprising deposited nanoparticles. It is suggested that this may further reduce the contact angle. The capillary driving force in a mesh, micro-grooved or arterial wick heat pipe is thus increased.

The deposition of nanoparticles on the heat transfer surfaces is generally observed to decrease the thermal resistance within the evaporator and condenser. Putra et al. [121] examined the performance of a range of fluids and concentrations on the performance of a 200 mm long 7.4 mm diameter heat pipe with a 4-layer plaited mesh wick and from their results, reproduced in Table 2.15, it can be seen that the overall resistance of the heat pipe is reduced under almost all conditions. Examination of temperature profiles in the heat pipe, shown in Fig. 2.45, indicates that the heat transfer coefficients in both evaporator and condenser were significantly increased by the addition of nanoparticles to the water base fluid. The variation of the evaporator heat transfer coefficient is illustrated in Fig. 2.46.

Table 2.15: Thermal Resistance of a Heat Pipe with Various Working Fluids [121]

No.	Working Fluids	Thermal Resistance R_{e-a}(°C/Watt)		
		10 W	20 W	30 W
1	Ethylene glycol	2.44	2.28	2.16
2	Water	2.36	2.20	2.11
3	Al_2O_3–ethylene glycol	2.18	2.02	1.86
4	TiO_2–ethylene glycol	2.38	2.23	2.11

Table 2.15: Thermal Resistance of a Heat Pipe with Various
Working Fluids [121]

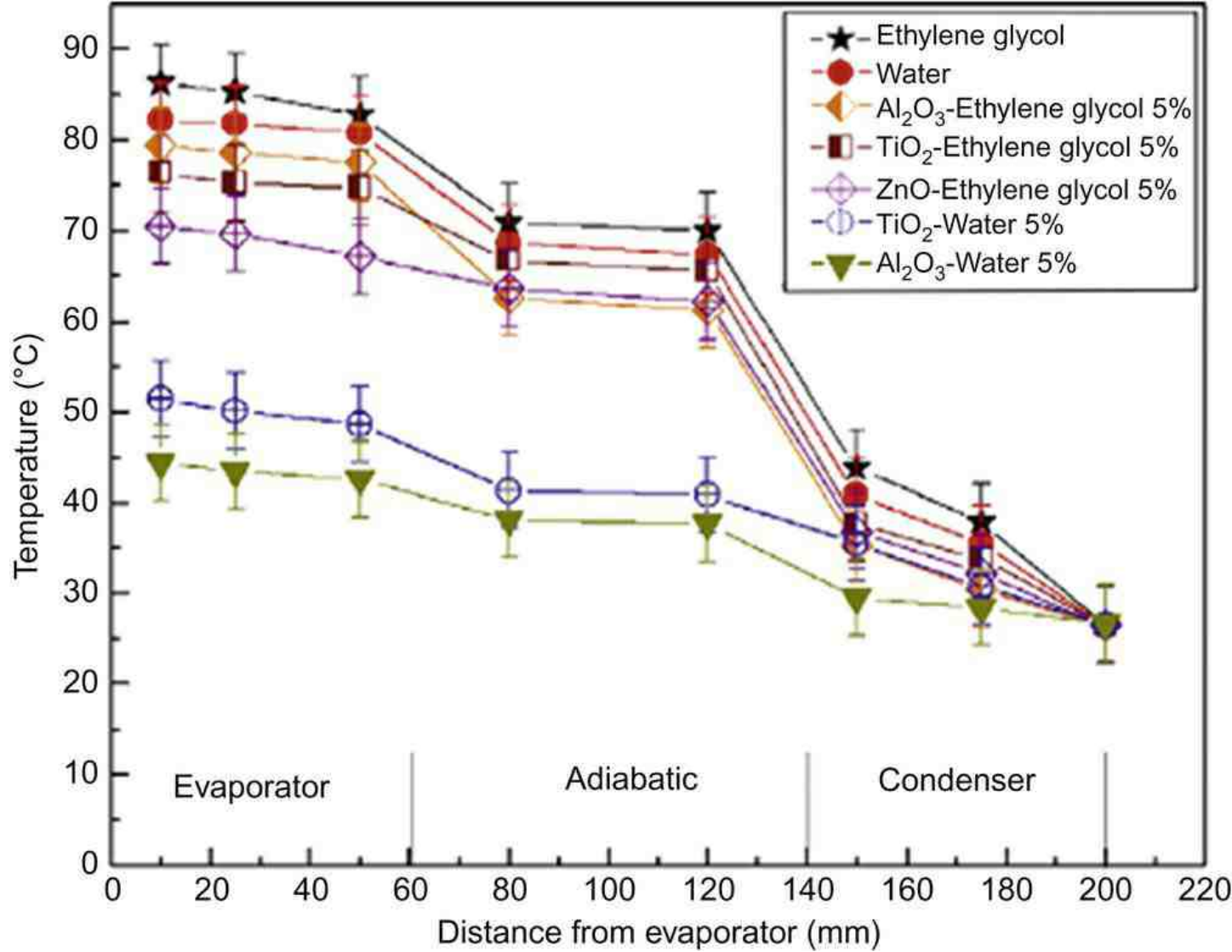| No.	Working Fluids	Thermal Resistance R_{e-a} (°C/Watt)		
		10 W	20 W	30 W
5	ZnO–ethylene glycol	1.82	1.67	1.55
6	Al_2O_3–water	0.51	0.36	0.26
7	TiO_2–water	0.76	0.63	0.54

Figure 2.45: Temperature distributions for water, ethylene glycol and ethylene-based nanofluids with 5% volume of different types of nanoparticles of heat load 30 W [121]
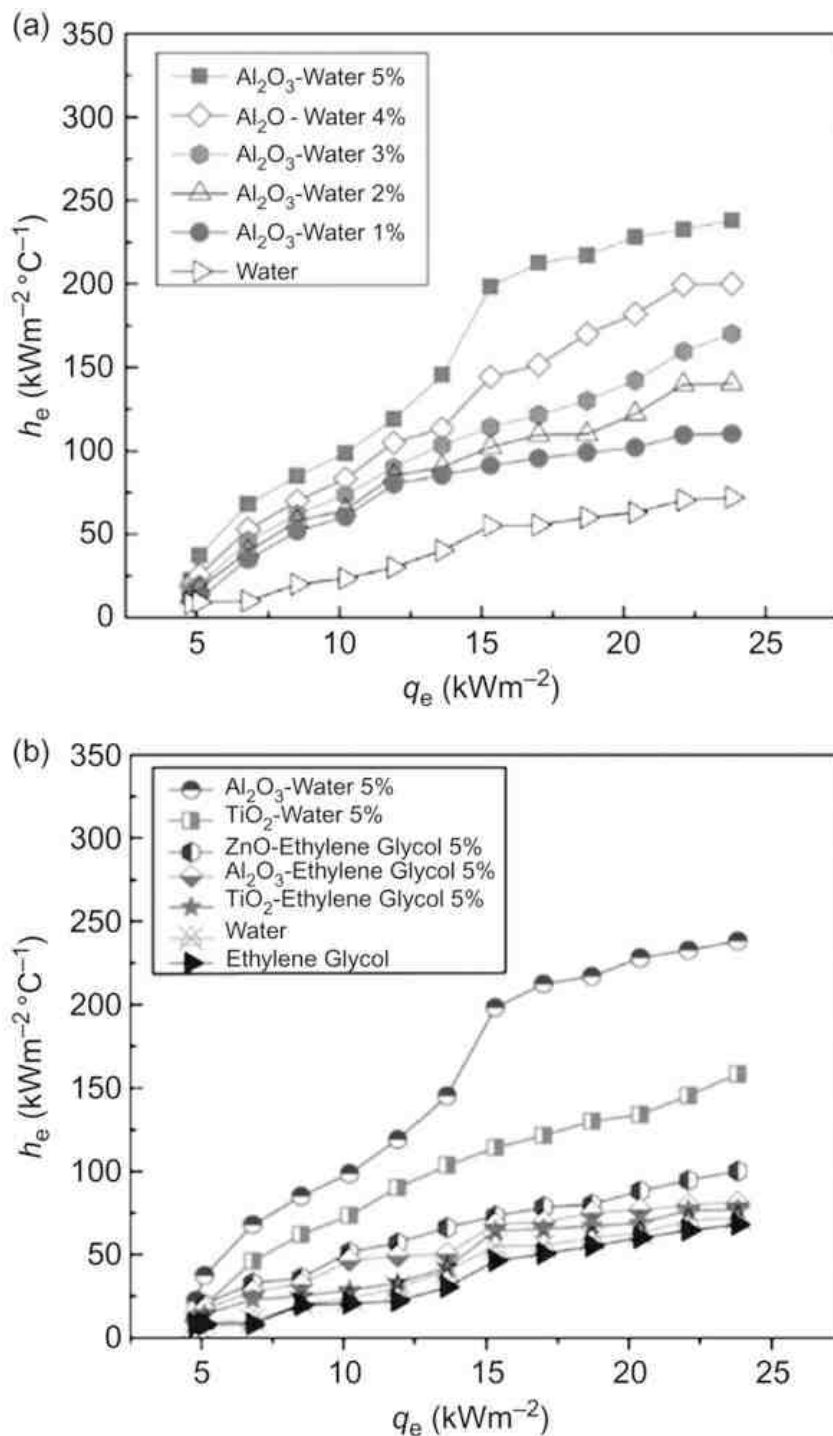
Figure 2.46: (a) Heat transfer coefficients of the evaporator with different concentrations of water-based Al_2O_3 nanofluid. (b) Heat transfer coefficients of the evaporator with different type of nanofluids [121]

The surface effect will be discussed further in Chapter 6, with reference to the performance of oscillating heat pipes.

On the negative side, increasing concentration of nanoparticles leads to an increase in density and viscosity, hence increasing concentration causes the liquid flow resistance to increase. This explains why there appears to be an optimum of concentration, above which there is no further improvement in performance. This also explains the cases where the measured performance is observed to decline with the presence of nanoparticles, for example in sintered wicks.

2.6 SUMMARY

The basic principles of fluid mechanics and heat transfer relevant to the design and performance evaluation of heat pipes have been outlined and these have been related to studies of heat pipes and thermosyphons. Particular attention has been paid to identifying the operating limits of heat pipes and thermosyphons. Prediction methods give good results with conventional fluids.

Nanofluids are currently being investigated for a wide range of heat transfer applications and have been shown to yield significant improvements in performance; however, while this has been demonstrated empirically, there is insufficient theoretical background to reliably predict performance with these fluids.

REFERENCES

[1] T.P. Cotter, Theory of heat pipes, LA-3246-MS, March 26, 1965.

[2] D.J. Shaw *Introduction to Colloid and Surface Chemistry* second ed.1970 Butterworth

[3] V.K. Semenchenke *Surface Phenomena in Metals and Alloys* 1961 Pergamon Press

[4] J. Bohdansky H.E. Schins *The surface tension of the alkali metals Inorg. Nucl. Chem.* 29 1967 2173–2179

[5] J.J. Jasper *The surface tension of pure liquid compounds J. Phys. Chem. Ref. Data* 1 1972 841

[6] IAPWS Release on Surface Tension of Ordinary Water Substance, International Association for the Properties of Water and Steam, September 1994.

[7] J. Bohdansky H.E.J. Schins *The temperature dependence of liquid metals J. Chem. Phys.* 49 1968 2982

[8] J.K. Fink, L. Leibowitz, Thermodynamic and transport properties of sodium liquid and vapor, ANL/RE-95/2, Argonne National Laboratory, January 1995.

[9] T. Iida R.I.L. Guthrie *The Physical Properties of Liquid Metals* 1988 Clarendon Press Oxford

[10] P. Walden *Uber den zusammenhang der kapillaritaskonstanten mit der latenten verdampfungswarme der losungsmittel Z. Phys. Chem.* 65 1909 267–288

[11] S. Sugden *A relation between surface tension, density and chemical composition J. Chem. Soc* 125 1924 1177–1189

[12] O.R. Quale *The parachors of organic compounds Chem. Rev.* 53 1953 439–585

[13] G.F. Hewitt *Handbook of Heat Exchanger Design* 1992 Begell House

[14] A. Brusly Solomon *Thermal performance of a heat pipe with nanoparticles coated wick Appl. Therm. Eng.* 36 2012 106–112

[15] Y. Nam S. Sharrat C. Byon S.J. Kim Y.S. Ju *Fabrication and characterization of the capillary performance of superhydrophilic Cu micropost arrays J. Microelectromech. Syst.* 19 32010 581–588

[16] Y. Nam S. Sharrat C. Byon S.J. Kim Y.S. Ju *Characterization and modelling of the heat transfer performance of nanostructured Cu micropost wicks J. Heat Transfer* 133 2011 101502-1–101502-7

[17] C.A. Busse, Pressure drop in the vapour phase of long heat pipes. Thermionic Conversion Specialists Conference, Palo Alto, CA, October 1967.

[18] J.M. Kay R.M. Nedderman *An Introduction to Fluid Mechanics and Heat Transfer* third ed.1974 Cambridge University Press Cambridge

[19] G.M. Grover, J.E. Kemme, E.S. Keddy, Advances in heat pipe technology, Second International Symposium on Thermionic Electrical Power Generation, Stresa, Italy, May 1968.

[20] D.M. Ernst, Evaluation of theoretical heat pipe performance, Thermionic Specialist Conference, Palo Alto, CA, October 1967.

[21] C.A. Bankston, J.H. Smith, Incompressible laminar vapour flow in cylindrical heat pipes. ASME Paper No. 7 1-WAJHT-1 5, 1971.

[22] A.R. Rohani C.L. Tien *Analysis of the effects of vapour pressure drop on heat pipe performance Int. J. Heat Mass Transfer.* 17 1974 61–67

[23] J.E. Deverall, J.E. Kemme, L.W. Flarschuetz, Some limitations and startup problems of heat pipes, LA-4518, November

1970.

[24] J.E. Kemme, Ultimate heat pipe performance, I.E.E.E. Thermionic Specialist Conference, Framingham, MA, 1968.

[25] J.E. Kemme, High performance heat pipes, I.E.E.E. Thermionic Specialist Conference, Palo Alto, CA, October 1967.

[26] R. Bertossi C. Romestant V. Ayel Y. Bertin *A theoretical study and review on the operational limitations due to vapour flow in heat pipes Front. Heat Pipes*3 2012 023001

[27] P. Gagneux, Contribution à l'étude des caloducs à sodium, PhD Thesis, Université de Poitiers, LET, ENSMA, 1979.

[28] L.K. Tower, D.C. Hainley, An improved algorithm for the modelling of vapour flow in heat pipes, Paper 13-8, in: Proceedings of the Seventh International Heat Pipe Conference, Minsk, Byelorussia, May 1990.

[29] B.H. Kim G.P. Peterson *Analysis of the critical Weber number at the onset of liquid entrainment in capillary-driven heat pipes Int. J. Heat Mass Transfer*38 81995 1427–1442

[30] H.A. Cheung, Critical review of heat pipe theory and applications, UCRL50453, July 1968.

[31] P.G. Drazin W.H. Reid *Hydrodynamic Stability* 1981 Cambridge University Press Cambridge

[32] S. Nukiyama *Maximum and minimum values of heat transmitted from metal to boiling water under atmospheric pressure J. Soc. Mech. Eng. Japan*37 1934 367

[33] Y.Y. Hsu *On the size range of active nucleation cavities on a heating surface ASME J. Heat Transfer* August 1962

[34] W.M. Rohsenhow *A method of correlating heat transfer data for surface boiling of liquids Trans. ASME*74 1955

[35] I.L. Mostinski *Application of the rule of corresponding states for the calculation of heat transfer and critical heat flux Teploenergetika*4 1963 66 (English abstract in British Chemical Engineering, 8, p. 580)

[36] M.G. Cooper, Saturated nucleate pool boiling – a simple correlation, in: Proceedings of the First UK National Heat Transfer Conference, IChemE Symposium Series No. 86, 2, 1984, pp. 785–793.

[37] V.I. Subbotin, Heat transfer in boiling metals by natural convection. USAEC-Tr-72 10, 1972.

[38] O.E. Dwyer *On incipient boiling wall superheats in liquid metals Int. J. Heat Mass Transfer*12 1969 1403–1419

[39] W.M. Rosenhow, P. Griffith, Correlation of maximum heat flux data for boiling of saturated liquids. ASME – AIChE Heat Transfer Symposium, Louisville, KY, 1955.

[40] B.F. Caswell, R.E. Balzhieser, The critical heat flux for boiling metal systems. Chemical Engineering Progress Symposium Series of Heat Transfer, Los Angeles, vol. 62, No. 64, 1966.

[41] E.C. Philips, J.D. Hinderman, Determination of capillary properties useful in heat pipe design. ASME. – AIChE Heat Transfer Conference Minneapolis, MN, August 1967.

[42] J.K. Ferrell J. Aileavitch *Vaporisation heat transfer in capillary wick structures Chem. Eng. Symp. Series No. 66*2 1970

[43] J.C. Corman, C.E. Welmet, Vaporisation from capillary wick structures. ASME – AIChE. Heat Transfer Conference, Tulsa, OK, Paper 71-HT-35, August 1971.

[44] A. Brautsch, P.A. Kew, The effect of surface conditions on boiling heat transfer from mesh wicks, in: Proceedings of the Twelfth International Heat Transfer Conference, Grenoble, Elsevier SAS, 2002.

[45] A. Brautsch, Heat transfer mechanisms during the evaporation process from mesh screen porous structures, PhD Thesis, Heriot-Watt University, 2002.

[46] A. Brautsch P.A. Kew *Examination and visualization of heat transfer processes during evaporation in capillary porous structures J. Appl. Therm. Eng.*22 2002 815–824

[47] J.P. Asakavicius V.A. Zukauskas V.A. Gaigalis V.K. Eva *Heat transfer from freon-113, ethyl alcohol and water with screen wicks Heat Transfer – Sov. Res.*11 11979

[48] J.W. Liu D.J. Lee A. Su *Boiling of methanol and HFE-7100 on heated surface covered with a layer of mesh Int. J. Heat Mass Transfer*44 2001 241–246

[49] J.Y. Tsay Y.Y. Yan T.F. Lin *Enhancement of pool boiling heat transfer in a horizontal water layer through surface roughness and screen coverage J. Heat Transfer*32 1996 17–26

[50] A. Abhat R.A. Seban *Boiling and evaporation from heat pipe wicks with water and acetone J. Heat Transf.* August 1974

[51] P.S. Marto, W.L. Mosteller, Effect of nucleate boiling and the operation of low temperature heat pipes. ASME – AIChE Heat Transfer Conference, Minneapolis, MN, August 1969.

[52] J.K. Ferrell, R. Davis, H. Winston, Vaporisation heat transfer in heat pipe wick materials, in: Proceedings of the First International Heat Pipe Conference, Stuttgart, Germany, 1973.

[53] R.M. Shaubach, P.M. Dussinger, J.E. Bogart, Boiling in heat pipe evaporator wick structures, in: Proceedings of the Seventh International Heat Pipe Conference, Minsk, 1990.

[54] K. Cornwell, B.G. Nair, Boiling in wicks, in: Proceeding of the Heat Pipe Forum Meeting, National Engineering Laboratory, Department of Industry, Report No. 607, East Kilbride, Glasgow, 1975.

[55] K. Cornwell B.G. Nair *Observation of boiling in porous media Int. J. Heat Mass Transfer*19 1976 236–238

[56] C.P. Costello WJ. Frea *The roles of capillary wicking and surface deposits in attainment of high pool boiling burnout heat fluxes AIChE. J.*3 101964 393

[57] F. Reiss, K. Schretzman, Pressure balance and maximum power density at the evaporator gained from heat pipe experiments, in: Second International Symposium on Thermionic Electrical Power Generation, Stresa, Italy, May 1968.

[58] R.E. Balhiser, J.A. Clark, E.E. Hucke, L.R. Smith, C.P. Colver, H. Merte, Investigation of liquid metal boiling heat transfer, Air Force Propulsion Lab, Wright Patterson, AFB, OH, AFAPL-TR 66-85, 1966.

[59] R.A. Moss A.J. Kelley *Neutron radiographic study of limiting heat pipe performance Int. J. Heat Mass Transfer*13 31970 491–502

[60] W.R. Davis, J.K. Ferrell, Evaporative heat transfer of liquid potassium in porous media, AIAA/ASME 1974 Thermophysics and Heat Transfer Conference, Boston, MA, July 1974.

[61] J.K. Ferrell, E.G. Alexander, Vaporisation heat transfer in heat pipe wick materials, AIAA Thermophysics Conference, San Antonio, TX, April 1972.

[62] G.A.A. Asselman D.B. Green *Heat Pipes Phillips Tech. Rev.*33 41973 104–113

[63] G.F.C Rogers Y.W. Mayhew *Engineering Thermodynamics – Work and Heat Transfer*fourth ed.1992 Longman

[64] C.A. Busse *Theory of ultimate heat transfer limit of cylindrical heat pipes Inst. J. Heat Mass Transfer*16 1973 169–186

[65] Anon, Heat pipes – performance of capillary-driven designs. Data Item No.70012, Engineering Sciences Data Unit, London, September 1979.

[66] C.L. Tien, K.S. Chung, Entrainment limits in heat pipes, AIAA Paper 78-382, in: Proceedings of the Third International Heat Pipe Conference, Palo Alto, CA, AIAA Report CP784, New York, 1978.

[67] F. Coyne Prenger J.E. Kemme *Performance limits of gravity-assist heat pipes with simple wick structures Proceedings of the Fourth International Heat Pipe Conference, London* 1981 Pergamon Press Oxford

[68] C.L. Tien *Fluid mechanics of heat pipes. Annual review Fluid Mech. Am. Inst. Physics*7 1975 167–185

[69] A. Abhat, H. Nguyen-chi, Investigation of performance of gravity assisted copper-water heat pipes, in: Proceedings of the Second International Heat Pipe Conference, Bologna; ESA Report SP112, vol. 1, 1976.

[70] J.R. Wiebe R.L. Judd *Superheat layer thickness measurements in saturated and subcooled nucleate boiling Trans. ASME J. Heat Transfer* 1971 Paper 71-HT-43

[71] K. Nishikawa Y. Fujita *Correlation of nucleate boiling heat transfer based on bubble population density Int. J. Heat Mass*

*Transfer*20 1977 233–245

[72] E.W. Saaski, Investigation of an inverted meniscus heat pipe wick concept, NASA Report CR-137724, 1975.

[73] K.T. Feldman, M.E. Berger, Analysis of a high heat flux water heat pipe evaporator. Tech. Report ME-62(73), ONR-012-2, U.S. Office of Naval Research, 1973.

[74] H.M. Winston, J.K. Ferrell, R. Davis, The mechanism of heat transfer in the evaporator zone of the heat pipe, in: Proceedings of the Second International Heat Pipe Conference, Bologna; ESA Report SP112, vol. 1, 1976.

[75] J.R. Johnson, J.K. Ferrell, The mechanism of heat transfer in the evaporator zone of the heat pipe, ASME Space Technology and Heat Transfer Conference, Los Angeles, CA, Paper 70-HT/SpT-12, 1970.

[76] J.E. Deverall, E.S. Keddy, Helical wick structures for gravity-assisted heat pipes, in: Proceedings of the Second International Heat Pipe Conference, Bologna; ESA Report sp112, vol. 1, 1976.

[77] R.V. Kaser, Heat pipe operation in a gravity field with liquid pool pumping, unpublished paper, McDonnell Douglas Corporation, July 1972.

[78] A.I. Strel'tsov *Theoretical and experimental investigation of optimum filling for heat pipes Heat Transfer Sov. Res.*7 11975

[79] L.L. Vasiliev, V.G. Kiselyov, Simplified analytical model of vertical arterial heat pipes, in: Proceedings of the Fifth International Heat Transfer Conference Japan, vol. 5, Paper HE 2.3, 1974.

[80] C.A. Busse J.E. Kemme *Dry-out phenomena in gravity-assist heat pipes with capillary flow Int. J. Heat Mass Transfer*23 1980 643–654

[81] M.J. Davies, G.H. Chaffey, Development and demonstration of improved gas to gas heat pipe heat exchangers for the recovery of residual heat, Report EUR 7127 EN, Commission of the European Communities, 1981.

[82] Anon, Thermophysical properties of heat pipe working fluids: operating range between −60°C and 300°C. Data Item No. 80017, Engineering Sciences Data Unit, London, August 1980.

[83] R. MacGregor P.A. Kew D.A. Reay *Investigation of low global warming potential working fluids for a closed two-phase thermosyphon J. Appl. Therm. Eng.*51 2013 917–925

[84] H. Nguyen-chi M. Groll *Entrainment or flooding limit in a closed two-phase thermosyphon Proceedings of the Fourth International Heat Pipe Conference, London* 1981 Pergamon Press Oxford

[85] Anon, Heat pipes – performance of two-phase closed thermosyphons, Data Item No. 81038, Engineering Sciences Data Unit, London, October 1981.

[86] P. Terdtoon, et al. Investigation of effect of inclination angle on heat transfer characteristics of closed two-phase thermosyphons, Paper B9P, in: Proceedings of the Seventh International Heat Pipe Conference, Minsk, May 1990.

[87] M. Groll *Heat pipe research and development in Western Europe Heat Recovery Syst. CHP*9 11989 19–66

[88] T. Payakaruk P. Terdtoon S. Ritthidech *Correlations to predict heat transfer characteristics of an inclined closed two-phase thermosyphon at normal operating conditions Appl. Therm. Eng.*20 2000 781–790

[89] I. Golobic B. Gaspersic *Corresponding states correlation for maximum heat flux in two-phase closed thermosyphon Int. J. Refrig.*20 61997 402–410

[90] R.K. Sakhuja, Flooding constraint in wickless heat pipes, ASME Publ. 73 - WA/HT-7, 1973.

[91] Z. Nejat *Effects of density ratio on critical heat flux in closed and vertical tubes Int. J. Multiphase Flow*7 1981 321–327

[92] Y. Katto *Generalized correlation for critical heat flux of the natural convection boiling in confined channels Trans. Japan. Soc. Mech. Eng.*44 1978 3908–3911

[93] C.L. Tien K.S. Chang *Entrainment limits in heat pipes AIAA J.*17 1979 643–646

[94] K. Harada S. Inoue J. Fujita H. Suematsu Y. Wakiyama *Heat transfer characteristics of large heat pipes Hitachi Zosen*

*Tech. Rev.*41 1980 167–174

[95] Z.R. Gorbis, G.A. Savchenkov, Low temperature two-phase closed thermosyphon investigation, in: Proceedings of the Second International Heat Pipe Conferences Bologna, Italy, 1976, pp. 37–45.

[96] M.K. Bezrodnyi *Isledovanie krizisa teplomassoperenosa v nizkotemperaturnih besfiteljinyih teplovih trubah Teplofizika visokih temperature*15 1977 371–376

[97] M. Groll, S. Rosler, Development of advanced heat transfer components for heat recovery from hot waste gases, Final Report CEC Contract No. EN3E–0027–D(B), 1989.

[98] F.C. Prenger, Performance limits of gravity-assisted heat pipes, in: Proceedings of the Fifth International Heat Pipe Conference, Tsukuba, Japan, 1984, pp. 1–5.

[99] T. Fukano K. Kadoguchi C.L. Tien *Experimental study on the critical heat flux at the operating limit of a closed two-phase thermosyphon Heat Transfer Japan. Res.*17 1988 43–60

[100] H. Imura K. Sasaguchi H. Kozai *Critical heat flux in a closed two-phase thermosyphon Int. J. Heat Mass Transfer*26 1983 1181–1188

[101] I.L. Pioro M.V. Voronenva *Rascetnoe opredelenie predelnogo teplovogo potoka pri kipenii zidkostej v dvuhfaznih termosifonah Inz. fiz. zurnal*53 1987 376–383

[102] I. Golobic, B. Gaspersic, Generalized method for maximum heat transfer performance in two-phase closed thermosyphon, International Conference CFCs, The Day After Padova, Italy, 1994, pp. 607–616.

[103] S.U.S. Choi J.A. Eastman *Enhancing thermal conductivity of fluids with nanoparticles* D.A. Siginer H.P. Wang *Developments and Applications of Non-Newtonian Flows* 1995 ASME New York, NY 99–105

[104] Z-H. Liu Y-Y Li *A new frontier of nanofluid research – application of nanofluids in heat pipes Int. J. Heat Mass Transfer*55 2012 6786–6797

[105] H.T. Chien C.Y. Tsai P.H. Chen P.Y. Chen *Improvement on thermal performance of a disk-shaped miniature heat pipe with nanofluid* pp. 389–391 *Proceedings of the Fifth International Conference on Electronic Packaging Technology* 2003 IEEE Shanghai, China

[106] W.C. Wei S.H. Tsai S.Y. Yang S.W. Kang *Effect of nano-fluid concentration on heat pipe thermal performance IASME Trans.*2 2005 1432–1439

[107] W. Kang W.C. Wei S.H. Tsai S.Y. Yang *Experimental investigation of silver nano-fluid on heat pipe thermal performance J. Appl. Therm. Eng.*26 2006 2377–2382

[108] X.F. Yang Z.H. Liu J. Zhao *Heat transfer performance of a horizontal micro-grooved heat pipe using CuO nanofluid J. Micromech. Microeng.*18 2008

[109] Z.H. Liu L. Lu *Thermal performance of axially microgrooved heat pipe using carbon nanotube suspensions J. Thermophys. Heat Transfer*23 2009 170–175

[110] K.H. Do S.P. Jang *Effect of nanofluids on the thermal performance of a flat micro heat pipe with a rectangular grooved wick Int. J. Heat Mass Transfer*53 2010 2183–2192

[111] M. Shafahi V. Bianco K. Vafai O. Manca *Thermal performance of flat-shaped heat pipes using nanofluids Int. J. Heat Mass Transfer*53 2010 1438–1445

[112] M. Shafahi V. Bianco K. Vafai O. Manca *An investigation of the thermal performance of cylindrical heat pipes using nanofluids Int. J. Heat Mass Transfer*53 2010 376–383

[113] Z.H. Liu Y.Y. Li R. Bao *Thermal performance of inclined grooved heat pipes using nanofluids Int. J. Therm. Sci.*49 2010 1680–1687

[114] G.S. Wang B. Song Z.H. Liu *Operation characteristics of cylindrical miniature grooved heat pipe using aqueous CuO nanofluids Expt. Therm. Fluid Sci.*34 2010 1415–1421

[115] C.Y. Tsai H.T. Chien P.P. Ding B. Chan T.Y. Luh P.H. Chen *Effect of structural character of gold nanoparticles in nanofluid on heat pipe thermal performance Mater. Lett.*58 2004 1461–1465

[116] Z.H. Liu T. Shu *Application of nanofluids in thermal performance enhancement of horizontal screen heat pipe J. Aerospace Power*23 2008 1623–1627

[117] Y.T. Chen W.C. Wei S.W. Kang C.S. Yu *Effect of nanofluids on flat heat pipe thermal performance* pp. 16–20 *Proceedings of the Twenty-Fourth IEEE Semiconductor Thermal Measurement and Management Symposium* 2008 IEEE San Jose, CA

[118] K.H. Do H.J. Ha S.P. Jang *Thermal resistance of screen mesh wick heat pipes using the water-based Al_2O_3 nanofluids Int. J. Heat Mass Transfer*53 2010 5888–5894

[119] Z.H. Liu Q.Z. Zhu *Application of aqueous nanofluids in a horizontal mesh heat pipe Energ. Convers. Manage.*52 2011 292–300

[120] R. Senthilkumar S. Vaidyanathan B. Sivaraman *Experimental analysis of cylindrical heat pipe using Copper nanofluid with an aqueous solution of N-hexanol Front. Heat Pipes*2 32011

[121] N. Putra W.N. Septiadi H. Rahman I. Irwansyah *Thermal performance of screen mesh wick heat pipes with nanofluids Exp. Therm. Fluid Sci.*40 2012 10–17

[122] P.-W. Wang X.-J. Chen Z.-H. Liu Y.-P. Liu *Application of nanofluid in an inclined mesh wicked heat pipes Thermochim. Acta*539 2012 100–108

[123] R.R. Riehl, Analysis of loop heat pipe behaviour using nanofluid, in: Proceedings of Heat Powered Cycles International Conference (HPC), 11–14 September 2006, Newcastle, UK, 06102, 2006.

[124] S.W. Kang W.C. Wei S.H. Tsai C.C. Huang *Experimental investigation of nanofluids on sintered heat pipe thermal performance Appl. Therm. Eng.*29 2009 973–979

[125] M.K. Moraveji S. Razvarz *Experimental investigation of aluminum oxide nanofluid on heat pipe thermal performance Int. Commun. Heat Mass Transfer*39 2012 1444–1448

[126] H.B. Ma C. Wilson B. Borgmeyer K. Park Q. Yu U.S. Choi M. Tirumala *Effect of nanofluid on the heat transport capability in an oscillating heat pipe Appl. Phys. Lett.*88 2006 143116

[127] H.B. Ma C. Wilson Q. Yu K. Park U.S. Choi M. Tirumala *An experimental investigation of heat transport capability in a nanofluids oscillating heat pipe J. Heat Transfer*128 2006 1213–1216

[128] F.M. Shang D.Y. Liu H.Z. Xian Y.P. Yang X.Z. Du *Flow and heat transfer characteristics of different forms of nanometer particles in oscillating heat pipe J. Chem. Indust. Eng.*58 2007 2200–2204

[129] Y.H. Lin S.W. Kang H.L. Chen *Effect of silver nano-fluid on pulsating heat pipe thermal performance Appl. Therm. Eng.*28 2008 1312–1317

[130] K. Park H.B. Ma *Nanofluid effect on heat transport capability in a well-balanced oscillating heat pipe J. Thermophys. Heat Transfer*21 2007 443

[131] J. Qu H.Y. Wu P. Cheng *Thermal performance of an oscillating heat pipe with Al_2O_3–water nanofluids Int. Commun. Heat Mass Transfer*37 2010 111–115

[132] N. Bhuwakietkumjohn S. Rittidech *Internal flow patterns on heat transfer characteristics of a closed-loop oscillating heat-pipe with check valves using ethanol and a silver nano-ethanol mixture Exp. Therm. Fluid Sci.*34 2010 1000–1007

[133] P. Cheng S. Thompson J. Boswell H.B. Ma *An investigation of flat-plate oscillating heat pipes J. Electron. Pack.*132 2010 041009

[134] Y. Ji H. Ma F Su G. Wang *Particle size effect on heat transfer in an oscillating heat pipe Exp. Therm. Fluid Sci.*35 2011 724–727

[135] M. Taslimifar M. Mohammadi H. Ashfin H. Saidi M.B. Shafii *Overall thermal performance of ferrofluidic open loop*

*pulsating heat pipes: an experimental approach Int. J. Therm. Sci.*65 2013 234–241

[136] R.R Riehl N. Santos *Water–copper nanofluid application in an open loop pulsating heat pipe Appl. Therm. Eng.*42 2012 6–10

[137] Y.H. Peng S.Y. Huang K.J. Huang *Experimental study on thermosyphon by adding nanoparticles to working fluid J. Chem. Industry Eng. (China)*55 2004 1768–1772

[138] H. Xue J. Fan Y. Hu R. Hong K. Cen *The interface effect of carbon nanotube suspension on the thermal performance of a two-phase closed thermosyphon J. Appl. Phys.*100 2006 104909

[139] Z.H. Liu X.F. Yang G.L. Guo *Effect of nanoparticles in nanofluid on thermal performance in a miniature thermosyphon J. Appl. Phys.*102 2007 013526

[140] Z.H. Liu J.G. Xiong R. Bao *Boiling heat transfer characteristics of nanofluids in a flat heat pipe evaporator with micro-grooved heating surface Int. J. Multiphase Flow*33 2007 1284–1295

[141] S. Khandekar Y.M. Joshi B. Mehta *Thermal performance of closed two-phase thermosyphon using nanofluids Int. J. Therm. Sci.*47 2008 659–667

[142] P. Naphon P. Assadamongkol T. Borirak *Experimental investigation of titanium nanofluids on the heat pipe thermal efficiency Int. Commun. Heat Mass Transfer*35 2008 1316–1319

[143] P. Naphon D. Thongkum P. Assadamongkol *Heat pipe efficiency enhancement with refrigerant–nanoparticles mixtures Energy Convers. Manage.*50 2009 772–776

[144] S.H. Noie S.Z. Heris M. Kahani S.M. Nowee *Heat transfer enhancement using Al$_2$O$_3$/water nanofluid in a two-phase closed thermosyphon Int. J. Heat Fluid Flow*30 2009 700–709

[145] Z.H. Liu X.F. Yang G.S. Wang G.L. Guo *Influence of carbon nanotube suspension on the thermal performance of a miniature thermosyphon Int. J. Heat Mass Transfer*53 2010 1914–1920

[146] T. Parametthanuwat S. Rittidech A. Pattiya *A correlation to predict heat-transfer rates of a two-phase closed thermosyphon (TPCT) using silver nanofluid at normal operating conditions Int. J. Heat Mass Transfer*53 2010 4960–4965

[147] T. Paramatthanuwat S. Boothaisong S. Rittidech K. Booddachan *Heat transfer characteristics of a two-phase closed thermosyphon using deionized water mixed with silver nano Heat Mass Transfer*46 2010 281–285

[148] G. Huminic A. Huminic I. Morjan F. Dumitrache *Experimental study of the thermal performance of thermosyphon heat pipe using iron oxide nanoparticles Int. J. Heat Mass Transfer*54 2011 656–661

[149] G. Huminic A. Huminic *Heat transfer characteristics of a two-phase closed thermosyphons using nanofluids Expt. Thermal Fluid Sci.*35 2011 550–557

[150] J. Qu H. Wu *Thermal performance comparison of oscillating heat pipes with SiO$_2$/water and Al$_2$O$_3$/water nanofluids Int. J. Therm. Sci.*50 2011 1954–1962

[151] Y.-H. Hung T.-P. Teng B.-G. Lin *Evaluation of the thermal performance of a heat pipe using alumina nanofluids Exp. Therm. Sci.*44 2013 504–511